LBL-5439
c.1

PHOTOIONIZATION STUDIES WITH MOLECULAR BEAMS

Cheuk-Yiu Ng
(Ph. D. thesis)

September 1976

Prepared for the U. S. Energy Research and
Development Administration under Contract W-7405-ENG-48

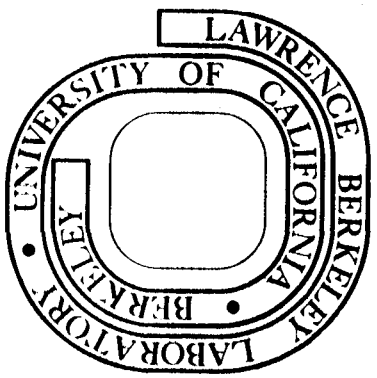

LBL-5439
c.1

DISCLAIMER

PHOTOIONIZATION STUDIES WITH MOLECULAR BEAMS

Cheuk-Yiu Ng

Materials and Molecular Research Division, Lawrence Berkeley Laboratory
Department of Chemistry; University of California
Berkeley, California 94720

ABSTRACT

A molecular beam photoionization apparatus which combines the advantages of both the molecular beam method with photoionization mass spectrometry has been designed and constructed for carrying out some unique photoionization experiments. It essentially consists of a differentially pumped windowless vacuum ultraviolet monochromator, a modulated supersonic beam production system, an ionization chamber, photon detectors, a low noise quadrupole mass spectrometer and intense continuum light sources (extending from 600Å to 2000Å).

Rotational cooling during the supersonic expansion has resulted in high resolution photoionization efficiency curves for NO, ICl, C_2H_2 and CH_3I. The analysis of these spectra has yielded ionization potentials for these molecules to an accuracy of ± 3 meV. Detailed autoionization structures were also resolved. This allows the investigation of the selection rules for autoionization, and the identification of the Rydberg series which converge to the excited states of the molecular ions. The degree of relaxation for thermally populated excited states has been examined using NO and ICl as examples. As a result of adiabatic cooling, a small percentage of dimers is also formed during the expansion. The photoionization efficiency curves for

$(NO)_2$, ArICl, Ar_2, Kr_2 and Xe_2 have been obtained near the thresholds. Using the known dissociation energies of the $(NO)_2$, Ar_2, Kr_2 and Xe_2 van der Waals molecules, the corresponding dissociation energies for NO-NO^+, Ar_2^+, Kr_2^+, and Xe_2^+ have been determined. The ionization mechanisms for this class of molecules is examined and discussed.

ACKNOWLEDGMENTS

I would like to express my deepest appreciation to Professor Y. T. Lee for his support, understanding, and assistance throughout the course of this research. His physical insight and encouragement have made my graduate studies to be one of the most exciting and fruitful periods in my life. Special acknowledgement goes to Professor B. H. Mahan for his advice and helpful suggestions during the last two years. I would also like to thank my many colleagues, Dr. T. P. Schaefer, Dr. F. P. Tully, Dr. J. M. Farrar, Dr. C. H. Chen, Dr. K. Shobatake, Mr. J. J. Valentini, Dr. M. J. Coggiola, Mr. R. K. Sparks, Mr. P. A. Schulz, Mr. Z. F. Wang, Mr. C. J. Becker, Mr. R. J. Buss, Mr. D. J. Trevor, Mr. S. J. Sibener, Mrs. C. C. Kahler, Miss P. L. Kronebusch and Mr. R. C. Sharp for their assistance, friendship and enlightening discussion.

The assistance of Dr. J. Conway and Mr. G. Shalimoff in aligning the monochromator and lending us the discharge lamp power supply is greatly appreciated. Special acknowledgement extends to Professor W. A. Chupka for his helpful advice in the design and construction of the vacuum ultraviolet light source, and Mr. G. Gabor for helpful suggestions in the design of the scintillation detector. I wish to take this opportunity to acknowledge the skillful assistance of the technical staff of the machine, ceramic, glass and electronic shop of the Lawrence Berkeley Laboratory during the development of the instruments, and to thank Mrs. Ann Weightman for typing the manuscript.

I am most grateful to my wife for her love, and deep understanding and encouragement.

TABLE OF CONTENTS

I. INTRODUCTION

The major processes resulting from the absorption of a vacuum photon by an atom or a molecule may be summarized as follows:

(1)	$X + h\nu \rightarrow X^*$	Atomic Excitation
(2)	$X + h\nu \rightarrow X^+ + e + K.E.$	Atomic Photoionization
(3)	$X + h\nu \rightarrow X^* \rightarrow X^+ + e + K.E.$	Atomic Autoionization
(4)	$XY + h\nu \rightarrow XY^*$	Molecular Excitation
(5)	$XY + h\nu \rightarrow X + Y + K.E.$ (X and/or Y can be an excited state)	Molecular Dissociation
(6)	$XY + h\nu \rightarrow XY^+ + e + K.E.$	Molecular Photoionization
(7)	$XY + h\nu \rightarrow XY^* \rightarrow X + Y + K.E.$	Predissociation
(8)	$XY + h\nu \rightarrow XY^* \rightarrow XY^+ + e + K.E.$	Molecular Autoionization
(9)	$XY + h\nu \rightarrow XY^+ + e \rightarrow X^+ + Y + e$	Fragmentation of Parent Ion
(10)	$XY + h\nu \rightarrow XY^* \rightarrow X^+ + Y^-$	Ion-Pair Formation

The study of these processes, which provide detailed information on the electronic state structures of gases, atoms and molecules as well as atomic and molecular ions, is a fundamental subject of physics and chemistry. The mechanism of UV photon interactions with gases is very important to the understanding of the events associated with phenomena ranging from electrical discharges and plasma physics, upper atmospheric aeronomy and astrophysics. Nevertheless, it is apparent that no single type of experiment is able to carry out detailed investigation of all these processes. As a matter of fact, it is only from different complementary experimental techniques that a full

picture of these mechanisms can be realized.

In vacuum ultraviolet absorption spectroscopy, the total absorption cross section is measured as a function of photon energy. This method provides the most accurate means of determining ionization potentials in the case where analysis of the spectrum allows identification of a sufficient number of Rydberg levels. For atoms, the absorption cross-section will closely approximate the ionization cross section, whereas for molecules other processes such as dissociation may occur. It is often true that due to the broadening of absorption lines because of predissociation, etc., that the identification of the Rydberg series is made difficult or impossible.

Photoelectron spectroscopy involves the measurement of the kinetic energies of the ejected electrons by the interactions of a monoenergetic beam of photons with an atom or a molecule. This method is an especially unambiguous one for the study of molecular electronic structures of substances in a vapor state. However, the lack of mass discrimination to assist in the identification of the ions formed often makes the analysis of the spectra very difficult.

The measurement of the ionization cross section for a particular ionizing channel as a function of photon energy is the object of the photoionization experiment. The photoionization efficiency curve (number of ions produced per photon transmitted, plotted as a function of wavelength) will, if taken at sufficient high resolution, usually contains information on the first and higher ionization potentials, vibrational frequency of the ion, and Franck-Condon factors for the

ionization process. Also found in the photoionization efficiency curves are sharp peaks due to autoionization, in which the ionization takes place in two stages. The first step is a resonant process involving the excitation of the neutral species to a discrete resonant state above its ionization potentials, and the second is the spontaneous loss of the electron. This structure allows the investigation of the coupling between discrete states and ionization continuum (i.e., the selection rules and lifetime etc. for autoionization). Furthermore, the measurement of ionization and appearance potentials can, by consideration of suitable thermodynamic cycles, provide a great deal of thermochemical data for both ionic and neutral species. Consider the case of molecular photoionization in process (6). The appearance potential is

$$AP(XY^+) = \Delta H_f(XY^+) - \Delta H_f(XY)$$

Since $\Delta H_f(XY)$ is known for a large number of compounds, then $\Delta H_f(XY^+)$ can be determined. Another example as in process (9) we have

$$AP_9(X^+) = IP(X) + D(X\text{-}Y)$$

where either the bond dissociation energy may be known from other experiments or it may be possible to measure the ionization potential of X from the above equation.

If the ion pair process also occurs, the difference in the appearance potential for process (10), $AP_{10}(X^+)$, and that of process (9), $AP_9(X^+)$ give the electron affinity of Y. That is

$$AP_9(X^+) - AP_{10}(X^+) = EA(Y)$$

However, as mentioned above, the full potential of the photoionization experiment will be fully realized only if high resolution photoionization efficiency curves are obtained. At the present technological level, a windowless vacuum ultraviolet monochromator operated by extensive differential pumping and an intense laboratory continuum vacuum ultraviolet light source are available. These enable the usual instrumental resolution for photoionization experiments to be as high as 1-10 meV without suffering from very low ion intensity. However, it is the rotational envelope of the molecules at room temperature that limits the ultimate resolution. For diatomic molecules, the rotational envelope half-width within a single electronic vibration is of the order of kT = 0.025 eV, while that of polyatomic molecule is about 39 meV. The rotational spread can be suppressed by cooling the gas to low temperature. In the case of hydrogen, by cooling the gas to liquid nitrogen temperature, an energy resolution as high as 0.04Å has been obtained by Chupka and co-workers.[1] Obviously, this is not applicable to condensable gases. One way to circumvent this difficulty is to use the modulated supersonic beam technique. It is known that adiabatic cooling of the gas during the expansion is extremely effective in lowering the rotational temperature. Furthermore, the beam technique also allows the photoionization of dimers and transient radicals to be possible. This thesis reports the results of high resolution photoionization studies of condensable gases (NO, ICl, CH_3I and C_2H_2) and dimers ($(NO)_2$, Xe_2, Kr_2 and Ar_2) using the molecular beam method.

REFERENCES

1. W. A. Chupka and J. Berkowitz, J. Chem. Phys., 51, 4244 (1969).

II. Theoretical Considerations

The ionization may be a direction process which involves a direct transition of a bound electron into the ionization continuum, or may take place by an indirect process, for example autoionization and predissociation.

2.1 Direct Ionization

It has been shown both theoretically[1,2] and experimentally[3] that the threshold for photoionization is a step-like function, i.e., the onset rises sharply at the threshold of each process and then tends to assume a constant value. To a first approximation, the cross section for photoionization can be calculated by considering the interaction of a photon with an atomic or molecular system to be analogous to the interaction of an electromagnetic wave with an electric dipole. If the wavelength of the incoming photon is long compared with the distance over which the wavefunctions are appreciable, the dipole approximation is satisfactory, and the operator describing the interaction of two wavefunctions may be taken to be the dipole operator.[4] Assuming only a single electron to be involved in the transition, the expression for total photoionization cross section is[5]

$$\sigma_\nu = \frac{4\Pi^2 \alpha a_o^2}{3} \quad \frac{V_i + k^2}{g_i} \quad |M_{if}|^2 \tag{1}$$

M_{if}, is the matrix element defined by

$$|M_{if}|^2 = \sum_i \sum_j \left| \int \Psi_f^* \sum_\mu r_\mu \Psi_i \, dc \right|^2 \tag{2}$$

σ_ν is the photoionization cross section at some radiation frequency ν.

m, e, are the mass and charge respectively of an electron.

g_i is the degeneracy of the initial state.

$\sum_i \sum_j$ denote sums over the initial and final state respectively.

Ψ_i is the initial state wavefunction.

Ψ_f^* is the final state wavefunction.

k^2 is the kinetic energy of the ejected electron.

V_i is the ionization threshold energy.

$\sum_\mu r_\mu$ characterizes the dipole moment operator.

α is the fine structure constant.

a_o is the Bohr radius.

Equation (1) indicated that the cross-section depends not only on the matrix element M_{if} but also on the frequency of the incident radiation and the velocity of the ejected electron. Let us consider the photoionization partial cross section which only involves the transition from Ψ_i to Ψ_f and let r and R denote the electronic and nuclear coordinates respectively. Assuming the photoionization process is rapid with respect to the vibrational period, i.e., the molecule contains a fixed nuclear geometry during this process, we can introduce the Born-Oppenheimer approximation and hence $\Psi_{i,f}$ can be written as the product of an electronic and a vibrational wavefunction (neglecting rotation) i.e., $\Psi_i = \psi_{e''}\psi_{v''}$ and $\Psi_f = \psi_{e'}\psi_{v'}$. The transition probability

$$P_{v'v''} \propto \left| \int \psi_{e'}\psi_{v'}(M_r + M_R)\psi_{e''}\psi_{v''} dr dR \right|^2 \qquad (3)$$

M_r and M_R are the dipole moment operators which depends on electronic and nuclear coordinates respectively. If $\psi_{e'}$ and $\psi_{e''}$ are orthorgonal

wavefunctions, we have

$$P_{v',v''} \propto \left|\int \psi_{e'} M_r \psi_{e''} dr \int \psi_{v'} \psi_{v''} dR + \cancelto{0}{\int \psi_{e'} \psi_{e''} dr} \int \psi_{v'} M_R \psi_{v''} dR\right|^2$$

$$= \left|\int \psi_{e'} M_r \psi_{e''} dr\right|^2 \left|\int \psi_{v'} \psi_{v''} dR\right|^2$$

$$= |\overline{Pe}|^2 \left|\int \psi_{v'} \psi_{v''} dR\right|^2$$

where $\left|\int \psi_{v'} \psi_{v''} dR\right|^2$ is the Franck-Condon factor which gives relative strengths of electronic transitions and distributes the intensity into appropriate vibrational states. For states of the ion having equilibrium distance different from that in the ground state of the neutral molecule, maximum wavefunction overlap (Franck-Condon region) occurs at a position on the potential energy surface of the ion different from the ground state. The most commonly observed Franck-Condon overlap conditions in photoionization are shown in Fig. (1).[6] The transitions are all taken as originating from the zero vibrational level of the initial electronic state. The maximum probability for a transition occurs in the center of the Franck-Condon region where the initial wavefunctions has its maximum. The three cases shown are:

a. The ionization only involves in removal of a nonbinding or "lone pair" electron, which has little effect in the bonding of the molecular ion. In other words, there is little or no change in internuclear distance or vibrational interval from that of the neutral molecule. The photoionization efficiency curve will essentially show one big step corresponding to an intense 0-0 transition as indicated in curve (a) of Fig. 1.

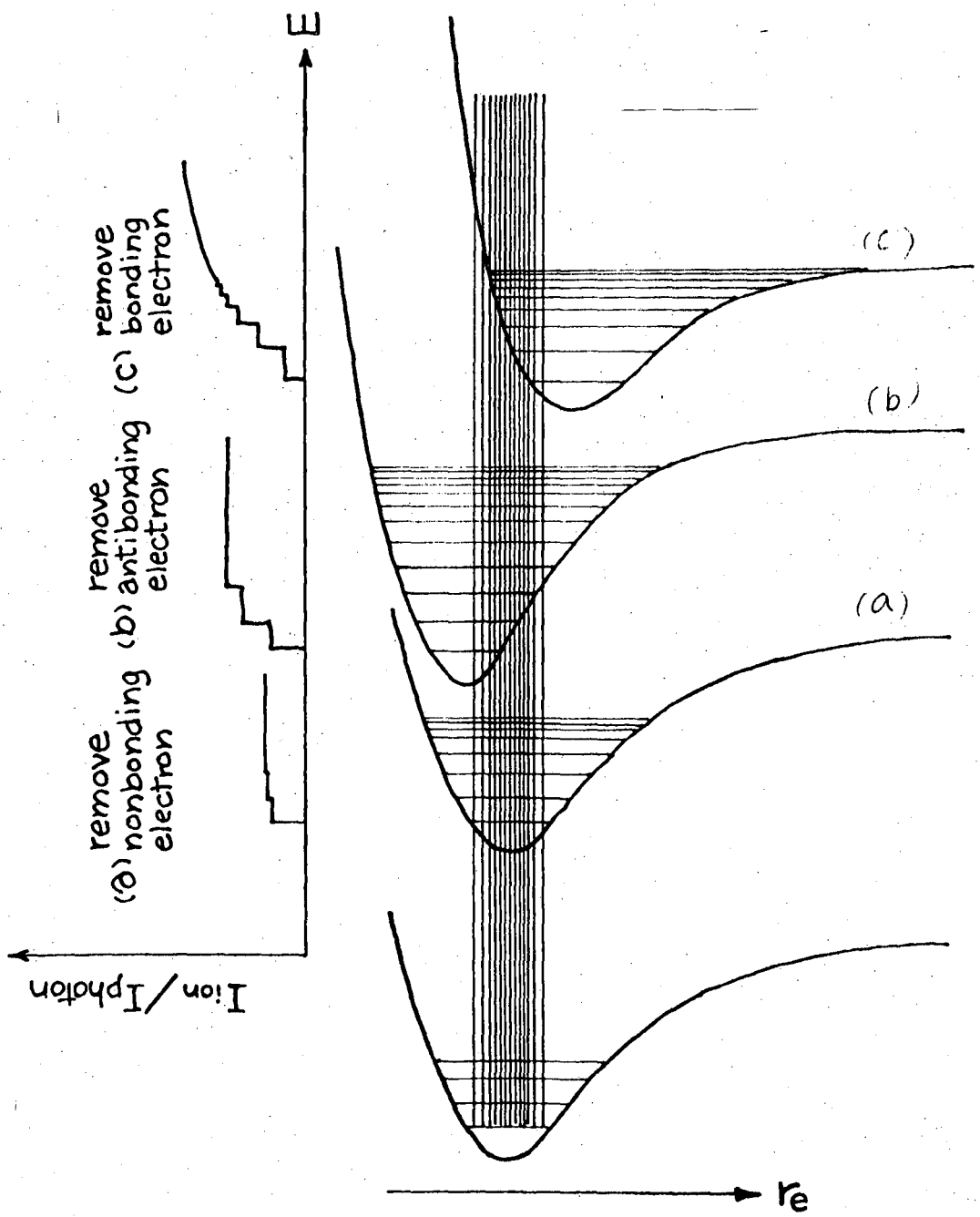

Fig. 1 Application of Franck-Condon Principle to photoion Production

b. The removal of an antibonding electron results in strengthening the bonding of the molecular ion. This implies a decrease in bond length and wider vibrational spacing for the ionic state. The photoionization efficiency curve hence will show a few widely spaced steps as shown in curve (b) of Fig. 1 (e.g. NO).

c. Removal of a bonding electron produces transitions to the steeper slope of the strongly repulsive portion of the ion potential well. The photoionization efficiency curve usually is composed of a closely spaced steps indicating an increase in bond length (weaker bonding) and frequency reduction in the molecular ion with respect to that in the neutral molecule. (e.g. C_2H_2). This is shown in curve (c) of Fig. 1.

If $|\overline{Pe}|^2$ is assumed independent of total energy and photoelectron energy, the intensity ratio corresponding to the transition from the ground state $\psi_{v''}$ to two vibrational states (v' + 1, v') of the molecular ion will bear the relation

$$\frac{\text{Step Height } (v' + 1)}{\text{Step Height } (v')} = \frac{|\langle\psi_{v''}|\psi_{v'+1}\rangle|^2}{|\langle\psi_{v''}|\psi_{v'}\rangle|^2} \qquad (4)$$

2.2 Autoionization

The removal of an electron from an atom or molecule which does not involve a transition directly into the continuum is known as autoionization. This process arises due to the overlapping of discrete energy levels by a continuous range of levels as depicted in Fig. 2. Series 1 represents the Rydberg levels converging to the first ionization potential and series 2 the Rydberg levels leading to a

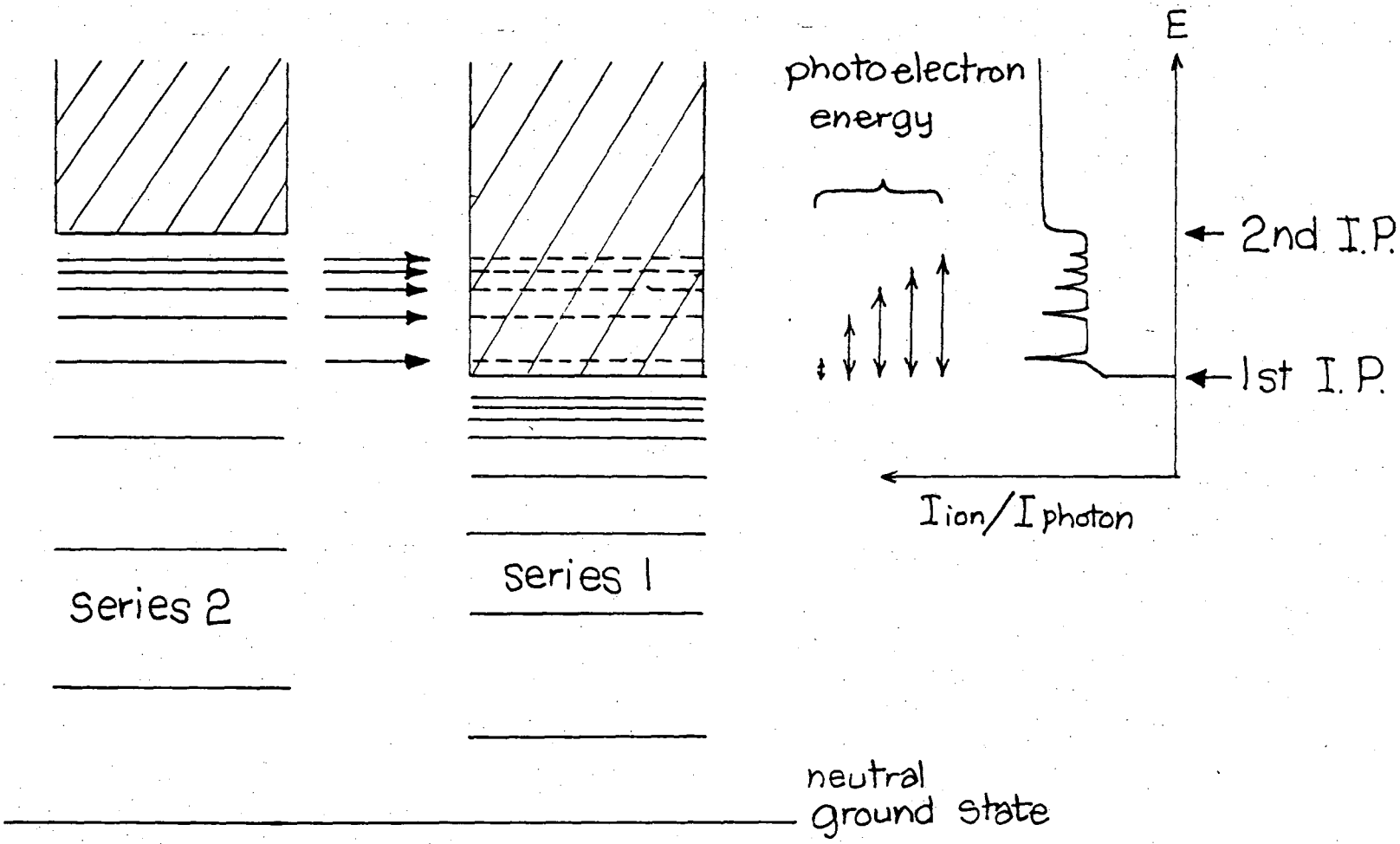

Fig. 2. Autoionization of atoms & Molecules after excitation
Levels above the 1st. I.P.

higher ionic state. If an electron is excited to a bound level in series 2 which is higher in energy than the first ionization potential associated with series 1, then the possibility exists of a radiationless transition from the bound molecular state into a stable ionic state. The electron ejected in this manner will have a kinetic energy equal to the difference between the energy of the bound state and the lower ionization potential. Unlike the direct ionization, autoionization is a resonant process occurring only at discrete energies which correspond to the bound levels of series 2. The process is manifested as a number of peaks on the photoionization efficiency curve as shown in Fig. 2.

The phenomenon was first postulated by Shenstone[7] to explain the broadening and asymmetry of some absorption peaks above the ionization potential of certain species. The theoretical aspects of autoionization have been investigated extensively. Fano[8] postulated configuration interaction between the discrete states and the continuum, and has studied theoretically the asymmetric peaks of autoionization which appear in the photoionization efficiency curve. He has been able to predict the position and intensity shifts produced in a Rydberg series due to autoionization. Mies[9] has extended Fano's theory of configuration interaction to include the case of many discrete states interacting with many continuum channels, with the possibility that neighboring resonances may overlap, i.e., that their autoionization widths may be greater than the spacing between discrete states. The transition amplitude is

$$t^{-}_{v'} = \sum_{\alpha} F_{v',\alpha} F_{\alpha,v''} C_{\alpha} \tag{5}$$

where $$C_{\alpha} = t_e[1 + q \sum_{n^*} \varepsilon^{-1}_{\alpha,n^*}]/[1 + i \sum_{n^*} \varepsilon^{-1}_{\alpha,n^*}] \tag{6}$$

$$\varepsilon_{\alpha,n^*} = (\varepsilon - \varepsilon_{\alpha,n^*})/(1/2\Gamma) \tag{7}$$

$$\Gamma = \sum_{v'} \Gamma_{v'} = 2 \sum_{v'} |\langle \Psi_{v',f} | H | \Psi_{\alpha,n^*} \rangle|^2 \tag{8}$$

$t^{-}_{v'}$ is the transition amplitude from ground vibrational state v" to final ionic vibrational state v'.

n* & α are the effective principle quantum number and vibrational quantum number respectively which characterize the Rydberg state.

q is the Fano's line profile index.

v", α, v' are the index for denoting the vibrational quantum number for the ground state, Rydberg state and final molecular ionic state.

$F_{v',\alpha}$ & $F_{\alpha,v''}$ are the Franck-Condon factors between the corresponding vibrational levels.

H is the interelectronic repulsion causing the two electron transition.

Γ is the total autoionization width of state (n^*,α).

t_e is a factor which depends on the electronic transition probability.

ε is the incident photon energy.

If the widths of the states are much less than the separation between successive states, autoionization will be important only if ε is close to the energy of some state n*, α, then

$$C_{\alpha} = t_e[\varepsilon_{\alpha,n^*} + q]/[\varepsilon_{\alpha,n^*} + i] \tag{9}$$

which is Bardsley's result.[10] If ε is far from any sharp resonance $C_{\alpha} = t^c$ for all α

$$t_{v'}^{-} = t_e \sum_{\alpha} F_{v'\alpha} F_{\alpha,v''} = t_e F_{v',v''} \tag{10}$$

which is the direct photoionization result. However if ε falls precisely on a single resonance (n^*, α) which does not overlap with any other resonance, then

$$t_{v'}^{-} = t_e [F_{v''v'} - F_{v''\alpha} F_{\alpha v'} (1 + iq)] \tag{11}$$

The first term in bracket is the contribution of direct photoionization and the second is the contribution of the autoionizing state. If the second term predominates, the intensity ratio of two vibrational peaks ($v' + 1$, v') now has the form[11]

$$\frac{\text{intensity } (v' + 1)}{\text{intensity } v'} = \left(\frac{F_{v' + 1, \alpha}}{F_{v'\alpha}} \right)^2 \tag{12}$$

REFERENCES

1. R. W. Ditchburn, U. Opik, "Atomic and Molecular Processes" ed. D. R. Bates, Academic Press, London (1962).
2. S. Geltman, Phys. Rev., 112, 176 (1958).
3. J. A. R. Samson, J. Op. Soc. Am., 55, 935 (1965).
4. E. W. McDaniel, "Collision Phenomena in Ionized Gases." Wiley, New York (1964).
5. D. R. Bates, Mon. Not. Roy. Astron. Soc., 106, 423 (1946).
6. D. A. S. Vroom, Ph.D. Thesis, The University of British Columbia (1966).
7. A. G. Shenstone, Phys. Rev., 38, 873 (1931).
8. U. Fano, Phys. Rev., 124, 1866 (1961).
9. F. H. Mies, Phys. Rev., 175, 164 (1968).
10. J. N. Bardsley, Chem. Phys. Lett., 2, 329 (1968).
11. A. L. Smith, Phil. Trans. Roy. Soc. Lond., A 268, 169 (1970).

III. PHOTOIONIZATION WITH MOLECULAR BEAMS

I. AUTOIONIZATION STRUCTURE OF NITRIC OXIDE NEAR THE THRESHOLD

ABSTRACT

The photoionization efficiency curve of $NO^+(X^1\Sigma^+)$ was obtained using a molecular beam technique in the wavelength range from 1350Å to 1185Å (9.18-10.46 eV). Due to the lowering of the rotational temperature by supersonic expansion, the autoionization structure superimposed on the vibrational steps is well resolved. This structure is attributed to vibrational autoionization. The splitting of the autoionization peaks due to the spin-orbit ground state ($^2\Pi_{1/2}$, $^2\Pi_{3/2}$) of nitric oxide is observed. The strong intensity peaks of the vibrational autoionization are found to correspond to a vibrational quantum number change of $\Delta v=-1$. The autoionization structure observed on the first four vibrational steps obeys the propensity rule proposed by Berry.[1]

INTRODUCTION

Since advances in vacuum technology and improvements of diffraction gratings have extended high resolution molecular spectroscopy into the vacuum ultraviolet region, many new electronic states and Rydberg series of molecules and atoms have been identified in absorption and emission. However, the absorption of ultraviolet radiation by molecules is observed to be considerably more complex than that of atoms. When the overlapping of discrete energy levels by a continuous range of levels occurs, both autoionization and predissociation can take place and reduce the lifetime of the discrete state, with concomitant broadening of the absorption features. The high resolution photoionization experiment remains one of the most sensitive methods of investigating the ionization processes and coupling mechanisms between the excited Rydberg states and ionic states. Not only does it give precise information on the first and higher ionization potentials of molecules and vibrational frequencies of the ions, but Franck-Condon factors for the direct ionization can also be obtained from the relative height of the steps which appear in the photoion yield curves. The most complete system of Rydberg states for a diatomic molecule other than H_2 and He_2 has emerged in recent years from the study of high resolution emission and absorption spectra of NO, which has been principally carried out by Miescher and his co-workers.[1-5] In a conventional absorption spectroscopic experiment, detection of weak autoionization structure can be difficult. These difficulties are lessened to a great extent in a high resolution photoionization experiment, where the ions are directly detected.

The photoionization of NO has been studied by many investigators in the last 20 years.[6-12] Step function behavior of the photoionization efficiency curve has been demonstrated and the fine structure superimposed upon the steps has also been observed.[11,12] A more detailed investigation of the threshold region was undertaken by Killgoar et. al.[13] only recently. Their experiment was done with a dispersed vacuum ultraviolet light on a gas cell of nitric oxide cooled to 150°K. The autoionizing peaks observed in their work are still relatively broad. Hence, the assignment of the autoionization structure might not be entirely certain. Even though Killgoar et. al. used a dispersed photon beam of about 6 meV resolution, the resolution of their experiment was actually limited by the rotational temperature of NO at 150°K (~13 meV). In order to take full advantage of the energy resolution available by photoionization experiments, the gas cell has to be cooled at least down to 80°K. This is obviously impossible for condensable gases such as NO. One of the most effective methods of surmounting these problems is to employ the supersonic beam technique. We have used this method to obtain the photoionization efficiency curve of NO with our molecular beam photoionization apparatus. The autoionization structure observed is re-interpreted as discussed below.

EXPERIMENTAL

The apparatus used in this work is essentially a normal incidence type vacuum-ultraviolet monochromator (McPherson 225) coupled to a molecular beam chamber as shown in Fig. 1. The photon source is the

many-line pseudo-continuum of H_2 produced by a D.C. capillary discharge. The discharge lamp is made out of quartz, with a 6 mm. O.D. x 4 mm. I.D. discharge capillary surrounded by a 1" O.D. standard wall water jacket. The whole discharge lamp is 11" long. Both the anode and cathode are made out of aluminum and water cooled during the operation of the lamp. Before the main chamber of the monochromator, the source is differentially pumped by a Roots blower and an ejector pump. With the lamp operated at about 5 torr, and with the entrance slit about 100 μ, the monochromator can maintain a vacuum at 5×10^{-6} torr. The intensity of the dispersed light coming out from the exit slit is monitored by a sodium salicylate coated photomultiplier, which is known to have a constant quantum efficiency from 300Å to 1600Å.[14] (The current output from the photomultiplier is usually about 10^{-7} ampere, which is two orders of magnitude higher than the photomultiplier dark current.) The signal from the photomultiplier is measured by a picoammeter. The stability of the discharge lamp is further monitored by taking the analog output of the picoammeter to a strip chart recorder. The grating used in the work is MgF_2 coated, ruled with 1200 lines/mm and blazed at 1200Å. The reciprocal dispersion is 8.3Å/mm, with 100 μ exit and entrance slits, the resolution is about 6 meV. Wavelength calibration was accomplished by using the known emission lines of the hydrogen atom and molecule.

The nitric oxide target gas is introduced in the chamber by supersonic expansion through a 0.005" nozzle with a stagnation pressure of ~350 torr. The beam expansion chamber is pumped by a 10" diffusion pump which maintains a vacuum of 10^{-4} torr. The second differential pumping region in which the beam is collimated is pumped by a 4"

diffusion pump which maintains a pressure of 10^{-5} torr. The main chamber is pumped by two 4" diffusion pumps , and has a pressure of 5×10^{-7} torr when the beam is running. The nitric oxide and photon beams cross in the main chamber at nearly a right angle. The width of both the photon beam and the molecular beam is about 0.3 cm at the collision region. The detector is a quadrupole mass spectrometer which has its axis perpendicular to both the photon beam and the molecular beam. The whole detector is differentially pumped by a 220 l/sec ion pump, which provides the detector with a very high vacuum ($\sim 5 \times 10^{-9}$ torr) when the main chamber is at 5×10^{-7} torr.

The ions generated at the collison center are focused into the mass spectrometer and mass analyzed. The molecular beam is chopped by a 150 Hz tuning fork chopper which generates two gating signals corresponding to the beam on and off. Each gate initiates one of an idential pair of 5 MHz scalers. The difference of the two counters gives the net signal. With the present beam production system, the modulated background is about 5-10% of the signal counts. The monochromator is scanned manually using a 0.5Å interval. At each wavelength, the current reading of the picoammeter which corresponds to the light intensity is recorded. The relative photoionization efficiency curve is thus equal to the ratio of ion signal to the photon signal. After the experiment, the monochromator is scanned down to 600Å where there is no light generated by the H_2 pseudo-continuum, and the current reading of the phototube corresponds to the background of stray photons from the monochromator. All photon signals are corrected for this background. Depending on the intensity of the light, the minimum counting rate is

~10 counts/sec and the maximum counting rate is 2000 counts/sec at the Lyman α. The average counting rate at the vibrational steps is ~50 counts/sec. The whole spectrum is obtained by counting 100 sec at each point.

The vertical cross section of the apparatus showing the experimental arrangement near the collision center is shown in Fig. 2. The photon beam is coming out from the plane of the figure. An electron bombardment type ionizer is coupled to the collision region to check the beam number density and calibrate the mass spectrometer. With the probe of the ionizer, the beam density in general is about 1.5×10^{12} molecules/cc at the collision center.

RESULTS AND DISCUSSION

The photoionization spectrum of NO obtained is shown in Fig. 3. The advantages of combining the photoionization mass spectrometric technique and the molecular beam method are apparent from the sharp features shown in the spectrum. The onset of each vibrational step is extremely sharp. The uncertainty of the rise is less than approximately 0.5Å. In addition to the clear step-function behavior due to the direct ionization process, considerable autoionization structure is well-resolved. The ionization potentials from the two ground spin-orbit ($^2\Pi_{1/2,\ 3/2}$) states to the first four vibrational levels of the ionic state ($^1\Sigma^+$) derived from the middle of the first sharp rise of each vibrational step in the photoionization efficiency curve are listed in Table I. A comparison of the values of the first ionization potential of NO obtained in this and in earlier work is made in Table II. The sharp onsets of the

photoionization efficiency curve observed in this work correspond to ionization potentials from ($X^2\Pi_{3/2}$, v"=0) to the ($X^1\Sigma^+$, v'=0,1,2,3) states, and the ionization potentials from the ($X^2\Pi_{1/2}$, v"=0) state are just 121 cm^{-1} (15 meV)[15] higher. The vibrational spacing is listed and compared the values obtained previously by other methods in Table III. All of them agree very well.

The onset of the ($^1\Sigma^+$, v'=0) state has been examined at three different nozzle pressures and the results are shown in Fig. 4. Curves a, b, and c correspond to nozzle pressures of 100 torr, 300 torr and 450 torr, respectively. They are essentially indistinguishable from each other; i.e., the rotational temperature of the target gas is already as low as ~80°K (the resolution of the photon beam in this work) at a nozzle pressure as low as 100 torr. A 80 torr nozzle beam having a rotational temperature $\lesssim$118°K has already been demonstrated by the photoionization work of Parr and Taylor.[18]

One of the most important pieces of information obtained by examining the photoion spectrum concerns the manner in which the excited Rydberg states of molecules couple with the ionization continuum. The only two well-characterized systems are those of H_2 and O_2. In the case of the hydrogen molecule near threshold, autoionization is purely vibrational induced. The energetics of autoionization involve relaxation of a vibrationally excited core, with the energy being supplied to the Rydberg electron. There have been several theoretical discussions of this problem recently.[17-21] Although different models have been applied to the process, they all come to the conclusion that the autoionization will be most probable for $\Delta v=-1$, considerably less for $\Delta v=-2$, still less

for $\Delta v=-3$, etc. This is what Berry[22] calls the propensity rule. This had been observed earlier in photionization experiments[23,24] and later in absorption spectroscopy.[25]

The fact that high resolution photoion spectrum of H_2 shows no steps in the apparent continuum at any of the thresholds for the formation of vibrationally excited states of H_2^+ indicates nearly complete autoionization. However, the situation is different for NO, which shows step-function structure. Such structure indicates that direct ionization is the dominant process, while autoionization gives only a weak structure superimposed on the steps. Miescher[1] has obtained a high resolution photograph of the absorption spectrum in the 1300Å - 1400Å region and identified several Rydberg series converging to excited vibrational states of the ground $X^1\Sigma^+$ electronic state of the NO ion. Due to the strong absorption background, the identification of the autoionizing lines may not always be feasible, as mentioned above. The energy range of Miescher's work, covers only the first vibrational step ($v'=0$) of the $X^1\Sigma^+$ state. Killgoar et. al.[13] extended the work to the 4th vibrational step ($v'=3$) by a high resolution photoionization experiment. Their assignment to the autoionization structure mainly follows that of Miescher's. Only a few strong autoionizing peaks were assigned as corresponding to a vibrational energy change $\Delta v=-1$. All others were identified as converging to highly excited vibrational states of the ionic $X^1\Sigma^+$ state. Thus, they do not disprove or confirm the propensity rule derived by Berry[17,22] and Bardsley.[18] Miescher has reported that many of the Rydberg series in NO are perturbed. This by no means implies that the predissociation is

strong enough to obscure the autoionizing structure. On the contrary, as argued in the paper of Killgoar et. al.,[13] the Rydberg absorptions converging to v'=1 are expected to be strong.

As can be seen in the photoion yield curve of NO, the autoionization fine structure is relatively weak, yet the peaks are sharp. This permits us to assign the autoionization structure unambiguously. Indeed, the analysis of the spectrum does confirm the strong autoionization structure is favored by the vibrational propensity rule $\Delta v=-1$.

The strong autoionization peaks have been fit with the Rydberg equation $\nu = T_v' - \frac{R}{(n-\delta)^2}$, where T_v' is the ionization potential limit to which the corresponding Rydberg transition converges, R is the Rydberg constant, δ is the quantum defect, n is the principal quantum number, and ν is the peak position. By using the ionization potentials obtained (Table I) in this work as the converging limits T_v', we find that 31 of the strong peaks observed in this work are favored by the vibrational propensity rule $\Delta v=-1$. With a quantum defect δ of 0.87, the predicted and observed autoionization peaks for the first four vibrational steps are listed in Table IV A-VII B. The observed autoionization peaks for the first four vibrational steps are listed in Tables IV A-VII B, where they are compared with the predictions of the Rydberg equation in which the quantum defect δ was 0.87. Predictions and experiments agree to within ~0.5Å, which is the uncertainty of this work. Essentially, on each vibrational step, there are two major series which are separated by about 15 meV. This is exactly the energy separation of the two spin-orbit states ($^2\Pi_{1/2}$ and $^2\Pi_{3/2}$) of the ground state NO molecule after a correction for zero point energy is made. The lower energy series of peaks is derived from the $^2\Pi_{3/2}$

state while the other comes from the $^2\Pi_{1/2}$ state. At room temperature, the population of the $^2\Pi_{3/2}$ state is about 56% of that of the ground state $^2\Pi_{1/2}$. Our observations show that a nozzle pressure of $\leq$ 350 torr is not effective in relaxing the $^2\Pi_{3/2}$ state of NO. The intensities of the doublet peaks will not stand in the ratio of 1:2 because the peak of the lower energy member ($^2\Pi_{3/2} \rightarrow X^1\Sigma^+$) always overlaps the rising edge of higher energy member ($^2\Pi_{1/2} \rightarrow X^1\Sigma^+$). For example, for the doublets on the first two vibrational steps, the higher intensity of the (n=8, v'=1) and (n=8, v'=2) peaks from the $^2\Pi_{3/2}$ state comes from the overlapping of the onset of (n=8, v'=1), and (n=8, v'=2) from $^2\Pi_{3/2}$ state respectively.

Table VIII lists the relative Franck-Condon factor derived in this work and compared with the values obtained by other methods. The accuracy of these values is limited by the autoionizing structure superimposed on the vibrational steps. We adopt the empirical choice of absorption cross-section for direct ionization to be that from base line to autoionization minimum.

In conclusion, we note that our assignments of the autoionization features differ in some respects from those of Killgoar et. al.[13] This reassignment is facilitated by the enhanced resolution of our photo-ionization efficiency curve, which results principally from the rotational cooling achieved by the supersonic expansion. The reassignment has the satisfying aspect that most of the features can be fit with a Rydberg formula in which only one value of the quantum defect is used.

ACKNOWLEDGMENTS

The authors wish to thank Professor Bradley Moore for providing the vacuum ultraviolet monochromator, and Dr. Conway for lending us the discharge lamp power supply. The helpful discussion with Professor W. A. Chupka on the construction of the vacuum ultraviolet light source is greatly appreciated. This research was supported by the Office of Naval Research and the U. S. Energy Research and Development Administration.

REFERENCES

1. E. Miescher, J. Mol. Spectry., 20, 130 (1966).
2. Ch. Jungen and E. Miescher, Can. J. Phys., 47, 1769 (1969).
3. K. P. Huber and E. Miescher, Helv. Phys. Acta., 36, 257 (1963).
4. R. Sutter, Can. J. Phys., 47 881 (1969).
5. Ch. Jungen and E. Miescher, Can. J. Phys., 46, 987 (1968).
6. K. Watanabe, F. F. Marmo, and E. C. Y. Inn, Phys. Rev., 91, 1155 (1953).
7. K. Watanabe, J. Chem. Phys., 22, 1564 (1954).
8. H. Hurzeler, M. G. Inghram, and J. D. Morrison, J. Chem. Phys., 28, 76 (1958).
9. A. J. C. Nicholson, J. Chem. Phys., 39, 954 (1963).
10. A. J. C. Nicholson, J. Chem. Phys., 43, 1171 (1965).
11. R. M. Reese and H. M. Rosenstock, J. Chem. Phys., 44, 2007 (1966).
12. K. Watanabe, F. M. Matsunaga and H. Sakai, Appl. Opt., 6, 391 (1967).
13. P. C. Killgoar, Jr., G. E. Leroi, J. Berkowitz and W. A. Chupka, J. Chem. Phys., 58, 803 (1973).
14. J. A. R. Samson, J. Opt. Soc. Am., 54, 6 (1964).
15. R. H. Gillette and E. H. Eyster, Physic. Rev., 56, 1113 (1939).
16. G. R. Parr and James W. Taylor, Rev. Sci. Instrum., 44, 1578 (1973).
17. R. S. Berry, J. Chem. Phys., 45, 1228 (1966).
18. J. N. Bardsley, Chem. Phys. Letters, 1, 229 (1967).
19. A. Russek, M. R. Patterson and R. L. Becker, Phys. Rev., 167, 17 (1968).
20. S. E. Nielsen and R. S. Berry, Chem. Phys. Letters, 2, 503 (1968).

21. B. Ritchie, Phys. Rev., A3, 95 (1971); A6, 1761 (1972).

22. R. S. Berry and S. E. Nielson, Phys. Rev., A1 (1970) 383, 395.

23. W. A. Chupka and J. Berkowitz, J. Chem. Phys., 48, 5726 (1968).

24. J. Berkowitz and W. A. Chupka, J. Chem. Phys., 51, 2341 (1969).

25. G. Honberg and Ch. Jungen, J. Mol. Spectrosc., 41, 425 (1972).

26. K. P. Huber, Helv. Phys. Acta., 34, 929 (1961).

27. K. Dressler, Astrophys. J., 141, 1266 (1965).

28. K. Watanabe, J. Chem. Phys., 26, 542 (1957).

29. W. C. Walker and G. L. Weissler, J. Chem. Phys., 23, 1962 (1955).

30. M. I. Al-Joboury, D. P. May, and D. W. Turner, J. Chem. Soc., 616 (1965).

31. D. A. S. Vroom, Ph.D. Thesis, The University of British Columbia (1966).

32. M. I. Al-Joboury and D. W. Turner, J. Chem. Soc., 4434 (1964).

33. P. H. Doolittle and R. L. Schoen, Report No. D1-82-0463, Boeing Scientific Research Laboratories, Seattle (1965).

34. G. G. Cloutier and H. I. Schiff, J. Chem. Phys., 31, 793 (1959).

35. H. Lefebvre-Brion and C. M. Mosier, J. Chem. Phys., 44, 2951 (1966).

36. M. E. Wacks, J. Chem. Phys., 41, 930 (1964).

37. E. Miescher, Helv. Phys. Acta., 29, 135 (1956).

38. L. Kerwin, P. Marmet, and E. M. Clarke, "Advances in Mass Spectrometry Vol. II," Pergamon Press, London (1963).

39. M. Halmann and I. Lanlicht, J. Chem. Phys., 43, 1503 (1965).

Table I. Ionization Potentials of Nitric Oxide (ev)
(uncertainty ± 0.003 ev)

Ionic State	$(^2\Sigma_{3/2}, v''=0) \rightarrow (X^1\Sigma^+, v')$	$(^2\Sigma_{1/2}, v''=0) \rightarrow (X^1\Sigma^+, v')$
$X^1\Sigma^+$, $v'=0$	9.256	9.271
$X^1\Sigma^+$, $v'=1$	9.547	9.562
$X^1\Sigma^+$, $v'=2$	9.834	9.849
$X^1\Sigma^+$, $v'=3$	10.115	10.130
$X^1\Sigma^+$, $v'=4$	10.395	10.410

Table II. Comparison of the ionization potentials of $NO(X^2\Pi: v''=0) \rightarrow NO^+(X^1\Sigma^+, v'=0)$

$(^2\Pi_{3/2}, v''=0) \rightarrow (X^1\Sigma^+, v'=0)$	$(^2\Pi_{1/2}, v''=0) \rightarrow (X^1\Sigma^+, v'=0)$	Method and Ref.
9.256 ± 0.003		Photoionization This work
	9.2637 ± 0.0006	Spectroscopic (2)
	9.267 ± 0.005	Spectroscopic (26)
	9.266 ± 0.008	Spectroscopic (27)
9.250 ± 0.005		Photoionization (9)
9.25 ± 0.02		Photoionization (28)
9.20 ± 0.03		Photoionization (29)
9.25 ± 0.03		Photoionization (8)
9.23		Photoelectron (30)
9.32		Photoelectron (31)
9.34		Photoelectron (32)
9.25		Photoelectron (33)
9.25 ± 0.002		Electron Impact (34)
	9.26	Theoretical (35)

Table III. Vibrational Spacing of the Lowest Ionic State ($^1\Sigma^+$) of NO

$\Delta v'$	Calculated[a]	Photoionization[b]	Spectroscopic[c]	Electron Impact[d]	Photoelectron[e]	This work
0-1	0.290	0.290	0.291	0.29	0.30	0.291
1-2	0.287	0.288	0.286	0.26	0.29	0.287
2-3	0.283	0.277	0.283		0.28	0.281
3.4	0.278	0.295	0.278		0.28	0.280

[a]Reference 36

[b]Reference 9

[c]Reference 37

[d]Reference 38

[e]Reference 31

Table IV A. Assignment of Autoionization Structure on the First Vibrational Step of NO^+ ($^1\Sigma^+ \leftarrow {}^2\Pi_{3/2}$)

Observed (Å)	Peaks Predicted by Equation (1) (Å)	δ	Assignment n	Assignment v'
1336.67	1336.12	0.87	8	1
1327.67	1327.31	0.87	9	1
1321.17	1321.35	0.87	10	1
1316.67	1316.95	0.87	11	1
1313.17	1313.88	0.87	12	1

$$h\nu = \left[9.546_8 - \frac{13.607_4}{(n-0.87)^2}\right] \text{eV} \qquad (1)$$

Table IV B. Assignment of Autoionization Structure on the First Vibrational Step of NO^+ ($^1\Sigma^+ \leftarrow {}^2\Pi_{1/2}$)

Observed (Å)	Peaks Predicted by Equation (2) (Å)	δ	Assignment n	Assignment v'
1334.17	1333.96	0.87	8	1
1325.17	1325.18	0.87	9	1

$$h\nu = \left[9.561_8 - \frac{13.607_4}{(n-0.87)^2}\right] \text{eV} \qquad (2)$$

Table V A. Assignment of Autoionization Structure on the Second Vibrational Step of NO^+ ($^1\Sigma^+ \leftarrow {}^2\Pi_{3/2}$)

Observed (Å)	Peaks Predicted by Equation (3) (Å)	δ	Assignment n	Assignment v'
1296.17	1295.94	0.87	8	2
1287.67	1287.62	0.87	9	2
1281.67	1281.95	0.87	10	2
1277.67	1277.90	0.87	11	2
1275.17	1274.91	0.87	12	2

$$h\nu = \left[9.834_5 - \frac{13.607_4}{(n-0.87)^2}\right] \text{eV} \qquad (3)$$

Table V B. Assignment of Autoionization Structure on the Second Vibrational Step of NO^+ $(^1\Sigma^+ \leftarrow ^2\Pi_{1/2})$

Observed (Å)	Peaks Predicted by Equation (4) (Å)	δ	Assignment n	Assignment v'
1293.67	1293.92	0.87	8	2
1285.17	1285.63	0.87	9	2

$$h\nu = \left[9.849_6 - \frac{13.607_4}{(n-0.87)^2}\right] eV \qquad (4)$$

Table VI A. Assignment of Autoionization Structure on the Third Vibrational Step of NO^+ ($^1\Sigma^+ \leftarrow {}^2\Pi_{3/2}$)

Observed (Å)	Peaks Predicted by Equation (5) (Å)	δ	Assignment n	Assignment v'
1259.17	1258.98	0.87	8	3
1250.67	1251.12	0.87	9	3
1245.17	1245.77	0.87	10	3
1241.67	1241.94	0.87	11	3
1233.67	1239.12	0.87	12	3

$$h\nu = \left[10.115_4 - \frac{13.607_4}{(n-0.87)^2}\right] eV \qquad (5)$$

Table VI B. Assignment of Autoionization Structure on the Third Vibrational Step of NO^+ ($^1\Sigma^+ \leftarrow {}^2\Pi_{1/2}$)

Observed (Å)	Peaks Predicted by Equation (6) (Å)	δ	Assignment n	Assignment v'
1256.67	1257.06	0.87	8	3
1249.17	1249.24	0.87	9	3
1243.67	1243.89	0.87	10	3
1240.17	1240.08	0.87	11	3
1236.67	1237.26	0.87	12	3

$$h\nu = \left[10.130_4 - \frac{13.607_4}{(n-0.87)^2}\right] eV \qquad (6)$$

Table VII A. Assignment of Autoionization Structure on the Fourth Vibrational Step on NO^+ ($^1\Sigma^+ \leftarrow {}^2\Pi_{3/2}$)

Observed (Å)	Peaks Predicted by Equation (7) (Å)	δ	Assignment n	Assignment v'
1224.67	1224.20	0.87	8	4
1216.67	1216.77	0.87	9	4
1211.17	1211.70	0.87	10	4
1207.67	1208.08	0.87	11	4

$$h\nu = \left[10.395_2 - \frac{13.607_4}{(n-0.87)^2}\right] eV \qquad (7)$$

Table VII B. Assignment of Autoionization Structure on the Fourth Vibrational Step of NO^+ ($^1\Sigma^+ \leftarrow {}^2\Pi_{1/2}$)

Observed (Å)	Peaks Predicted by Equation (8) (Å)	δ	Assignment n	Assignment v'
1222.17	1222.39	0.87	8	4
1215.17	1214.98	0.87	9	4
1209.67	1209.93	0.87	10	4

$$h\nu = \left[10.410_2 - \frac{13.607_4}{(n-0.87)^2}\right] eV \qquad (8)$$

Table VIII. Relative Transition Probabilities (normalized for v'=1)

v'	Calculated		Photoionization	Photoelectron	This work
	Ref. 36	Ref. 39	Ref. 7	Ref. 31	
0	0.478	0.4781	0.79	0.59	0.70
1	1.000	1.000	1.00	1.00	1.00
2	0.917	0.9170	1.00	0.81	1.03
3	0.484	0.4843	0.67	0.40	0.70
4	0.163	0.1629		0.16	0.28

FIGURES

Figure 1. Schematic diagram of the apparatus (Plane View) (1) McPherson 225 Vacuum UV Monochromator, (2) Differential Pumping System, (3) Entrance Slit, (4) Light Source, (5) Exit Slit, (6) Sodium Salicylate Coated Quartz Window, (7) Photon Detector, (8) Nozzle, (9) Tuning Fork Chopper.

Figure 2. Schematic diagram of the apparatus (Vertical Cross Section View) (1) Nozzle, (2) Skimmer, (3) Tuning Fork Chopper, (4) Quadrupole Mass Spectrometer, (5) Focusing Ion Lenses, (6) Electron Gun.

Figure 3. Photoionization efficiency curve of $NO^+(X^1\Sigma^+)$ in the wavelength range from 1350Å to 1185Å (9.18-10.46 eV).

Figure 4. The onset of the ($X^1\Sigma^+$, v'=0) state at different nozzle pressures. (a) 100 torr, (b) 300 torr, (3) 450 torr.

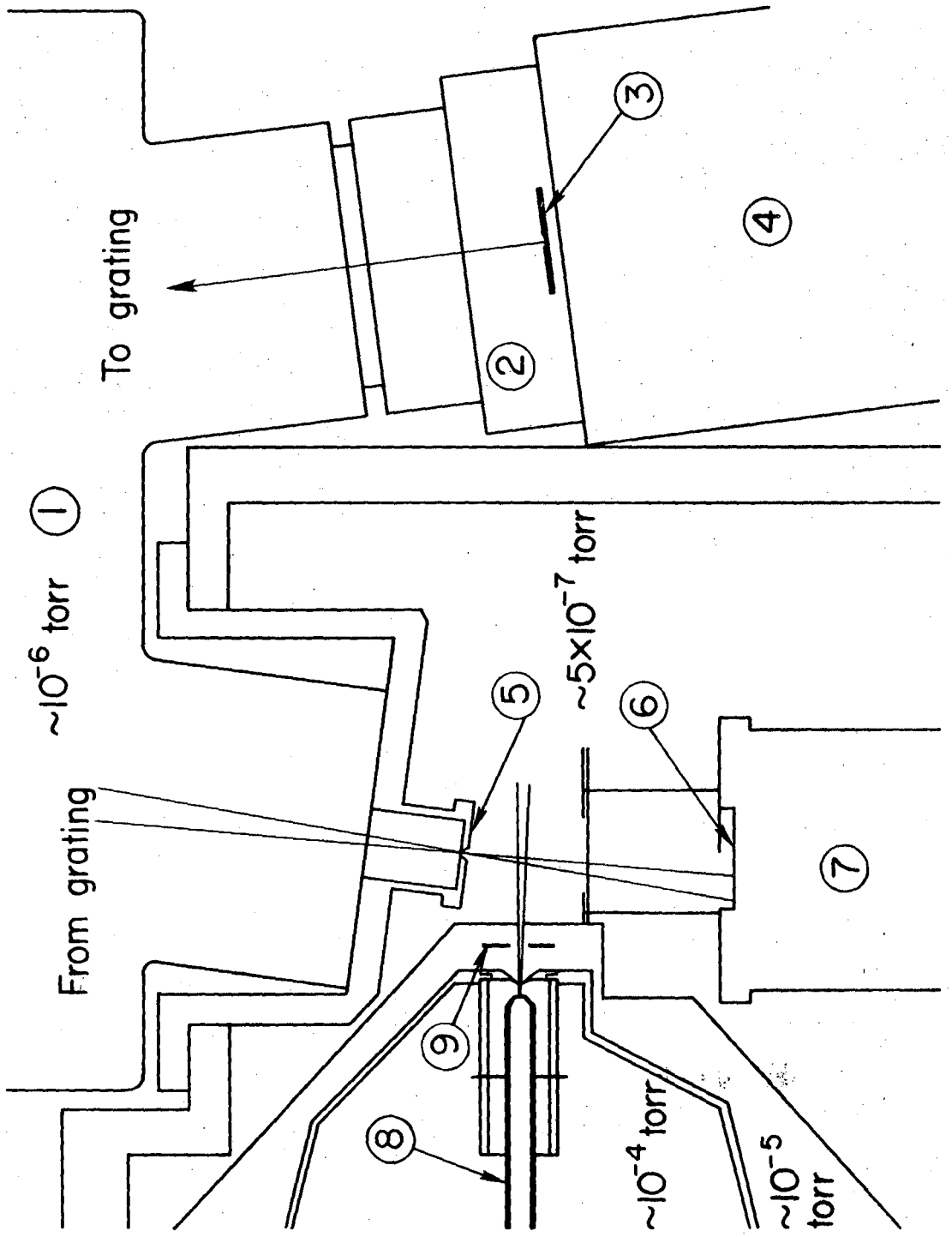

XBL 764-2667

Fig. 1

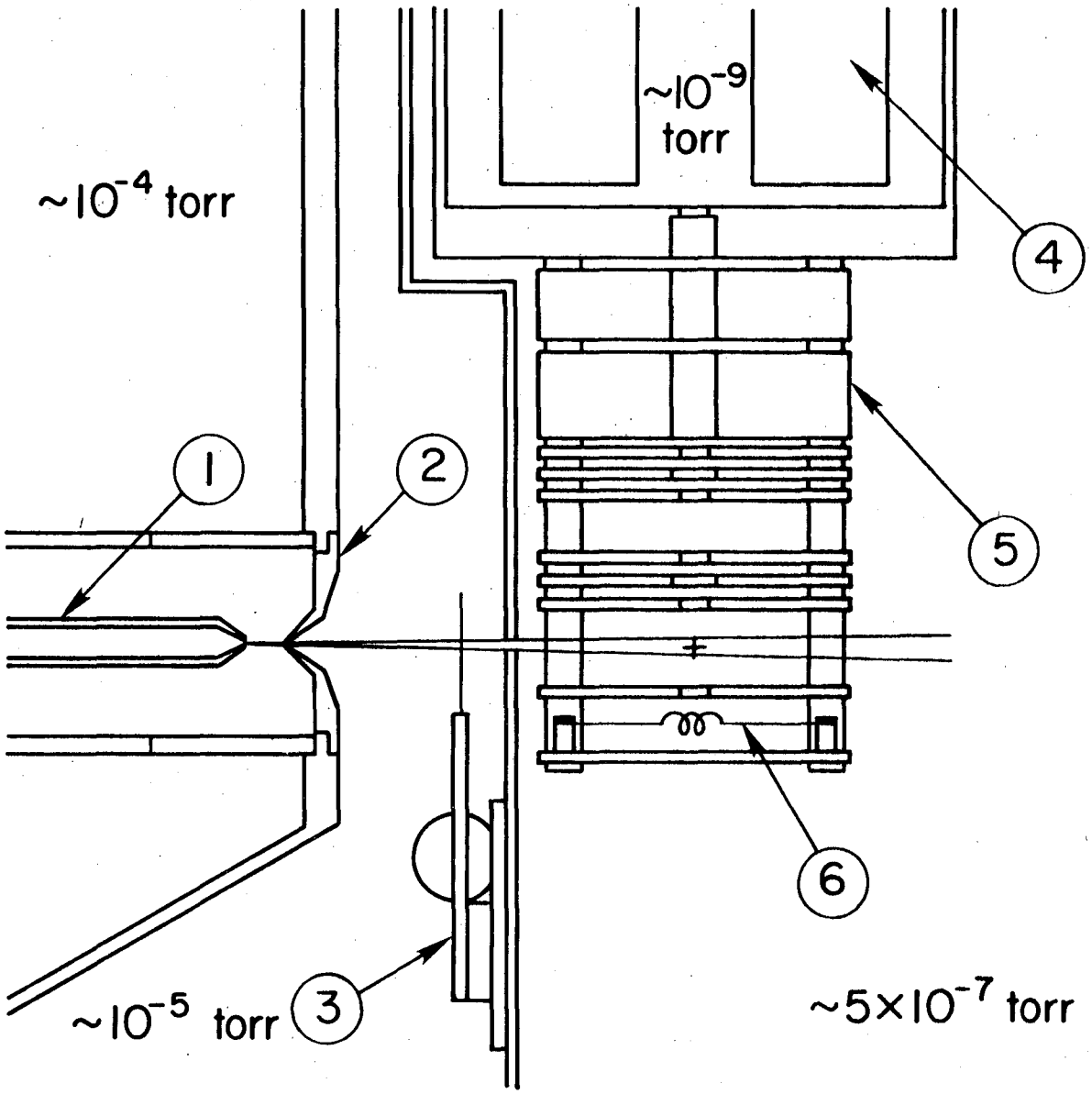

XBL 764-2666

Fig. 2

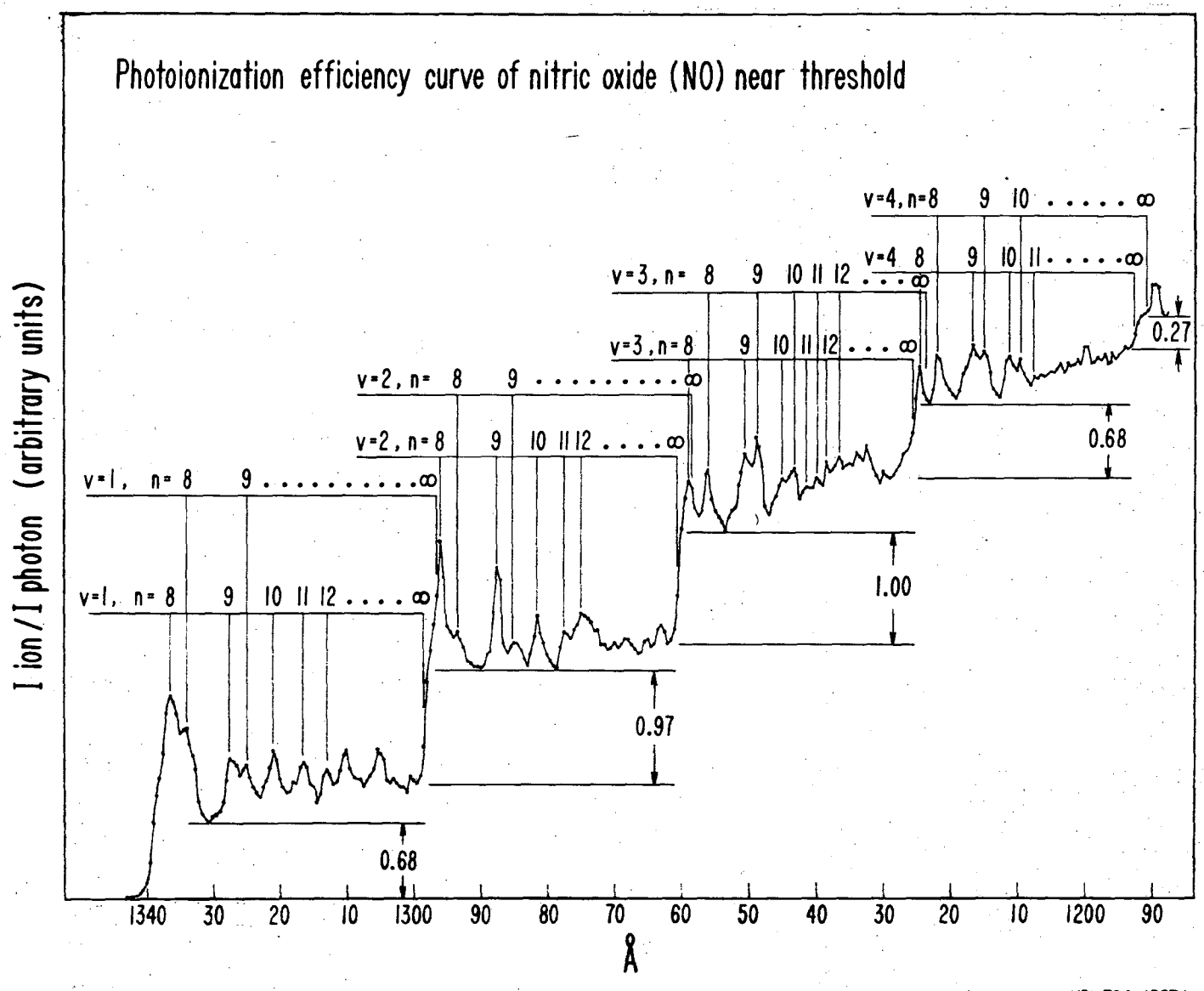
Photoionization efficiency curve of nitric oxide (NO) near threshold
I ion / I photon (arbitrary units)
v=4, n=8 9 10 . . . . . ∞
v=4 8 9 10 11 . . . . ∞
v=3, n= 8 9 10 11 12 . . . ∞
v=3, n=8 9 10 11 12 . . . ∞
v=2, n= 8 9 . . . . . ∞
v=2, n=8 9 10 11 12 . . . . ∞
v=1, n= 8 9 . . . . . ∞
v=1, n= 8 9 10 11 12 . . . . ∞
0.27
0.68
1.00
0.97
0.68
1340 30 20 10 1300 90 80 70 60 50 40 30 20 10 1200 90
Å
XBL 764-1087A

Fig. 3

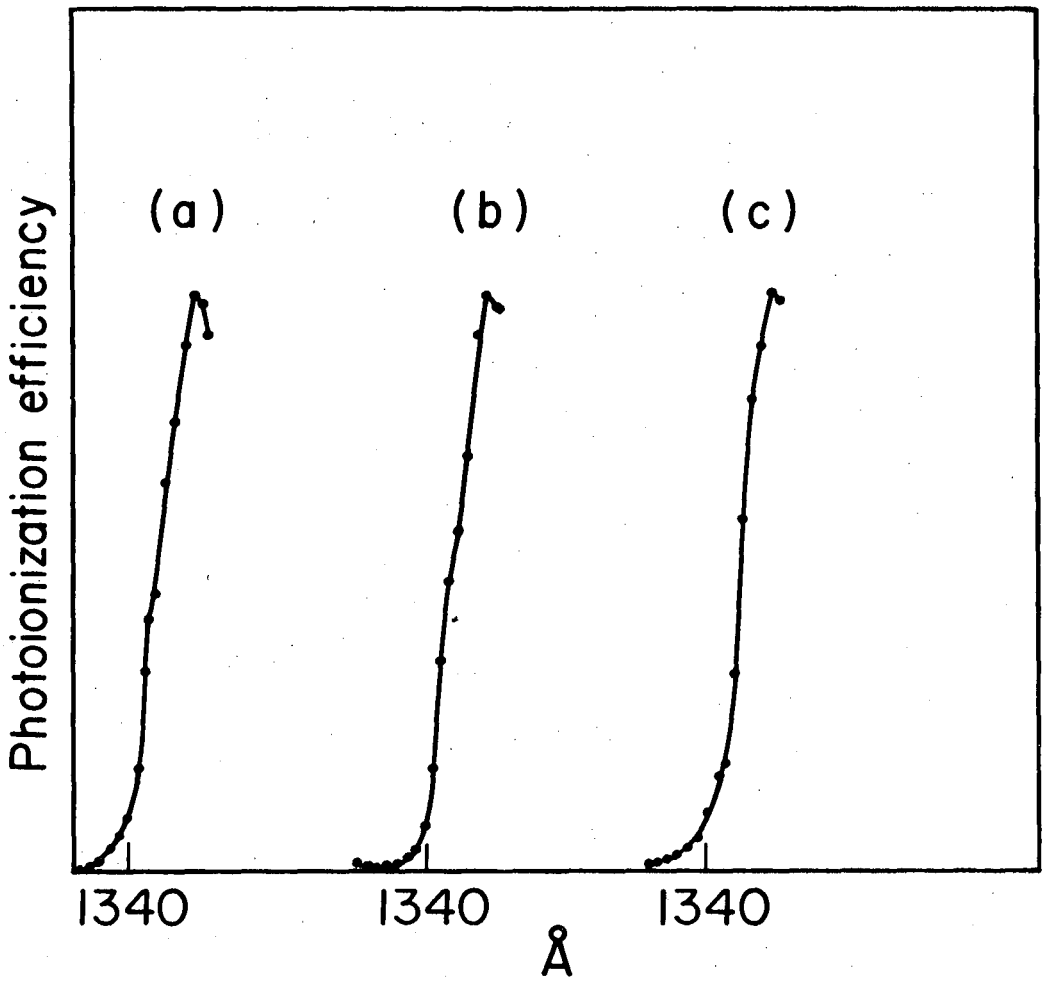

XBL 764-2665

Fig. 4

IV. THE BINDING ENERGY BETWEEN NO AND NO^+

ABSTRACT

The photoionization efficiency curve of the nitric oxide dimer $(NO)_2$ was obtained in the wavelength range from 1420Å to 1230Å (8.731 eV - 10.080 eV). The ionization potential of $(NO)_2$ was found to be 8.752 eV ± 0.008 eV. From the structure of the photoion yield curve of $(NO)_2$, $NO(^2\Pi, v''=0)$-$NO^+(X^1\Sigma^+, v')$ is found to be bound when $NO^+(X^1\Sigma^+)$ is in v'=0 or 1 vibrational state. From this and the dissociation energy of $(NO)_2$ (0.069 eV ± 0.003 eV) obtained by Billingsley and Callear, the dissociation energy of $NO(^2\Pi, v''=0)$-$NO^+(X^1\Sigma^+, v'=0)$ is deduced to be 0.573 eV ± 0.008 eV.

INTRODUCTION

The important role played by the nitric oxide dimer in many atomic and molecular processes has been recognized recently. For example, the chemiluminous reaction $(NO)_n + O \rightarrow NO_2^* + (NO)_{n-1}$ is found to be several orders of magnitude faster than the three body reaction of $NO + O + M \rightarrow NO_2^* + M$.[1-3] Both the rapid vibrational relaxation of nitric oxide[4] and anomalous thermodynamic properties of gaseous nitric oxide at low temperatures[5-8] are attributed to the existence of $(NO)_2$. The nitric oxide dimer $(NO)_2$ in the gas phase has been directly observed by mass spectrometric sampling of an expanding NO jet[9-10] using an electron bombardment type ionizer. From studies of the ultraviolet spectrum[11-12] and infra-red transitions of the dimer in the gas phase,[13] the heat of formation of the dimer has been estimated to be 2.45 kcal/mol. The structure of the nitric oxide dimer $(NO)_2$ has been determined in the gas phase by infrared measurements,[13] and in the solid state by x-ray crystallography.[14-15] It is found that $(NO)_2$ has a nearly rectangular cis configuration. In this work we report the first photoionization study of $(NO)_2$. One of the main reasons for this study was to determine the binding energy between NO and NO^+. If the ionization mechanism of $(NO)_2$ is such that only one of the NO molecules in the dimer is being excited to the different vibrational states of $NO^+(X^1\Sigma^+)$, we would expect to see the same step-function behavior that is observed in the photoionization efficiency curve of NO alone. Furthermore, since the intermolecular energy transfer in the $NO\text{-}NO^+(^1\Sigma^+v')$ complex is expected to be faster than the ion

transit time to the detector (~10^{-6} sec), if the energy of a certain vibrational level of $NO^+(^1\Sigma^+)$ is greater than the binding energy of $NO\text{-}NO^+$, the complex will no longer be stable. Thus the number of steps observed in the photoionization efficiency curve will be related to the binding energy of $NO\text{-}NO^+(^1\Sigma^+)$. It is with this expectation that the photoionization study of $(NO)_2$ has been carried out.

EXPERIMENTAL

The experimental apparatus is essentially the same as that described previously.[16] Modifications were made such that the system can now be operated automatically.[17] A stepping motor was installed in the McPherson 225 one meter monochromator. When the machine was operated in the automatic mode, the ion counters and the photon counter counted for a preset time at a certain wavelength and then the signals were printed out by a printer. Immediately after the printing, the stepping motor advanced upward or downward by a preset number of steps which corresponded to a certain increment of wavelength, and the scalers were reset and restarted simultaneously. The hydrogen many-line pseudo-continuum was used as the light source. The grating used was coated with MgF_2 and has 1200 lines/m.m. With the 300μ entrance and exit slits used in this experiment, the resolution was about 2.49Å (i.e. ~16 meV at 1400Å). The nitric oxide used in this experiment was C.P. grade (99% minimum in purity) obtained from Matheson without further purification. A nozzle 0.127 mm in diameter was used. The photo-

ionization efficiency curve of $(NO)_2$ was obtained with a nozzle stagnation pressure of 600 torr. The monochromator was scanned automatically at 1Å intervals, and at each wavelength, the scalers were set to count for 300 sec. The counting rates varied from about 0.5 count/sec to 5 counts/sec. Wavelength calibration was accomplished by using the known emission lines of the hydrogen atom and molecule. The photon signal has been corrected for the background of stray photons from the monochromator.

RESULTS AND DISCUSSION

The percentage of concentration of nitric oxide dimer versus nozzle stagnation pressure of nitric oxide at room temperature was obtained at 1215.7Å (Lyman α). The results shown in Fig. 1 are calculated with the assumption that the photoionization cross section of $(NO)_2$ is twice that of NO. It has been shown that when a gas is adiabatically expanded from a high pressure gas reservior into a vacuum, association of the molecules occurs as a first step in the condensation process.[18-19] Due to adiabatic cooling, the gas jet after expansion consists of a higher percentage of dimer as compared to the percentage before expansion. For a given gas, the degree of cooling through the expansion depends strongly on the parameter $P_o \cdot D_o$, where P_o is the nozzle stagnation pressure and D_o is the diameter of the nozzle. It is seen that the concentration of the $(NO)_2$ dimer relative to the monomer, NO, rises with increasing pressure. No attempt has been made to analyze the dimer formation in

the expanding gas beam of NO. However, it was found that with the present beam production arrangement, the concentration of $(NO)_2$ is approximately proportional to P_o^2.

The photoion yield spectrum of $(NO)_2$ obtained is shown in Fig. 2. The photoionization efficiency curve of NO is also plotted for comparison. The ionization potential of $(NO)_2$ obtained in this work is equal to 8.752 eV ± 0.008 eV, which is 0.504 eV ± 0.008 eV lower than the I.P. of the NO molecule[16] (9.256 eV ± 0.003 eV). The standard deviation of the photoionization efficiency at several points is shown in Fig. 2. Due to the small counting rate of $(NO)_2^+$, the average standard deviation of this spectrum is as high as 15-20%. This prevents us from analyzing the fine structure of the spectrum.

The photoionization efficiency curve of NO has been found to follow predominately a step-function behavior which corresponds to direct ionization of NO (v"=0) to NO^+ ($X^1\Sigma^+$, v'=0,1,2,3,4 etc). Although the stability of $(NO)_2$ is attributed to a weak "chemical bond" which arises from electron pairing between two ($^2\Pi$) NO molecules, the coupling between the two interacting NO molecules will still be weak. The unpaired electron will mainly be localized on each NO molecule. Thus when a photon comes in and knocks out an electron, the ionization process is expected to be similar to that of NO alone. The only difference is that the ionization potential of the $(NO)_2$ will be shifted to lower energy due to the interaction of the ion with its partner NO molecule. However, in the photoion yield curve of $(NO)_2$, only two steps are clearly resolved. They are separated by 0.290 eV, which is the vibrational quantum of the NO molecule.

In order to explain the observed features in the photoionization efficiency curve of (NO), schematic representations of the potential energy curves for $(NO)_2$ and $(NO)_2^+$ are shown in Fig. 3. The quantities ε and ε^+ are the dissociation energies of NO-NO and NO-NO^+, respectively. The ionization process of $(NO)_2$ involves ejecting an antibonding electron which is associated with one of the NO molecules. This can result in the excitation of the stretching vibrational mode of NO^+. The onset of the first step in the photoion yield curve (i.e. the I.P. of $(NO)_2$) can be attributed to the ionization threshold of $(NO)_2$ to form NO-NO^+ (v=0). The onset of the second step is then equal to the I.P. of $(NO)_2$ to form NO-NO^+ (v=1). With this model, the nonexistence of the third step in the photoion yield curve implies that NO-NO^+ (v=2) has an energy larger than the ion-neutral bond energy. Intramolecular energy transfer is expected to be fast and the dimer dissociates in less than $\sim 10^{-6}$ sec (i.e. the estimated flight time from the ionizing region to the entrance of the quadrupole mass spectrometer). Thus we have

$$(NO\text{-}NO) + h\nu \longrightarrow NO\text{-}NO^+ \ (v=2) \xrightarrow{\leq 10^{-6} \text{ sec}} NO + NO^+ + K.E.$$

The charge exchange cross section between the neutral NO molecule and the NO^+ molecular ion is expected to be large. This does not change any of the argument presented above. The fact that NO-NO^+ (v=1) is bound but NO-NO^+ (v=2) is not, permits a measurement of the well depth of (NO-NO^+). The minimum well depth for the NO and NO^+ interaction is 0.290 eV ± 0.008 eV (ε^+_{min}) and the maximum is estimated to be 0.580 eV ± 0.008 eV (ε^+_{max}), which correspond to the vibrational

energies of NO^+ (v=1) and NO^+ (v=2), respectively. From Fig. 3, the following relation can be derived:

$$\varepsilon^+ + I.P.((NO)_2) = I.P.(NO) + \varepsilon \qquad (1)$$

Using ε^+_{max} and substituting into equation (1), an upper bound for the dissociation energy of $(NO)_2$ is found to be 0.076 eV ± 0.008 eV. On the other hand, with the value of 0.069 eV ± 0.004 eV for the dissociation energy of $(NO)_2$ as determined by Billingsley and Callear, we would obtain a value of 0.573 eV ± 0.008 eV for the dissociation energy of $(NO\text{-}NO^+)$. This certainly lies within our estimates.

ACKNOWLEDGEMENTS

This research was supported by the Office of Naval Research and the U. S. Energy Research and Development Administration.

REFERENCES

1. A. Fontijin and D. E. Rosner, J. Chem. Phys., 46, 3275 (1967).
2. D. Golomb and R. E. Good, J. Chem. Phys., 49, 4176 (1968).
3. M. Bodenstein, Helv. Chim. Acta, 18, 745 (1935).
4. J. Billingsley and A. B. Callear, Nature, 221, 1136 (1969).
5. O. K. Rice, J. Chem. Phys., 4, 367 (1936).
6. R. L. Scott, Mol. Phys., 11, 399 (1966).
7. E. A. Guggenheim, Mol. Phys., 10, 401 (1966).
8. E. A. Guggenheim, Mol. Phys., 11, 403 (1966).
9. T. A. Milne and F. T. Greene, J. Chem. Phys., 47, 3668 (1967).
10. R. E. Leckenby and E. J. Robbins, Nature, 207, 1253 (1965); Proc. Roy. Soc., (London) 291A, 389 (1966).
11. J. Billingsley and A. B. Callear, Trans. Faraday Soc., 67, 589 (1971).
12. L. D'Or, A. deLattre and P. Tarte, J. Chem. Phys., 19, 1064 (1951).
13. C. E. Dinerman and G. E. Ewing, J. Chem. Phys., 53, 626 (1970).
14. W. J. Dulmage, E. A. Meyers and W. N. Lipscomb, Acta Cryst., 6, 760 (1953).
15. W. N. Lipscomb, F. E. Wang, W. R. May and E. Lippert, Jr., Acta Cryst., 14, 1100 (1961).

16a. C. Y. Ng, B. H. Mahan and Y. T. Lee, J. Chem. Phys., to be published.

b. C. Y. Ng, D. J. Trevor, B. H. Mahan and Y. T. Lee, J. Chem. Phys., to be published.

17. C. Y. Ng, Ph.D. Thesis, University of California, Berkeley (1976).
18. F. T. Greene and T. A Milne, J. Chem. Phys., 39, 3150 (1963).
19. R. E. Leckenby, E. J. Robbins and P. A. Trevalion, Proc. Roy. Soc. A, 280, 409 (1964).

FIGURES

Fig. 1. Variation of concentration of nitric oxide dimer with nozzle stagnation pressure at room temperature as probed at Lyman α (1215.66Å). The dashed line is the best fit to the experimental points, and is given by % of $(NO)_2 = (7.97 \times 10^{-4}) [P_o \cdot D_o]^2$ where P_o is the nozzle stagnation pressure in torr, and D_o is the nozzle diameter (0.0127 cm).

Fig. 2. Photoionization efficiency curve of $(NO)_2$ in the wavelength range from 1230Å to 1425Å (10.080 eV - 8.700 eV).

Fig. 3. Schematic representation of NO + NO and NO + NO^+ potential energy curves. ε^+ and ε denote the dissociation energies of $(NO)_2^+$ and $(NO)_2$, respectively.

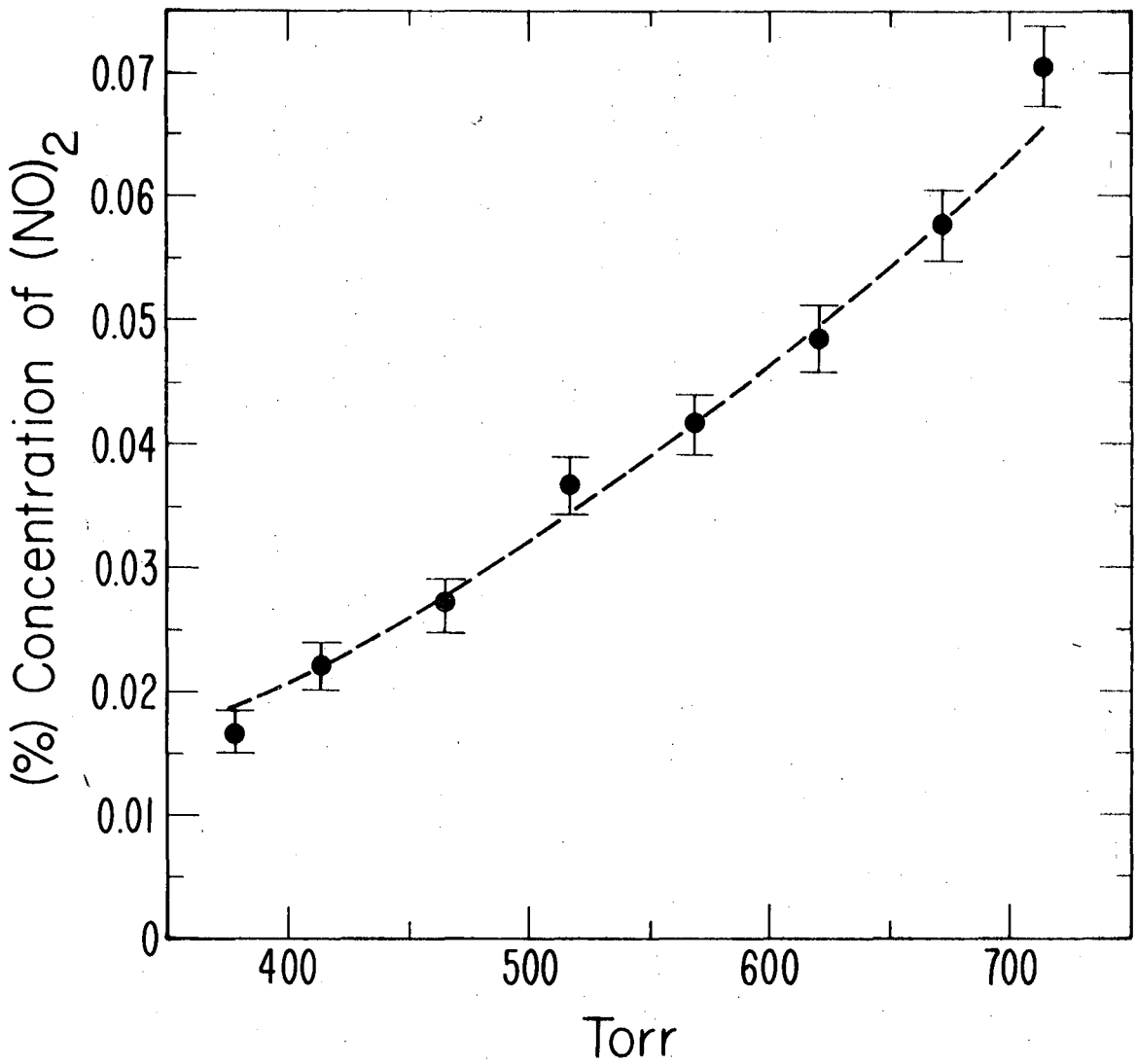

XBL 767-3201

Fig. 1

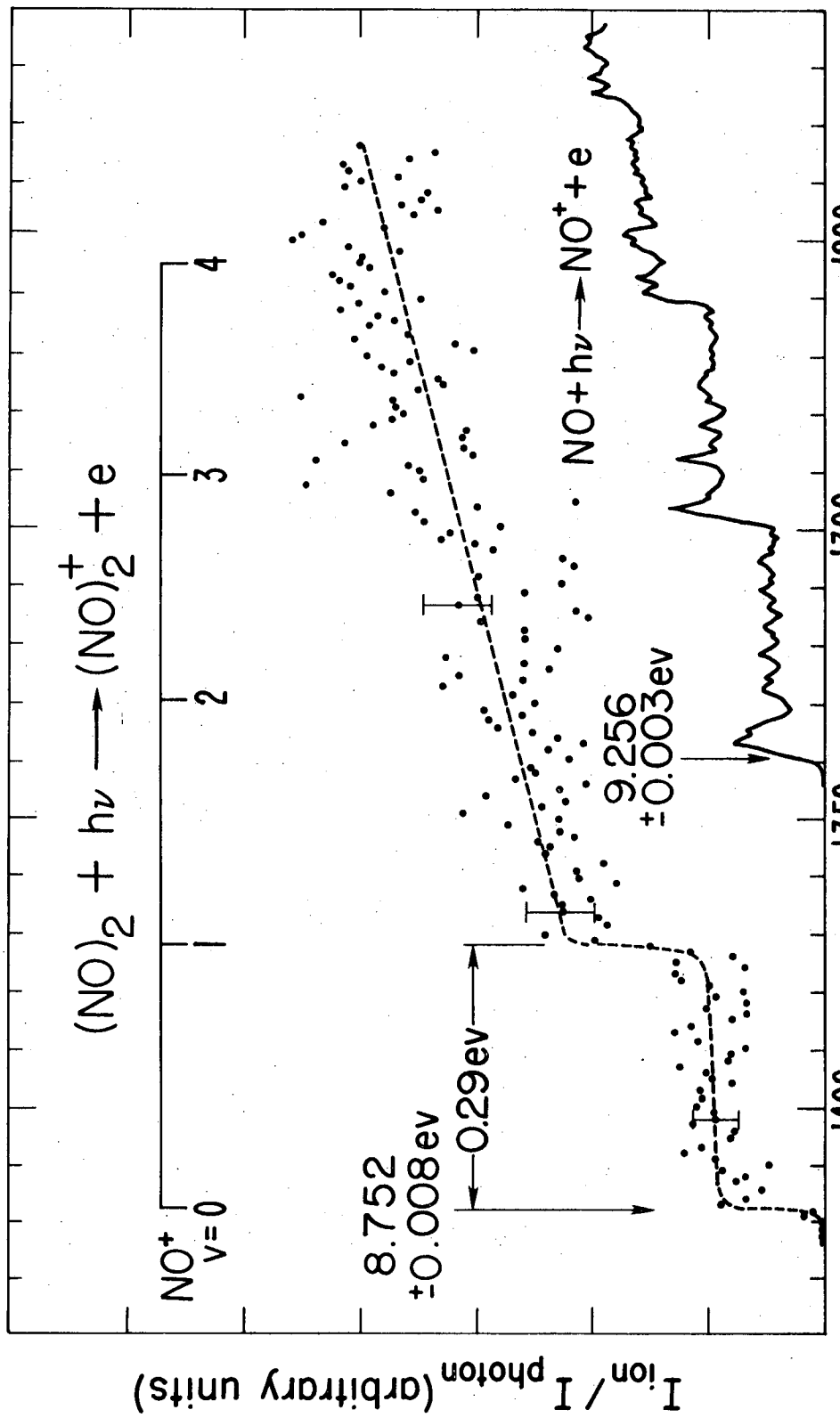

XBL 767-8667

Fig. 2

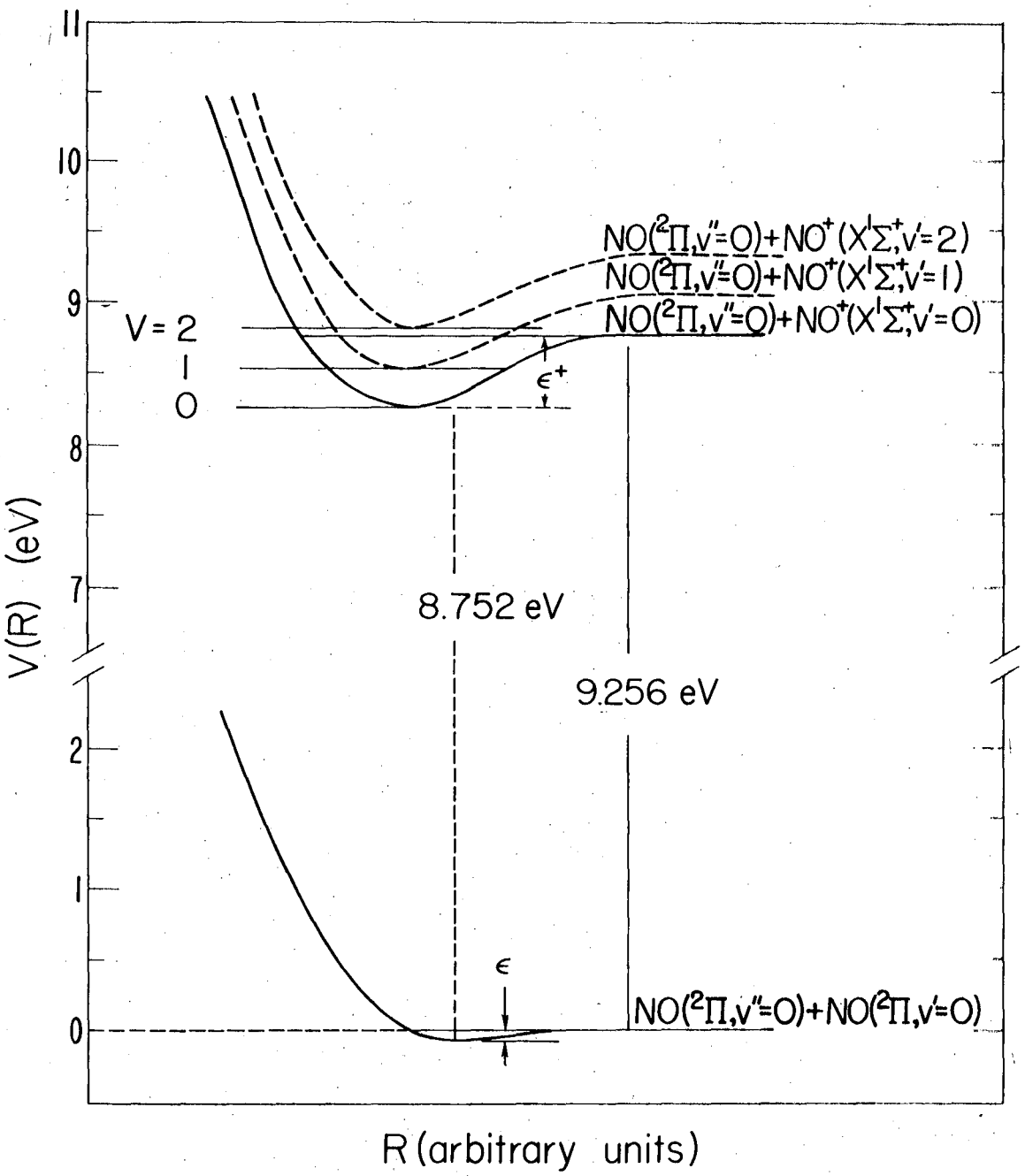

XBL 767 8666

Fig. 3

V. PHOTOIONIZATION STUDIES OF THE Xe_2, Kr_2 AND Ar_2 VAN DER WAALS MOLECULES

A. Photoionization Study of the Xe_2 Van Der Waals Molecule*

The dissociation energy D_o of the Xe_2^+ ion has been estimated from mass spectrometric electron impact appearance potentials[1,4] and photoionization methods.[2,3] In the work of Huffman and Katayama,[2] the lower bound for D_o was estimated to be 0.967 eV from the difference between the threshold energy of the photon induced associative ionization process $Xe^* + Xe \rightarrow Xe_2^+$ and the ionization potential of Xe. In the work of Samson and Cairns,[3] the ionization potential of Xe_2 was obtained by photoionization in a high pressure gas cell, where the mechanism of producing Xe_2^+ was predominately the same associative ionization process. From such experiments D_o was found to be 0.99 ± 0.02 eV. In this work, we report the first direct photoionization studies of the van der Waals molecule Xe_2.

The experimental apparatus and procedures were essentially the same as previous described.[5] Briefly, the apparatus consisted of a hydrogen lamp, a vacuum ultraviolet monochromator, a quadrupole mass spectrometer and a modulated molecular beam production system. The light intensity was monitored by a sodium salicylate coated photomultiplier. The spectrometer grating is ruled with 1200 lines/mm and has a reciprocal dispersion of 8.3 Å/mm. The Xe_2 van der Waals molecules were prepared by supersonic expansion of Xe through a ~0.005" diameter nozzle with a stagnation pressure of ~350 torr at room temperature. The beam of Xe_2

*Submitted to Journal of Chemical Physics for publication.

molecules together with Xe atoms then intersected the dispersed vacuum ultraviolet photon beam at a distance of approximately 3 inches from the nozzle, after two stages of differential pumping. The ions produced were focused and mass analyzed. The number density at the collision center as probed by an electron gun was approximately 1.5 x 10^{12} atom/cc for Xe. The counting rate of Xe_2^+ at 1020Å was about 10% that of Xe^+. Assuming the photoionization cross section of Xe_2 is twice that of Xe, the Xe_2 molecules formed comprise roughly 5% of the beam (~7.5 x 10^{10} molecule/cc).

The photoionization efficiency curve obtained for Xe_2 is shown in Fig. 1(a) and 1(b). In Fig. 1(a), the photoion yield curve was obtained with 300μ entrance and exit slits corresponding to a resolution of 2.5Å (~25 meV). Data were taken at intervals of 1Å, counts being collected for 100 sec at each point from 965Å to 1100Å, while each point was counted for 200 sec in the range from 1110Å to 1118Å where the photoionization efficiency is low. Counting rates varied from 100 counts/sec to ~0.5 counts/sec. Between 965Å and 1080Å, the standard deviations were better than 4%. No ions were observed at wavelengths greater than 1114.3Å, and this can be taken to be the adiabatic ionization potential of Xe_2, with an uncertainty of ± 1Å. This value together with the ionization potential of Xe and dissociation energy of Xe_2 (~24 meV)[6] gives 1.03 ± 0.01 eV as the dissociation energy D_0 for Xe_2^+. We note that our result is somewhat larger than the value given by Samson and Cairns.[3]

The photoionization efficiency of Xe_2^+ increases very slowly from the threshold up to 1080Å, and then increases dramatically with the

autoionization structure dominating the spectrum. A small Franck-Condon factor for direct ionization is to be expected, since the ground state of Xe_2 is essentially a repulsive state with a shallow van der Waals well (~24 meV) and an equilibrium internuclear distance (R_e) of approximately 4.4Å,[6] whereas the Xe_2^+ ground state is bound with R_e estimated to be about 2.85Å.[7] The amount of Xe_2^+ produced by associative ionization of normal and excited Xe atoms in the beam is negligible under our experimental conditions. The photoion yield curve does not show the same structure as the work of Huffman and Katayama.[2] This indicates that the Xe_2^+ we observed is not formed by secondary processes, but rather by Xe_2 molecules which are synthesized by supersonic expansion.

In order to examine the coupling between the molecular excited Rydberg states and the molecular ionic states, of Xe_2, the photoionization efficiency curve was measured again with 100μ exit and entrance slits (i.e. ~10 meV resolution). With these narrower slits, the counting rate at a particular wavelength setting decreased by nearly one order of magnitude. Data were taken at 0.5Å intervals with a 200 sec counting time for each point. The results are shown in Fig. 1(b), where much detailed structure is evident. This spectrum was scanned twice and all the structure was found to be reproducible. In order to verify the wavelength calibration, the ionization threshold of Xe^+ was also measured and the data is shown in Fig. 1(a). The ionization potential of atomic xenon in this work is found to be 1022.3Å which is in good agreement with spectroscopic values.[8] The standard deviations at several points are shown on the graph.

An attempt was made to assign the excited atomic levels to which the molecular Rydberg states are correlated upon dissociation. In the Franck-Condon transition region of Xe_2, i.e. the neighborhood of the equilibrium distance for the ground state, the molecular states should correspond to the Hund-Mulliken case (c).[9] The ground state of Xe_2 has closed electronic shells, and thus is a 0_g^+ state. By the selection rules of case (c), transitions for 0_g^+ to 0_u^+ or 1_u excited molecular states are the only ones which are electric dipole allowed. All the excited atomic states (except those with J=0) can couple with the ground state Xe atom ($5_p^6\ ^1S_o$) to give an 0_u^+ and/or an 1_u molecular state. This makes the assignments of excited atomic states to the corresponding excited molecular states nearly impossible within the present resolution of our experiment. Only the electric dipole allowed atomic Rydberg series[8] are shown in Fig. 1(b). For example, between the $10s\left[\frac{3}{2}\right]_1^\circ$ and $8d\left[\frac{1}{2}\right]_1^\circ$ where the strongest observed autoionization peak is located in this spectrum, there exist a total of 14 other excited atomic levels which can couple with the ground atomic state to give excited molecular states 1_u and/or 0_u^+. The number of possible atomic states increases as one approaches the ionization threshold of the xenon atom.

ACKNOWLEDGEMENT

This work was done with support from the U. S. Energy Research and Development Administration.

REFERENCES

1. M. S. B. Munson, J. L. Franklin, and F. H. Field, J. Phys. Chem., 67, 1542 (1963).
2. R. E. Huffman and D. H. Katayama, J. Chem. Phys., 45, 138 (1966).
3. J. A. R. Samson and R. B. Cairns, J. Opt. Soc. Am., 56, 1140 (1966).
4. J. A. Hornbeck and J. P. Molnar, Phys. Rev., 84, 621 (1951).
5. to be published in J. Chem. Phys.

6a. J. A. Baker, R. O. Watts, J. K. Lee, T. P. Schafer and Y. T. Lee, J. Chem. Phys., 61, 308 (1974).

b. G. C. Maitland and E. B. Smith, Chem. Phys. Lett., 22, 443 (1973).

7. R. S. Mulliken, J. Chem. Phys., 52, 5170 (1970).
8. C. E. Moore, Atomic Energy Levels, NBS Circ., 467, Vol. III, (1949).
9. R. S. Mulliken, Rev. Mod. Phys., 3, 89 (1931); 4, 1 (1932).

FIGURE CAPTIONS

Fig. 1. Photoionization efficiency curve of Xe_2. (a) Photoion yield curve obtained with 300μ entrance and exit slit. (b) Photoion yield curve obtained with 100μ entrance and exit slit.

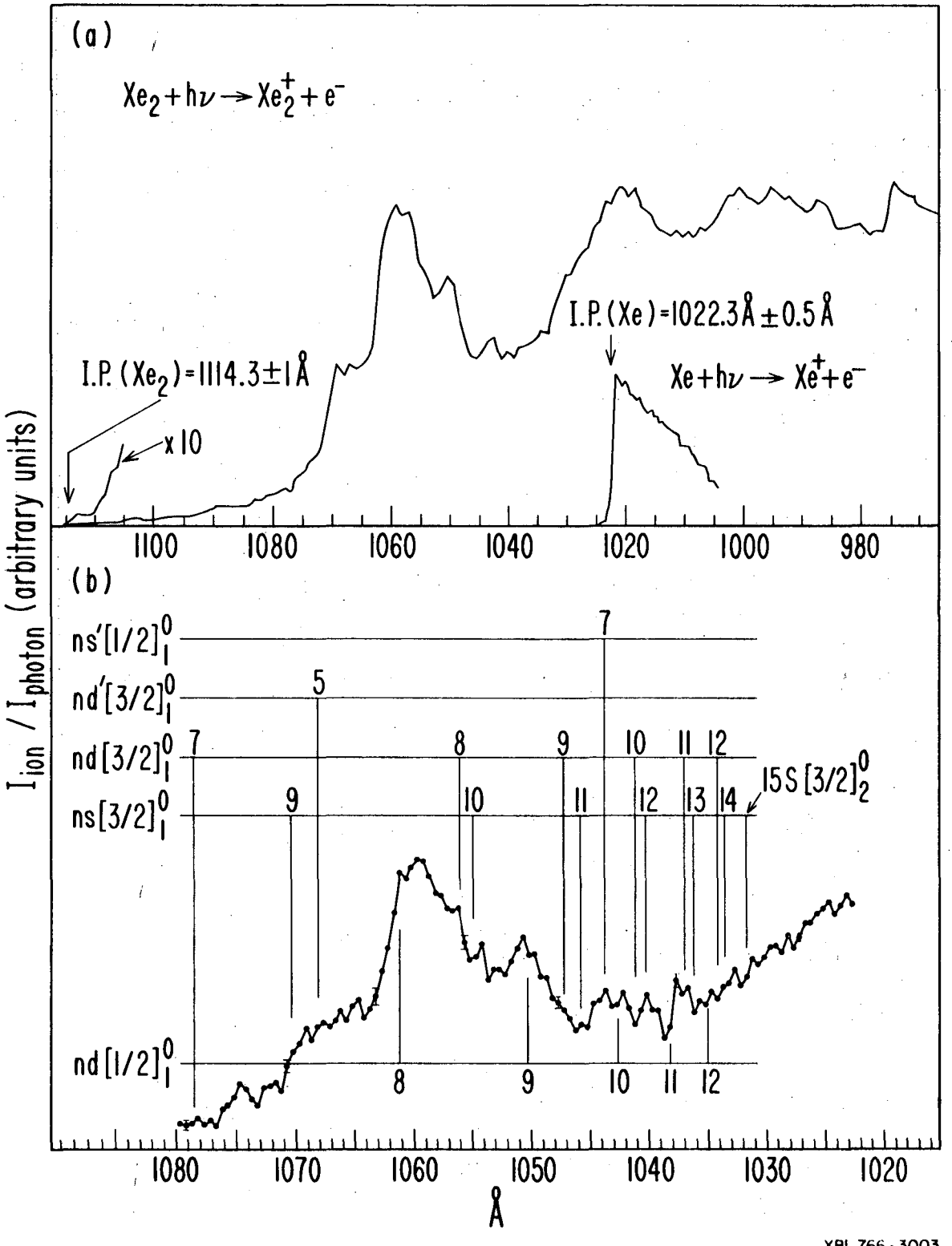
(a)
$Xe_2 + h\nu \rightarrow Xe_2^+ + e^-$
I.P. (Xe_2) = 1114.3 ± 1 Å
x 10
I.P. (Xe) = 1022.3 Å ± 0.5 Å
$Xe + h\nu \rightarrow Xe^+ + e^-$
1100
1080
1060
1040
1020
1000
980
(b)
$ns'[1/2]^0_1$
$nd'[3/2]^0_1$
$nd[3/2]^0_1$
$ns[3/2]^0_1$
$nd[1/2]^0_1$
$15S[3/2]^0_2$
I_{ion} / I_{photon} (arbitrary units)
1080
1070
1060
1050
1040
1030
1020
Å
XBL 766-3003

Fig. 1

B. Photoionization Studies of the Kr_2 and Ar_2 Van Der Waals Molecules*

ABSTRACT

The photoionization efficiency curves of the Kr_2 and Ar_2 van der Waals dimers were obtained with the molecular beam technique in the wavelength range from 850 to 965Å (12.848 - 14.586 eV) and from 750 to 855Å (14.501 - 16.531 eV) respectively. The ionization potential of Kr_2 was found to be 12.86 ± 0.015 eV (963.7 ± 1.2Å), which agrees with the value obtained by Samson and Cairns. The ionization potential of Ar_2 was found to be 14.44 ± 0.02 eV (852.7 ± 1.2Å). Using the known ground state dissociation energies of Kr_2 and Ar_2, the dissociation energy of Kr_2^+, $D_o(Kr_2^+)$, is deduced to be 1.12 ± 0.02 eV and that for Ar_2^+, $D_o(Ar_2^+)$, is 1.31 ± 0.02 eV. The photoion yield curves of Kr_2 and Ar_2 are compared with that of Xe_2. Prominent autoionization structure was observed to correspond to Rydberg molecular states which are derived from the combination of a normal and an excited atom in the $4p^5ns$ (or $4p^5nd$) configuration for Kr and $3p^5ns$ (or $3p^5nd$) configuration for Ar.

*Submitted to Journal of Chemical Physics for publication.

INTRODUCTION

The existence of stable Ar_2 molecules has long been postulated to account for the negative second virial coefficient of Ar at low temperatures. Recently, Milne and Greene[1] as well as many other workers have observed the formation of argon dimers and polymers in supersonic gas jets of Ar. In a mass spectrometric investigation, Leckenby et. al.[2] also observed strong evidence for dimers such as Ar_2, Xe_2, etc. Reliable information on the interaction potentials for the rare gas symmetric pairs has become available in recent years from molecular beam differential and total cross sections measurements,[3] careful analysis of transport phenomena and macroscopic properties,[4] and high resolution vacuum UV absorption spectra.[5] The high resolution vacuum ultraviolet absorption spectra of Kr_2 and Ar_2 obtained by Tanaka and Yoskino[5] not only allowed them to locate many vibrational energy levels of ground states but also enabled them to identify many excited electronic states of Ar_2 and Kr_2. However, to the authors' knowledge, careful ionization studies of the rare gas van der Waals molecules either by electron or photon impact, have not been carried out.

The lower bound of the dissociation energies of the rare gas molecular ions (R_2^+) have been estimated from the appearance potentials of the electron impact induced associative ionization process.[6-10] The first photoionization study of the formation of the Ar_2^+, Kr_2^+ and Xe_2^+ rare gas molecular ions was carried out by Huffman and Katayama.[11] The ions were produced mainly by an associative collision process between an electronically excited atom and a ground state atom, which results in

the formation of a diatomic ion and an electron. Samson and Cairns[12] also have obtained the ionization potentials of Kr_2 and Xe_2 from their photoionization experiment with a high pressure gas cell. Due to the interference stemming from secondary processes they were unable to identify and examine the photoionization of the rare gas van der Waals molecules alone. In order to investigate the photoionization mechanism of van der Waals dimers, we have prepared these molecules by the supersonic expansion of the corresponding monomer at high pressure through a small orifice. By combining the molecular beam technique with photoionization mass spectrometry, we carried out the first photoionization study of Xe_2[13] and demonstrated that the direct ionization mechanism of Xe_2 in the beam is quite different from associative ionization process observed by Hoffman and Katayama in the gas cell. Nevertheless, since the van der Waals well depth decreases from 24 meV in Xe_2[3] to 17 meV for Kr_2[3] and 12 meV for Ar_2[4] it would not be unreasonable to expect a corresponding gradual change in the photoionization mechanism. In this report, we present the first photoionization study of the Kr_2 and Ar_2 van der Waals molecules.

EXPERIMENTAL

The experimental apparatus, arrangement, and procedure are the same as previously described.[13,14] The grating used was coated with MgF_2 and had 1200 lines/mm. The reciprocal dispersion is 8.3Å/mm. With a 100μ entrance and a 300μ exit slit, the resolution achieved is about

1.2Å FWHM. The light source was the helium Hopfield continuum.[15] During this experiment, the discharge lamp was operated by a high power pulser at a repetition rate of 100 KHz and a pulse width of ~0.5μ sec. The photon output at the exit slit of the monochromator was about 10^{10} photon/sec Å at 800Å as measured by a nickel photoelectric cell. At the ionization threshold region of Kr_2, which is around 960Å, the hydrogen many-line pseudocontinuum was used as the light source. This avoided the interference of the high energy photons of the helium Hopfield continuum coming from the second-order diffraction of the grating.

The Kr_2 and Ar_2 van der Waals molecules were prepared by supersonic expansion through a nozzle with 0.127 mm diameter at a stagnation pressure of 500 torr. The mixed beam of atoms and dimers formed by adiabatic cooling then intersected the dispersed vacuum ultraviolet photons at a distance of approximately 7.5 cm from the nozzle. With two stages of differential pumping, the main chamber pressure was maintained at 5×10^{-7} torr during the experiment. The total number density of the beam at the collision center which contained a small fraction of dimers was estimated with an electron bombardment type ionizer to be about 10^{12} atom/cc. The photon detector was a sodium salicylate coated photomultiplier. Data were taken at a wavelength interval of 1Å. In view of the strong pressure dependence of the concentration of the dimers relative to the monomers in the expansion, the nozzle stagnation pressure was well regulated. The photoionization efficiency of $Kr_2(Ar_2)$ at 870Å (780Å) was arbitrarily chosen as a

reference point with which to monitor the fluctuation of the intensity of both the Kr_2 and Ar_2 molecules and the vacuum UV photons. For every 20Å, the monochromator was scanned back to the reference point and the photoionization efficiency was recorded. It was found that the intensity of the Kr_2 (or Ar_2) dimer stayed constant within 3%. The photoion yield curves thus obtained have been normalized to account for the beam fluctuations. The average counting rates at the maximum of the autoionization peaks were about 25 ct/sec for Kr_2 and 15 ct/sec for Ar_2. Generally, counts were collected for 200 sec for Ar_2 and 100 sec for Kr_2. However, near the ionization threshold where the photoionization cross sections were low, counts were accumulated for as long as 800 sec.

RESULTS AND DISCUSSION

Assuming the photoionization cross section of the dimer to be twice that of the atom, the variation of the concentration of the Kr_2 (Ar_2) dimers relative to that of Kr (Ar) atom monitored at 870Å (780Å) were plotted against the nozzle stagnation pressure as shown in Fig. 1. In a static reservoir of a particular gas, the concentration of the dimers relative to the monomers as predicted by the statistical model[2b] is linearly proportional to the pressure (P_o). However, with the expansion arrangement and condition of this work, it was found that the percentage concentration of Kr_2 relative to Kr atoms, $\alpha(Kr_2)$, is approximately proportional to P_o^3, whereas $\alpha(Ar_2)$ is only proportional to $P_o^{1.5}$. It is interesting to note that, by assuming a Lennard-Jones

(6-12) potential, Sogryn and Hirschfelder[16] have calculated the Ar_2 dimer concentration at S.T.P. to be 1×10^{-3}. A value of 3×10^{-3} was obtained from our experiment when Ar is expanded from 1 atmosphere pressure.

The photoionization efficiency curves of Kr_2 and Ar_2, together with that[13] of Xe_2 are shown in Fig. 2. The photoionization thresholds of Xe, Kr, and Ar are also plotted for comparison. The graphs are plotted in energy scale (cm^{-1}) and are shifted such that the ionization potentials of the atoms fall in a line. The Franck-Condon factor for direct ionization is expected to be small for this system. The thresholds are not abrupt, and the curves rise very slowly until the strong autoionization structure sets in. Within the sensitivity of our photoionization mass spectrometer system, which can detect a signal as low as 0.1 count/sec (with 800 sec counting time), the ionization potential for Kr_2 is found to be 963.7 ± 1.2Å (12.86 ± 0.015 eV) and that for Ar_2 is 852.7 ± 1.2Å (14.44 ± 0.02 eV). Using the known dissociation energies of the ground state Kr_2 and Ar_2 van der Waals dimers,[3,4] the dissociation energies, D_0, of Kr_2^+ and Ar_2^+ are deduced to be 1.12 ± 0.02 eV and 1.31 ± 0.02 eV respectively. The values of $D_0(Xe_2^+)$, $D_0(Kr_2^+)$ and $D_0(Ar_2^+)$ derived from other methods are also listed in Table I for comparison with the results of this work. The values for $D_0(Xe_2^+)$ and $D_0(Kr_2^+)$ obtained by Samson and Cairns are in good agreement with our determinations. For $D_0(Ar_2^+)$, a value as high as 2 eV deduced from the high pressure mass spectrometric work of Kebarle, et. al.[18] but this result appears to be too high. Recently, elastic differential scattering measurements have

been performed on $Ar^+ + Ar$ and $Xe^+ + Xe$ at low energy ($E_{c.m.}$ = 5-25 eV) by Lorentz and co-workers.[17] Their data are found to be consistent with a potential well depth of 1.25 eV for Ar_2^+ and 0.97 eV for Xe_2^+. In the vacuum ultraviolet absorption spectrum of Ar_2, a diffuse band which might correspond to the formation of Ar_2^+ was observed starting at 870Å. Consequently, an extremely careful scan in the wavelength region from 870 to 845Å was conducted before I.P. (Ar_2) of 852.7 ± 1.2Å was obtained.

One of the main purposes of this study was to investigate the photoionization mechanism for this class of van der Waals complex. By examining the photoion yield curves of the rare gas dimers (Xe_2, Kr_2 and Ar_2), we can conclude that autoionization is the predominant process. Autoionization essentially consists of two discrete steps. The first one is the excitation of the dimer R_2 to a resonant molecular state, and the second is the interaction between the excited Rydberg electron and the ion core which results in the ejection of the electron and formation of R_2^+ in a discrete ionic level. The resonant molecular levels of R_2 in this energy region can only be derived from the combination of one normal ground state ($^1S_0$) and one excited atomic level. For the electronic states of the rare gas dimer R_2, Hund-Mulliken's case (c) applies. The ground state of R_2 has a closed electronic shell, and thus is a 0_g^+ state. By the selection rules of case (c), transitions from 0_g^+ to 0_u^+ or 1_u excited molecular states are the only ones which are dipole allowed.

All the excited atomic states (except those with J=0) can couple with the ground state rare gas atom ($np^6\ ^1S_0$) (where n=5 for Xe, n=4

for Kr and n=3 for Ar) to give an 0_u^+ and/or an 1_u molecular state. In other words, disregarding the second step in the autoionization process, all the excited atomic levels which have an energy higher than the dissociation energy of the ground state R_2^+ are available for autoionization. However, if we compare the positions of the peaks and the excited atomic levels, we find a very good correlation between the Rydberg atomic level dervied from $4p^5(^2P_{1/2,\ 3/2})$ ns (or nd) ($3p^5(^2P_{1/2,\ 3/2})$ ns (or nd)) for Kr (Ar) and the autoionization peaks as shown in Fig. 2(b) and 2(c). The Rydberg atomic levels derived from $5p^5(^2P_{1/2,\ 3/2})$ ns (and nd) are also plotted in Fig. 2(a) for comparison. The correlation is not very obvious in the case of Xe_2.

The dissociation energies of Kr_2 (17 meV) and Ar_2 (12 meV) are smaller than that of Xe_2 (24 meV). Hence for Kr_2 and Ar_2, one atom feels a small perturbation from its partner. When a photon comes in, it essentially sees two separate atoms. The excitation of one of them will follow the parity selection rule $\Delta l = \pm 1$, which is a well defined property of a free atom with any number of electrons and with any kind of coupling. In other words, the molecular Rydbery orbital is essentially a tightly bound atomic orbital associated entirely with the excited atom. With the atoms of the dimer in the ground state ($^1S_0$), the selection rule $\Delta J = +1$, which is valid for free rare gas atoms, no longer holds. All the atomic levels with different J values (except J=0) which are derived from $5p^5(^2P_{1/2,\ 3/2})$ ns (and nd) for Xe, $4p^5(^2P_{1/2,\ 3/2})$ ns (and nd) for Kr, and $3p^5(^2P_{1/2,\ 3/2})$ ns (and nd) for Ar by jl coupling scheme[19] are expected to be allowed tran-

sitions as a result of the perturbation by its partner. Nevertheless, the dimer is just like a persistent collision complex, and the probability of vibrationally induced autoionization will be large. In fact, the autoionization lifetime will be much shorter than the radiative lifetime. This seems to explain well the observed autoionization structure for Kr_2 and Ar_2 shown in Fig. 2(b) and 2(c). However, this by no means excludes the autoionization of the Rydberg states which are derived from an excited Kr (Ar) atom with the configuration $4p^5(^2P_{1/2,\ 3/2})$ np (or nf) $3p^5(^2P_{1/2,\ 3/2})$ np (or nf)) and a normal ground state Kr (Ar) atom. In fact, it is possibly the autoionization of these levels that gives rise to a finite photoionization efficiency at the onset of the rare gas dimers.

ACKNOWLEDGEMENT

This work was done with support from the U. S. Energy Research and Development Administration.

REFERENCES

1a. F. T. Greene and T. A. Milne, J. Chem. Phys., 39, 3150 (1963).

b. T. A. Milne and F. T. Greene, J. Chem. Phys., 47, 4095 (1967).

2a. R. E. Leckenby, E. J. Robbins and P. A. Trevalion, Proc. Roy. Soc. A, 280, 409 (1964).

b. R. E. Leckenby and E. J. Robbins, Proc. Roy. Soc. London, Ser. A, 291, 389 (1966).

3. J. M. Parson, P. E. Siska and Y. T. Lee, J. Chem. Phys., 56, 1511 (1972).

4. J. A. Baker, R. O. Watts, J. K. Lee, T. P. Schafer and Y. T. Lee, J. Chem. Phys., 61, 308 (1974).

5a. Y. Tanaka, K. Yoshino and D. E. Freeman, J. Chem. Phys., 59, 5160 (1973).

b. Y. Tanaka and K. Yoshino, J. Chem. Phys., 53, 2012 (1970).

6. J. A. Hornbeck and J. P. Molnar, Phys. Rev., 84, 621 (1951).

7. W. Kaul and R. Fuchs, Z. Naturforch, 152, 326 (1960).

8. W. Kaul and R. Taubert, Z. Naturforch, 17a, 88 (1962).

9. M. S. Munson, J. L. Franklin and F. H. Field, J. Phys. Chem., 67, 1542 (1963).

10. C. E. Melton and W. H. Hamill, J. Chem. Phys., 41, 1469 (1964).

11. R. E. Huffman and D. H. Katayama, J. Chem. Phys., 45, 138 (1966).

12. J. A. R. Samson and R. B. Cairns, J. Opt. Soc. Am., 56, 1140 (1966).

13. C. Y. Ng, D. J. Trevor, B. H. Mahan and Y. T. Lee, J. Chem. Phys., to be published.

14. C. Y. Ng, B. H. Mahan and Y. T. Lee, J. Chem. Phys., to be published.

15a. J. J. Hopfield, Phys. Rev., 35, 1133 (1930).

b. J. J. Hopfield, Phys. Rev., 36, 784 (1930).

c. J. J. Hopfield, Astrophys. J., 72, 133 (1930).

16. D. E. Stogryn and J. O. Hirschfelder, J. Chem. Phys., 31, 1531 (1959).

17. D. C. Lorentz, R. E. Olson and G. M. Conklin, Chem. Phys. Lett., 20, 589 (1973).

18. P. Kebarle, R. M. Haynes and S. K. Searles, J. Chem. Phys., 47, 1684 (1967).

19. C. E. Moore, Atomic Energy Levels, NBS Cir. 467, Vol I (1949), II (1952), III (1958).

FIGURE CAPTIONS

Fig. 1. Variation of the Kr_2 and Ar_2 rare gas dimers relative to the corresponding monomer versus nozzle stagnation pressure.

● experimental points for Kr_2 obtained at 870Å

– – – approximate fit, % concentration $\alpha(Kr_2) = 1.81 \times 10^{-3} [P_o \cdot D_o]^3$

○ experimental points for Ar_2 obtained at 780Å

——— approximate fit. $\alpha(Ar_2) = 1.01 \times 10^{-2} (P_o \cdot D_o)^{1.5}$

where P_o (torr) is the nozzle stagnation pressure and D_o (= 0.0127 cm), the nozzle diameter.

Fig. 2. (a) Photoionization efficiency curve of Xe_2 in the energy range from 89,000 cm^{-1} to 103,000 cm^{-1}.

(b) Photoionization efficiency curve of Kr_2 in the energy range from 103,000 cm^{-1} to 118,000 cm^{-1}.

(c) Photoionization efficiency curve of Ar_2 in the energy range from 117,000 cm^{-1} to 132,000 cm^{-1}.

Table I. Rare-gas Ion Dissociation Energies D_o

	Electron Impact Appearance Potentials					Theoretical		Miscellaneous			Photoionization		
	(a)	(b)	(c)	(d)	(e)	(f)	(g)	(h)	(i)	(j)	(k)	(l)	(m)
Ar_2^+	1.08 ±0.1	0.66	0.66	0.84 ±0.02	0.66	1.25	1.21	2	0.0035	1.25	1.049 ±0.009		1.31 ±0.02
Kr_2^+	1.00 ±0.1	0.8		0.8 ±0.02			0.92				0.995 ±0.007	1.13	1.12 ±0.016
Xe_2^+	0.91 ±0.01				0.5		0.65			0.97	0.968 ±0.005	0.99 ±0.02	1.03 ±0.01

(a) Reference 7
(b) Reference 4
(c) Reference 5
(d) Reference 8
(e) Reference 6
(f) T. L. Gilbert and A. C. Wahl (unpublished SCF calculation)
(g) R. S. Mulliken, 52, 5170 (1970)
(h) Reference 18
(i) E. A. Mason and J. T. Vanderslice, J. Chem. Phys., 36, 1103 (1962).
(j) Reference 17
(k) Reference 9
(l) Reference 10
(m) This work.

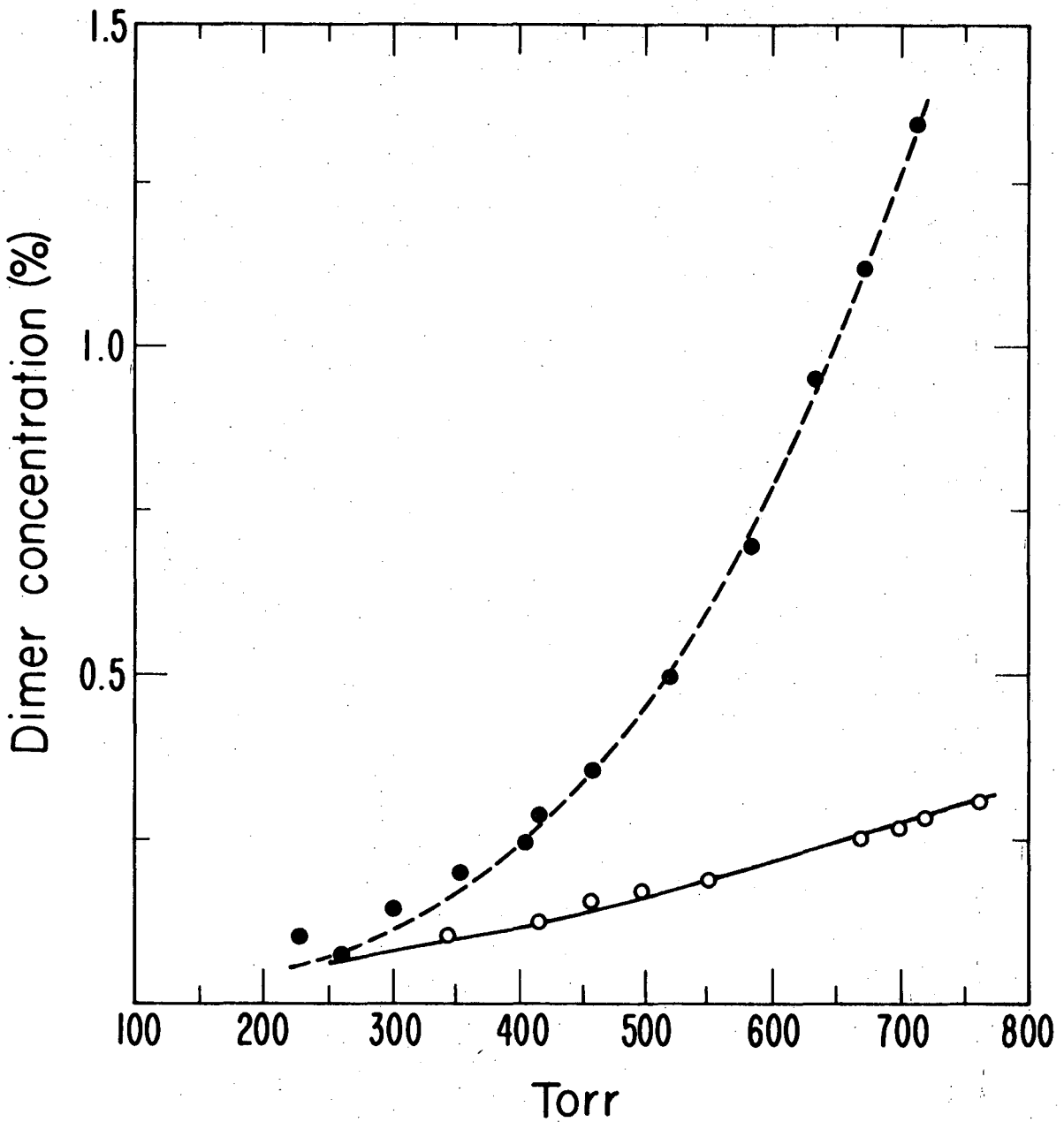

Fig. 1

XBL 767-3200

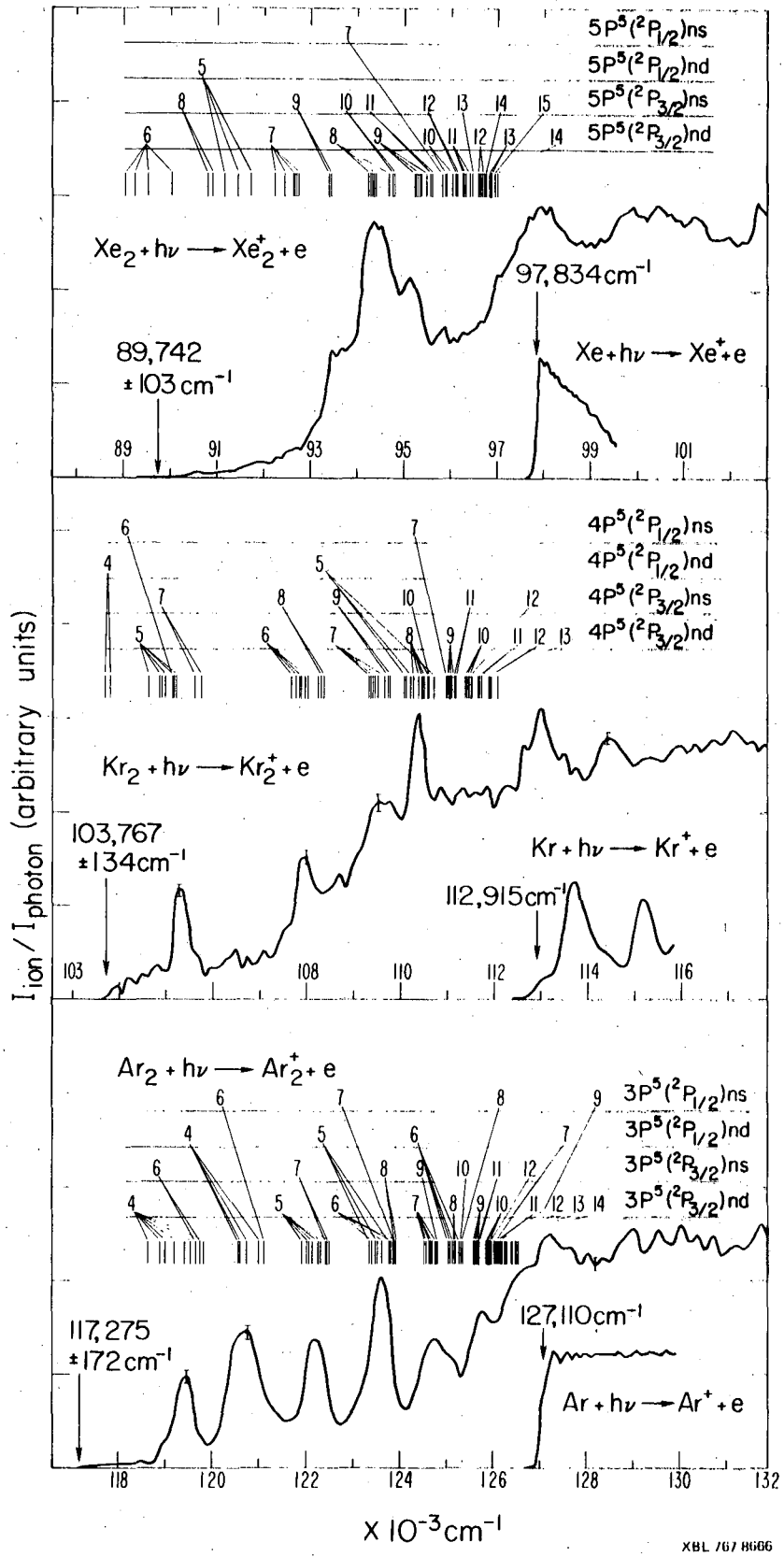

Fig. 2

VI. PHOTOIONIZATION STUDY OF ICl AND THE ArICl VAN DER WAALS MOLECULE

ABSTRACT

Photoionization efficiency curves of ICl and the ArICl van der Waals dimer were obtained with the molecular beam technique in the wavelength range from 1140Å to 1245Å (9.958 eV - 10.875 eV) and from 1190Å to 1250Å (9.919 eV - 10.418 eV) respectively. The ionization potential of ICl from the ground electronic state ($^1\Sigma^+$, v"=0) to the ICl^+ ground molecular ionic state ($^2\Pi_{3/2g}$, v'=0), was found to be 10.069 ± 0.003 eV which is in agreement with the value obtained by Dibeler et. al. The ionization potential corresponding to the ionization of ICl($^1\Sigma^+$, v"=0) to ICl^+($^2\Pi_{1/2g}$, v'=0) was found to be 10.699 ± 0.003 eV. By analyzing the photoion yield curve of ICl, the vibrational quantum for the ICl^+($^2\Pi_{3/2g}$) was deduced to be 428 ± 20 cm^{-1}. The excitation efficiency leading to ion-pair formation (i.e. $ICl + h\nu \rightarrow I^+ + Cl^-$) was also observed for ICl by monitoring the I^+ atomic ion. Using the known electron affinity for Cl($^2P_{3/2}$) atom, the dissociation energy for ICl is deduced to be 2.140 ± 0.003 eV. For ArICl, the ionization potential was observed to be 9.960 ± 0.003 eV which is 0.109 ± 0.003 eV lower than the I.P. of ICl. The photoionization mechanism of the ArICl van der Waals molecule is discussed.

INTRODUCTION

In the studies of the ionization processes of atoms and molecules, the photoionization technique offers many advantages over the electron impact method. First, all the difficulties that contribute to the instability and poor resolution of the electron impact experiments such as sample pyrolysis due to hot filament, the presence of space charge due to the electron beam and the effects of charging up the surfaces of the ion optics, are avoided in the photoionization method. Second, the threshold law for photoionization is much more favorable for investigating the ionization potentials of atoms and molecules. The typical instrumental resolution for photoionization is 1 - 10 meV. However, due to the rotational (and vibrational) temperature of the molecules which is about 30 meV at room temperature, this value of the resolution essentially is unattainable unless the sample gas is cooled down to the corresponding temperature. The cooling of the gas in a gas cell to e.g. 77°K (~7 meV) in a conventional photoionization experiment can only be feasible for noncondensible gases such as H_2. For condensible gases, one of the methods of overcoming this problem is to use the supersonic beam technique to introduce the target gases to the ionization region. In an isentropic expansion, individual molecules can be easily supercooled to well below 20°K. This has been demonstrated by the high resolution obtained for the photoionization efficiency (P.E.) curves of NO,[1] C_2H_2 and CH_3I[2] in photoionization studies which combined molecular beam techniques and photoionization mass spectrometry. As a result of adiabatic cooling, a small percentage

of dimer and polymer will be formed during the expansion. This provides a unique way of synthesizing van der Waals molecules for photoionization studies. Recently, the photoion-yield curves of diatomic halogen and interhalogen molecules have been obtained by Dibeler et. al.[3] Recognizing the thermal population of the excited vibrational states at room temperature, they have applied room temperature and cooled-gas photoionization to distinguish the hot band effect (i.e., the apparent lowing of a threshold value due to the ionization of vibrationally-excited molecules to form ground-state ions) and have identified the adiabatic ionization thresholds for the diatomic homonuclear halogen molecules and for the interhalogens. Iodine monochloride was chosen for this photoionization experiment as an example to investigate the influence of adiabatic cooling on the hot band effect. The photoionization study of the ArICl van der Waals molecule also permits us to examine the photoionization mechanism of this class of weak complexes.

EXPERIMENTAL

The experimental apparatus, arrangement, and procedure is the same as previously described.[1] Iodine monochloride (ICl) was the practical grade obtained from Matheson, Coleman and Bell and was used without further purification. At room temperature, ICl has a vapor pressure of approximately 30 torr. In this experiment ICl vapor was premixed with Ar and then the mixture was introduced into the main chamber as the target gases by expansion through a 0.12 mm diameter pyrex nozzle

at a total stagnation pressure of 450 torr. The light source was the hydrogen many-line pseudocontinuum. The grating used was coated with MgF_2 and had 1200 lines/mm. The reciprocal dispersion was 8.3Å/mm. Using the 100μ entrance and exit slit, the resolution achieved was 0.83Å (~6.5 meV) at 1240Å. Data were collected at a wavelength interval of 0.5Å. The dispersed light coming out from the exit slit was monitored by a sodium salicylate coated photomultiplier. Wavelength calibration was accomplished by using the known emission lines of the hydrogen atom and molecule. The photon signal has been corrected for the background of the stray photons from the monochromator. With two stages of differential pumping, the main chamber pressure was always below 5×10^{-7} torr during the experiment. The counting rates varied from 100 ct/sec to 900 ct/sec for ICl^+. For I^+, the average counting rate at the major autoionization peaks was about 150 ct/sec. Counts were accumulated for 100 sec and 150 sec for ICl^+ and I^+ respectively. The intensity of ArICl relative to that of ICl as probed at 1215.7Å (Lyman α) was about 1.8%. Thus, in the photoionization experiment of ArICl, each point was counted for 350 sec.

RESULTS AND DISCUSSION

A. Iodine-Monochloride (ICl)

The photoionization efficiency curve obtained is shown in Fig. 1. The structure of the P.E. curve is similar to that obtained by Dibeler

et. al.[3a] The ground electronic state of ICl is a $^1\Sigma^+$ state. The first ionization process involves removing an electron from an antibonding π^* orbital and leaving the ICl^+ molecular ion in the ground $^2\Pi_{3/2g}$ state. The sharp onset at 10.069 ± 0.003 eV as observed from the P.E. curve corresponds to the adiabatic ionization potential of ICl from the ground state ($^1\Sigma^+$, v"=0) to the ground ionic state ($^2\Pi_{3/2g}$, v'=0). The I.P. which corresponds to the excited molecular ionic state $^2\Pi_{1/2g}$ was found to be 10.699 ± 0.003 eV.

The small hump before the onset in the P.E. curve is attributed to the hot band effect. The vibrational quantum of $ICl(^1\Sigma^+)$ is 384 cm^{-1}. At room temperature, the ratio of the number of molecules in the first to the ground vibrational state assuming the Boltzman distribution is about 0.15. The peak intensity of the hump relative to that of onset peak is slightly less than 10%. Thus, we conclude that with the present beam production arrangement, the vibrationally excited states of ICl do not relax efficiently. However, as judged from the onset of the ionization threshold, the relaxation of rotational energy is realized.

The P.E. curve of ICl exhibits quite regular autoionization structure which possibly consists of electronic and vibrational autoionization series. Although autoionization is the predominant ionization process for ICl, if the Franck-Condon factors between the ground state $ICl(^1\Sigma^+$, v"=0) and the $ICl^+(^2\Pi_{3/2g}$, v') molecular ionic states are favorable, direct ionization still would take place. By examining the (HeI) photoelectron spectrum of ICl, Cornford has been able to resolve about five vibrational states. In other words, the leading

edges of the first five broad peaks in the P.E. curve of ICl are contributed by direct ionization. The results of the analysis of the energy separation between adjacent (leading edge) autoionization peaks is shown in Table I. The leading edges as assigned as the onsets of the corresponding vibrational states are positioned by solid lines in Fig. 1. The average of the vibrational quantum is 428 ± 25 cm^{-1} which is in good agreement with that obtained by photoelectron spectroscopy.[4]

The autoionization peaks (the second, the fifth, the seventh, and the ninth) have higher photoion yield than the rest, and it is therefore not unreasonable to assume that these peaks have more than one autoionization peak superimposed on each other. The trend of these peaks suggests that they belong to a electronic Rydberg series. Using the ionization potential of ICl from the ground $^1\Sigma^+$, v"=0 state to the $ICl^+(^2\Pi_{1/2g}$, v'=0) molecular ionic state as converging limit, several peaks were identified as members of a Rydberg series described by the Rydberg equation

$$h\nu(eV) = 10.699 - \frac{13.607_4}{(n-0.1)^2} \qquad n = 5,6,7,8,9,10$$

The Rydberg series observed for ICl is very similar in structure to that observed[2] for CH_3I. They may both result from the excitation of a nearly nonbonding electron which is localized mainly around the iodine atom.

The efficiency of the ion-pair formation process, as monitored by I^+ atomic ion, from the onset to 1210Å is shown in Fig. 2. The excitation efficiency curve comprises mainly two broad peaks which

are modulated by sharp autoionization structure. Similar structure has been obtained for Br_2. The threshold of the ion-pair formation process was found to be 1380.3Å (8.982 ± 0.003 eV) which corresponds to the excitation process

$$ICl(^1\Sigma^+, v''=0) + h\nu \longrightarrow I^+(^2P_2) + Cl^-(^1S_0)$$

If the bond dissociation energy for ICl and the ionization potential of the iodine atom is precisely known, we can determine the electron affinity for the Cl atom more accurately. On the other hand, using the ionization potential of the iodine atom (10.457 eV)[5] and the known electron affinity for chlorine atom,[6] $E(Cl(^2P_{3/2})) = 3.613 \pm 0.003$ eV, we obtain from the relation

$$8.982 \text{ eV} = I.P.(I) - E(Cl) + D_0(I\text{-}Cl)$$

the bond dissocation energy for ICl, $D_0(I\text{-}Cl)$, of 2.140 eV ± 0.003 eV. This is slightly less than the spectroscopic value.[7]

B. The ArICl van der Waals molecule.

The photoionization efficiency curve for the ArICl van der Waals molecule is shown in Fig. 3. The ionization potential of ArICl was found to be 9.960 ± 0.003 eV, which is 0.109 eV lower than the I.P. of ICl. The ArICl van der Waals molecules which is synthesized by isentropic expansion is likely to have a distribution of internal energy. Thus the resolution obtained for the P.E. curve of ArICl as shown in Fig. 3 is expected to be worse than that of ICl alone. By shifting the P.E. curve of ICl to lower energy and normalizing the I.P. of ICl with that of ArICl, we found that the structures of the two spectra are very similar.

Thus, the photoionization process of ArICl is essentially the same as that of ICl except the I.P. of ArICl is lower than that of ICl. It is interesting to note that, there is a narrow step which is found to be reproducible at the onset in the P.E. curve of ArICl, this may have related to the distribution of the internal energy for ArICl. Assuming ε^+ is the dissociation energy for the Ar-$(ICl)^+$ complex, and ε is that for Ar-ICl, the following relation can be derived:

$$\varepsilon^+ + \text{I.P.(Ar-ICl)} = \varepsilon + \text{I.P.(ICl)}$$

or

$$\varepsilon^+ - \varepsilon = 0.109 \pm 0.003 \text{ eV}$$

The minimum value of ε^+, ε^+_{min}, is thus equal to 0.109 eV. The vibrational quantum of $ICl(^1\Sigma^+)$ as obtained from our experiment is ΔE_v = 0.053 eV. Due to intramolecular energy transfer, it is expected that Ar-$ICl^+(^2\Pi_{3/2g}$, v') will not be bound, if ICl^+ has vibrational energy bigger than ε^+. According to our estimates, $\varepsilon^+_{min} > 2\Delta E_v$ (where ΔE is the vibrational quantum of $ICl^+(^2\Pi_{3/2g})$). That is Ar-$ICl^+(^2\Pi_{3/2g}$, v'=0) and Ar-$ICl^+(^2\Pi_{3/2g}$, v'=1) must be bound.

REFERENCES

1. C. Y. Ng, B. H. Mahan and Y. T. Lee, J. Chem. Phys., to be published.
2. C. Y. Ng, Ph.D. Thesis, The University of California, Berkeley, 1976.
3a. V. H. Dibeler, J. A. Walker, K. E. McCulloh and H. M. Rosenstock, Int. J. Mass. Spectrom. Ion. Phys., 7, 209 (1971).

b. V. H. Dibeler, J. A. Walker and K. E. McCulloh, J. Chem. Phys., 53, 4414 (1970).

c. V. H. Dibeler, J. A. Walker and K. E. McCulloh, J. Chem. Phys., 53, 4715 (1970).

4. A. B. Cornford, Ph.D. Thesis, The University of British Columbia, 1971.
5. C. E. Moore, Atomic Energy Levels, NBS Circ., 467, Vol. 3 (1958).
6. R. S. Berry and C. W. Reiman, J. Chem. Phys., 38, 1540 (1963).
7. G. Herzberg, "Molecular Spectra and Molecular Structure, I. Spectra of Diatomic Molecules," Van Nostrand Reinhold Company, 2nd Ed., P.542, New York, (1950).

Table I. The vibrational quanta of $ICl^+(^2\Pi_{3/2g})$ (cm^{-1})

$\Delta v'$[a]	0-1	1-2	2-3	3-4	4-5	5-6
$\Delta E_{v'}$[b]	430	435	423	428	432	420

(a) v' is the vibrational quantum number

(b) $\Delta E_{v'}$ = vibrational quantum between adjacent vibrational states (the uncertainty of these values is ± 25 cm^{-1}).

FIGURE CAPTIONS

Fig. 1. Photoionization efficiency curve of ICl in the wavelength range from 1140Å to 1245Å (9.958 eV - 10.875 eV).

Fig. 2. Excitation efficiency curve of the ion-pair formation process for ICl by monitoring the I^+ ion in the wavelength range from 1210Å to 1390Å (8.919 eV - 10.246 eV).

Fig. 3. Photoionization efficiency curve of the ArICl van der Waals molecules in the wavelength range from 1190Å to 1250Å (9.919 eV - 10.418 eV).

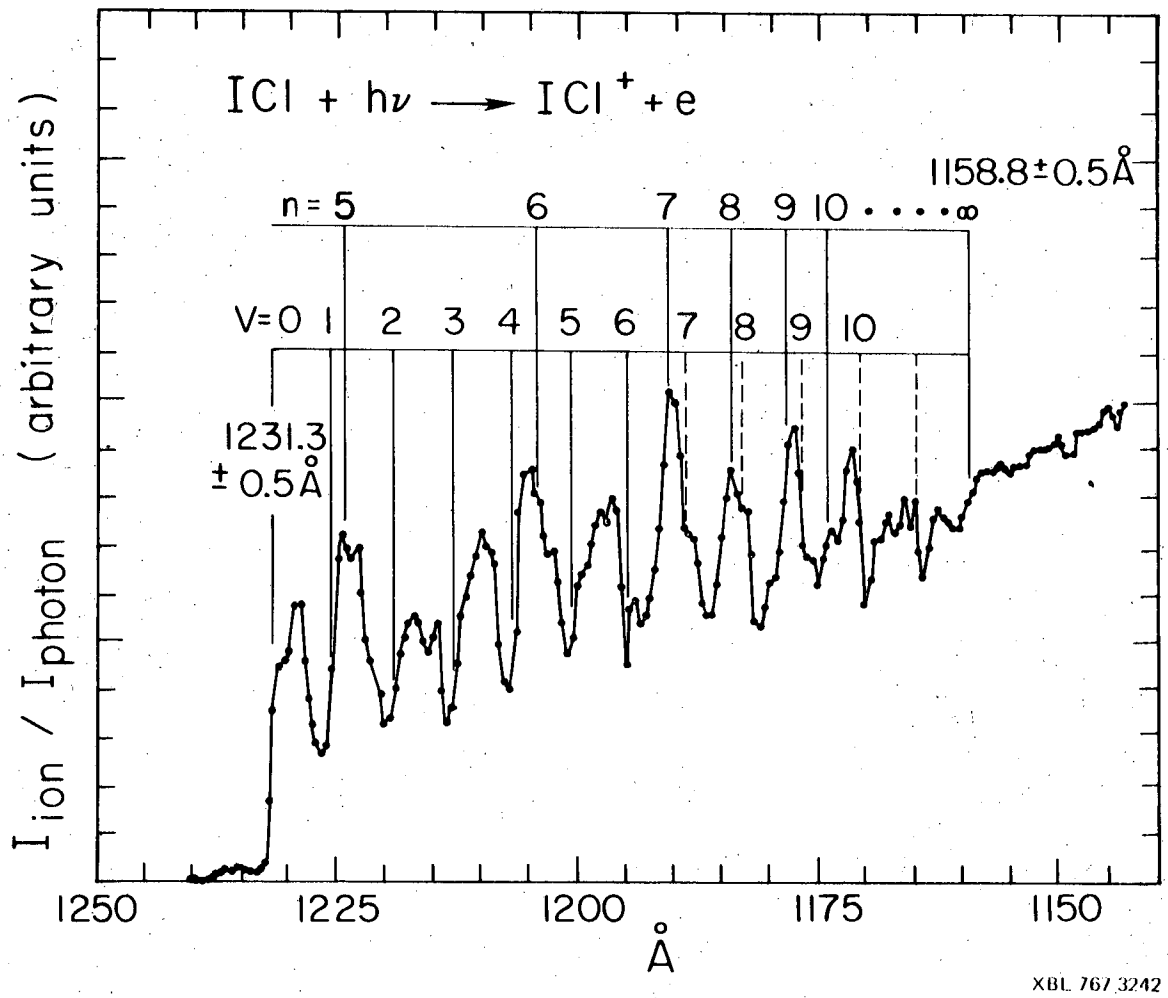

Fig. 1

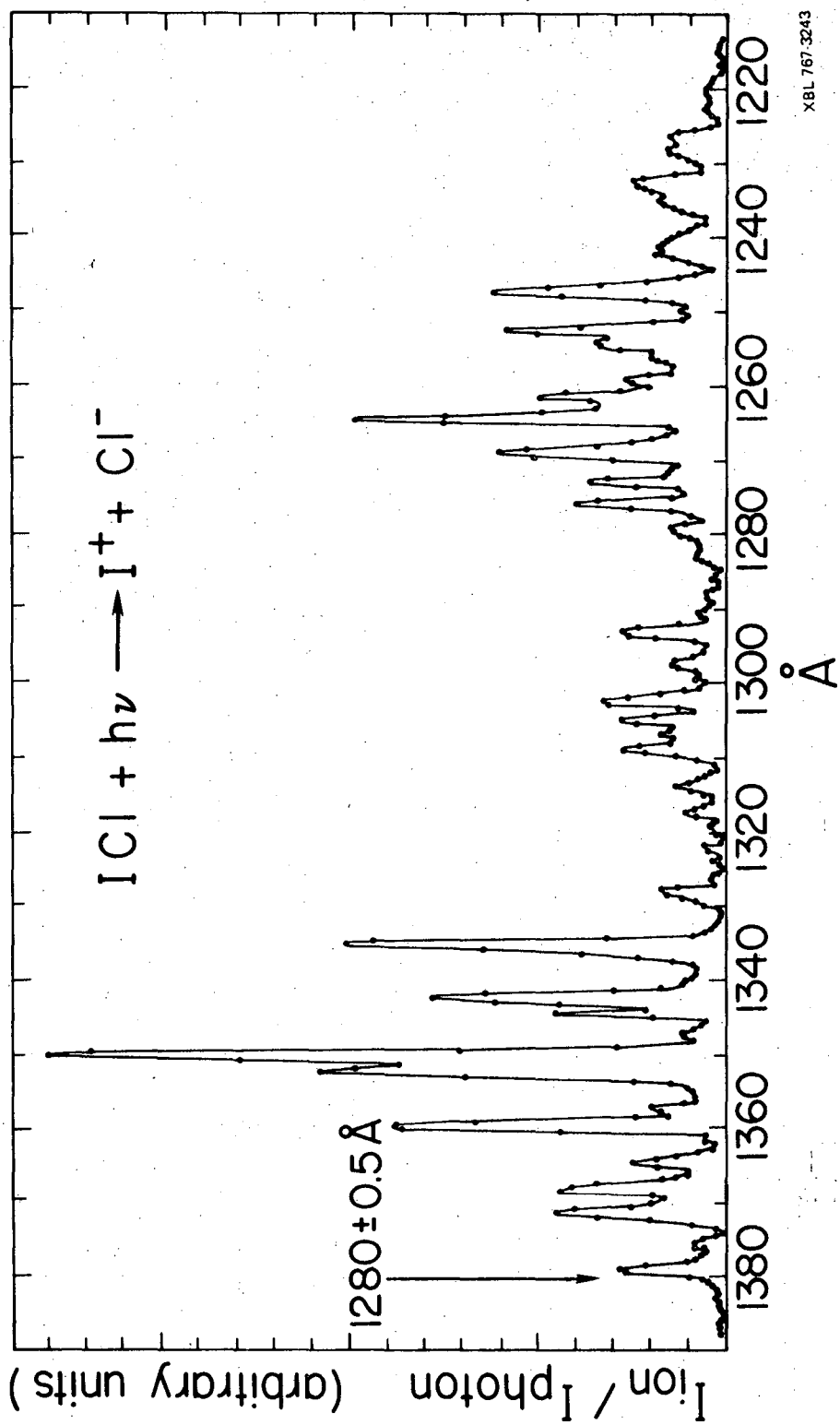
ICl + hν ⟶ I⁺ + Cl⁻
1280±0.5Å
I ion / I photon (arbitrary units)
1380
1360
1340
1320
1300
1280
1260
1240
1220
Å
XBL 767-3243

Fig. 2

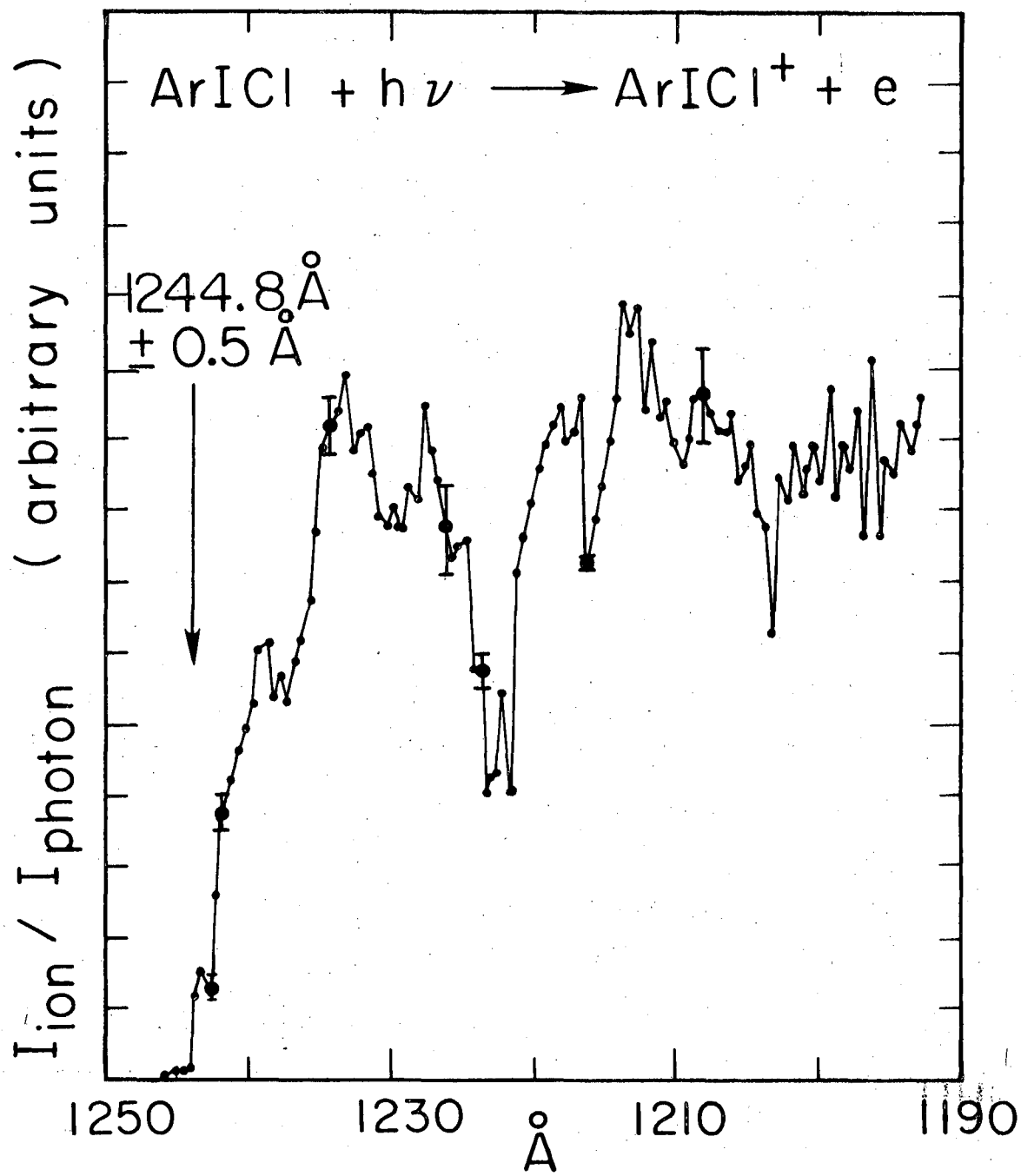

Fig. 3

XBL 767-3241

VII. PHOTOIONIZATION STUDY OF ACETYLENE (C_2H_2) AND METHYL IODIDE (CH_3I)

A. Photoionization Study of Acetylene (C_2H_2)

INTRODUCTION

There is a general agreement on the first ionization threshold value of acetylene as derived by photoionization studies,[1-5] photoelectron spectroscopy,[6] vacuum ultraviolet absorption spectroscopy[7,8] and monoenergetic electron impact.[9] Photoionization studies have also shown that, the ionization of acetylene $C_2H_2(^1\Sigma_g^+)$ to the ground molecular ionic state $C_2H_2^+$ $(^2\Pi_u)$ gives rise to a step-function behavior corresponding to the ground, and first and second vibrationally excited states of the ion. Recently, Dibeler et. al., obtained a high resolution photoionization curve of C_2H_2 and resolved the weak autoionization structure which is superimposed on the steps. Their experiment was done by cooling acetylene in a low pressure gas cell to 118°K, which lowered the rotational envelope to approximately a width of 0.01 eV. In our photoionization study, acetylene was chosen to investigate the rotational relaxation through supersonic gas expansion. With the 100μ entrance and exit slits on a 1 meter monochromator, the instrumental resolution achieved will be about 0.01 eV in the wavelength region which corresponds to the ionization threshold of acetylene. Thus, it is expected that, if the rotation energy of acetylene is relaxed by supersonic expansion, we would obtain a photoionization efficiency curve with at least as good resolution as that employed by Dibeler.

EXPERIMENTAL

The experimental apparatus, arrangement and procedure were the same as previously described.[10] The acetylene gas (99.6% minimum purity) obtained from Matheson without further purification. Acetylene was introduced into the main chamber as a target gas by supersonic expansion through a 0.127 mm diameter nozzle at stagnation pressure of 300 torr. The stability of the stagnation pressure was well regulated by a needle valve (Edwards high vacuum LTD). Data were taken at a wavelength interval of 0.5Å. From the onset to 1040Å, counts were accumulated for 40 sec. In the wavelength region 1040Å to 1020Å, each point was counted for 100 sec. The average counting rate at the threshold was about 60 ct/sec.

RESULTS AND DISCUSSION

The photoionization efficiency (P.E.) curve obtained in the wavelength region from 1020Å to 1095Å (11.322 eV - 12.155 eV) for acetylene is shown in Fig. 1. As expected, the P.E. curve of acetylene compares favorably with that obtained by Dibeler. In other words, the rotational temperature in our experiment is less than 118°K after the expansion with our beam production system.

The ground state electronic configuration of acetylene can be expressed as:[11]

$$C_2H_2 : (\sigma_g|S_c)^2(\sigma_u|S_c)^2(2\sigma_g)^2(2\sigma_u)^2(3\sigma_g)^2(1\Pi_u)^4,\ {}^1\Sigma_g^+$$

The first ion onset, which is observed to be 11.398 ± 0.005 eV, corresponds to the energy required to remove one of the 1π electrons and leave the molecular ion in a $^2\Pi_u$ state. Wilkinson[8] has obtained high resolution absorption spectra for C_2H_2 and C_2D_2 in the vacuum ultraviolet. Several electronic transitions were identified. One of these, designated 3R, is of a Rydberg type and evidently involves a linear upper state. The ν_2 (C-C stretching frequency) vibrational mode of the 3R state was found to be 0.23 eV for C_2H_2. This value compares favorably with the vibrational intervals which have an average value of 0.21 eV resolved from the P.E. curve of C_2H_2. On this basis, early studies suggested that the ionization of C_2H_2 from the ground electronic state ($^1\Sigma^+$, v"=0) to the ground molecular ionic state $^2\Pi_u$ involves the excitation of the ν_2 (C-C stretching) mode for $C_2H_2^+$. The summary of ionization energies for acetylene obtained from this work is listed in Table I.

Beside the simple step structure as observed from the P.E. curve of acetylene, the curve also contains a series of peaks superimposed on the steps. These features correspond to weak autoionization of one or more Rydberg series converging to the several limits of the vibrationally excited states of $C_2H_2^+$. Two Rydberg series in the vacuum ultraviolet absorption spectrum of acetylene were identified by Price.[7]

$$h\nu(eV) = 11.416 - \frac{13.607_4}{(n-0.50)^2} \qquad \text{Series I}$$

$$h\nu(eV) = 11.400 - \frac{13.607_4}{(n-0.95)^2} \qquad \text{Series II}$$

Both series lead to nearly the same ionization energy of 11.41 eV. The small difference in limits possibly representing the splitting of the lowest $^2\Pi$ state of the ion. Using the same δ values, Dibeler et. al. have calculated the Rydberg series converging to each of the three vibrational states of $C_2H_2^+$. It is found that Series II correlates well with observed peaks. These series are also shown in Fig. 1.

REFERENCES

1. V. H. Dibeler and R. M. Reese, J. Res. Nat. Bur. Stand., A68, 409 (1964).
2. A. J. C. Nicholson, J. Chem. Phys., 43, 1171 (1965).
3. R. Botter, V. H. Dibeler, J. A. Walker and H. M. Rosenstock, J. Chem. Phys., 44, 1271 (1966).
4. B. Brehm, Z. Naturforsch., 21a, 196 (1966).
5. I. Omura, T. Kaneko, Y. Yamada and K. Tarraka, J. Phys. Soc. Jap., 27, 178 (1969).
6. C. Baker and D. W. Turner, Pro. Roy. Soc. (London), A308, 19 (1968)
7. W. C. Price, Phys. Rev., 47, 444 (1935).
8. P. G. Wilkinson, J. Mol. Spectrosc., 2, 387 (1958).
9. F. P. Lossing, Int. J. Mass Spectrom. Ion Phys., 5, 190 (1970).
10. C. Y. Ng, B. H. Mahan and Y. T. Lee, J. Chem. Phys., (1976).

Table I. Summary of Ionization Energies for Acetylene

Transition	Ionization Energy (eV)	ΔEv^a (eV)
$^1\Sigma_g^+$, v"=0 → $^2\Pi_u$, v'=0	11.308 ± 0.005	0.220
→ $^2\Pi_u$, v'=1	11.618 ± 0.005	0.218
→ $^2\Pi_u$, v'=2	11.836 ± 0.005	0.210
→ $^2\Pi_u$, v'=3	12.046 ± 0.006	

[a] ΔEv is the vibrational spacing.

FIGURE CAPTIONS

Fig. 1. The photoionization efficiency curve of acetylene (C_2H_2 in the wavelength range from 1020Å to 1095Å (11.322 eV - 12.155 eV).

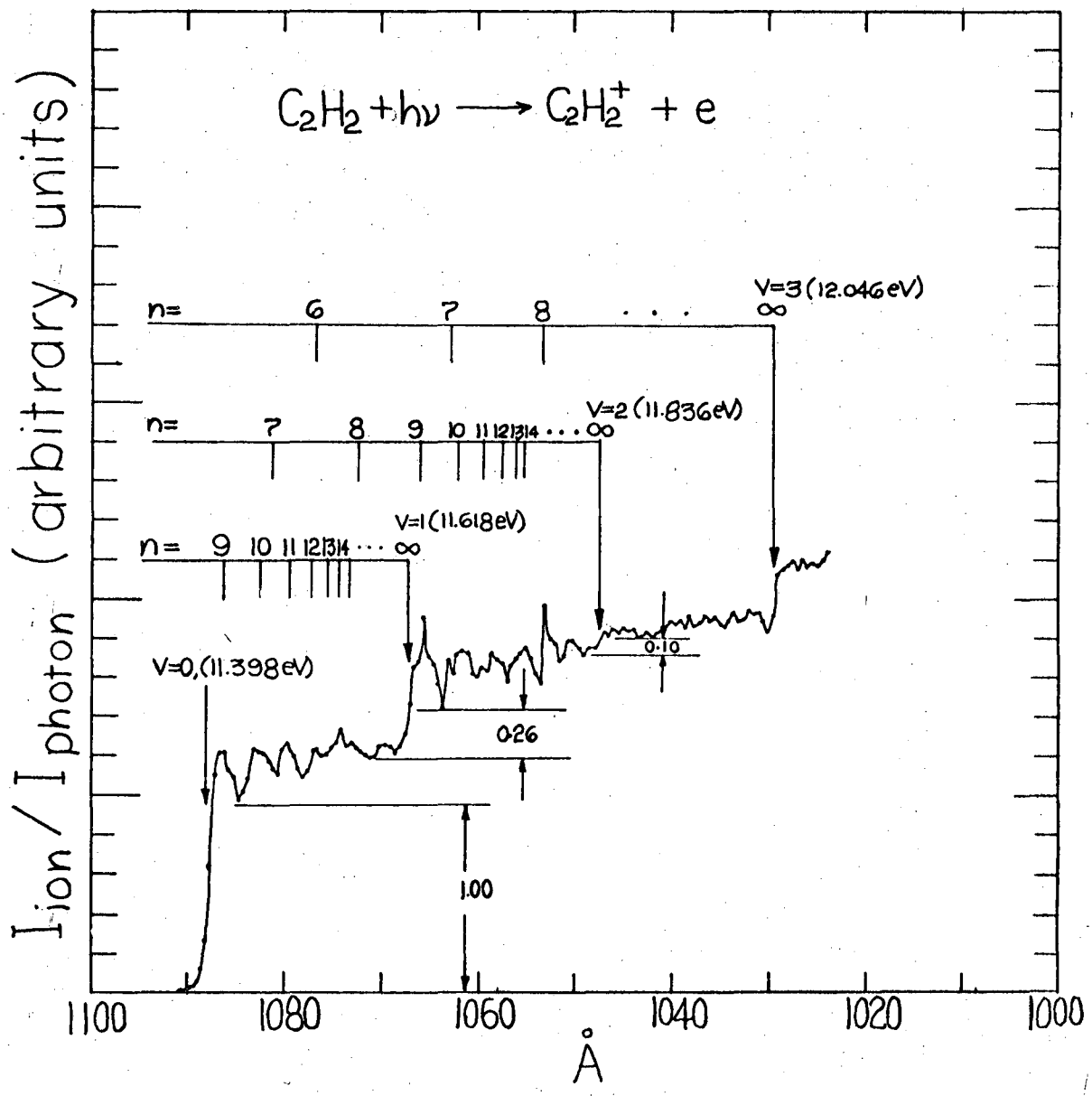

Fig. 1

B. Photoionization Study of Methyl Iodide (CH_3I)

Autoionization is a familiar phenomenon in photoionization, but has been largely avoided in 21.22 eV (HeI) photoelectron spectroscopy. The reason is that for ordinary gases there are relatively few strong autoionizing states at energies above 20 eV. Autoionization was found to be the major ionizing process for CH_3I near the threshold from the previous photoionization studies.[1,2] The lowest ionization potential of methyl iodide corresponds to the removal of an electron from a nonbonding (5p, e) orbital which is mainly localized on the iodine atom. This leaves the CH_3I^+ molecular ion in the ^2E state which is further split by spin-orbit interaction into the $^2E_{3/2}$ (ground) and $^2E_{1/2}$ states.

The experimental apparatus, arrangement and procedure was the same as previously described.[3] Methyl iodide was introduced into the main chamber as a target gas by expansion through a 0.12 mm diameter pyrex nozzle at a stagnation pressure of 400 torr (the vapor pressure of methyl iodide at room temperature). The average counting rate was about 200 ct/sec. Counts were collected for 100 sec at each point.

The photoionization efficiency curve for methyl iodide is shown in Fig. 1. The spectrum shows a large number of well defined autoionization peaks. It is found that this series is the same as obtained by Price[4] from the analysis of the vacuum ultraviolet absorption spectrum of CH_3I. This series is fit by the Rydberg equation

$$h\nu(eV) = 10.157 - \frac{13.607_4}{(n - 0.20)^2} \qquad n = 5\text{-}14$$

The splitting in the two peaks corresponding to n = 5 and 6 is suggested to be caused by the interaction of the Rydberg electron with the non-spherical charge distribution of the CH_3I^+ core.[2]

The first ionization potential as determined from our experiment is 9.532 ± 0.003 eV, which agrees favorably with the spectroscopic value.[4] The spin-orbit splitting of the ^2E molecular ionic state for CH_3I^+ is expected to be mainly determined by the spin-orbit coupling coefficient of an I^+ atomic ion, since it is determined by the group $5p^3$ localized on I^+. The spin-orbit coupling constant determined for CH_3I^+ from this experiment is 0.625 ± 0.003 eV which is nearly the same as the splitting of similar doublet in ICl^{+5} (0.630 eV).

REFERENCES

1. J. P. Morrison, H. Hurzeler and M. G. Inghram, J. Chem. Phys., 33, 821 (1960).
2. T. Baer and B. P. Tsai, J. of Electron Spect. and Related Phenomena, 2, 25 (1973).
3. C. Y. Ng, B. H. Mahan and Y. T. Lee, J. Chem. Phys., (1976).
4. W. C. Price, J. Chem. Phys., 4, 536 (1936).
5. C. Y. Ng, B. H. Mahan and Y. T. Lee, J. Int. Mass Spect. and Ion Phys., to be published.

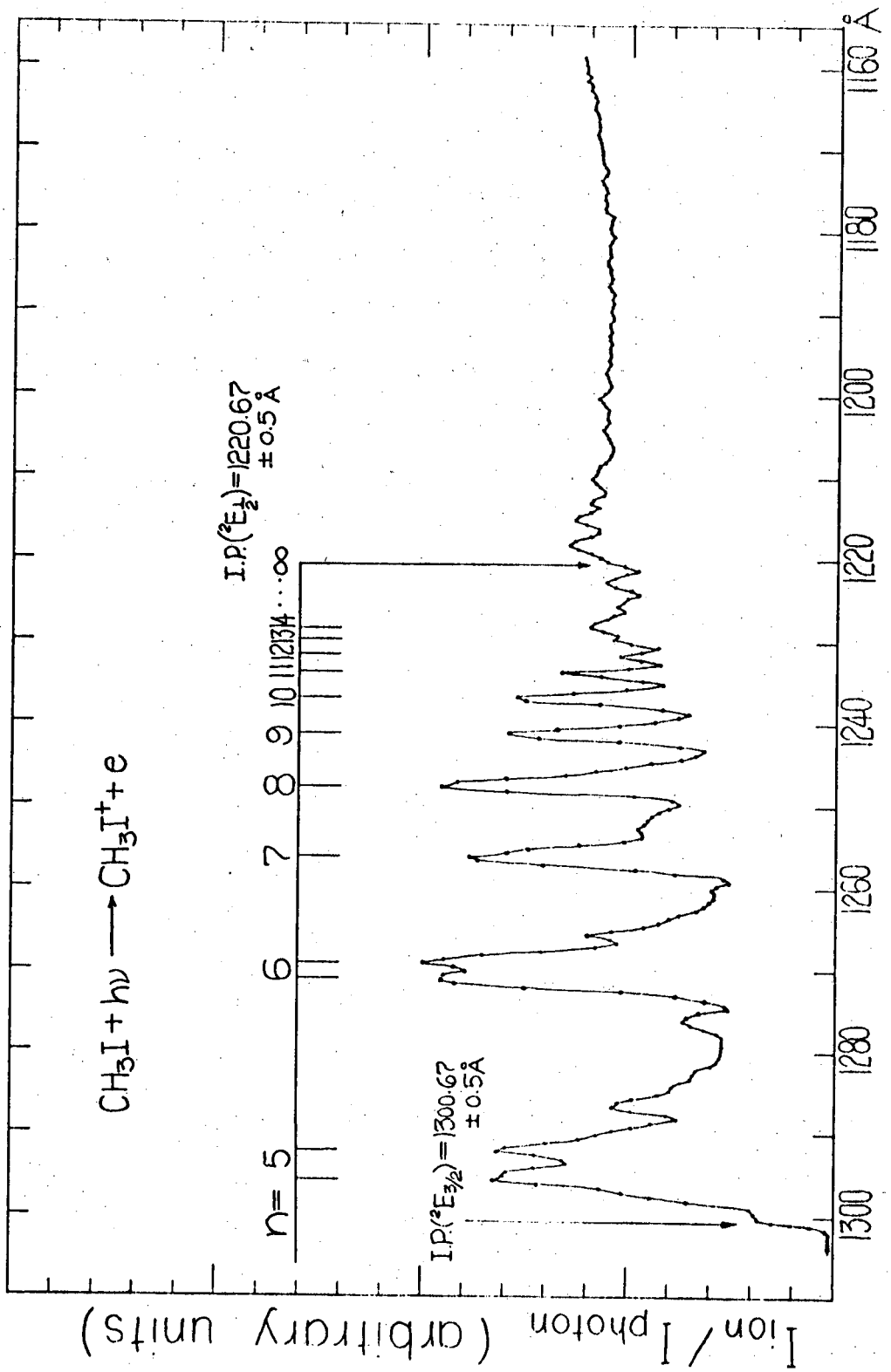
I_{ion} / I_{photon} (arbitrary units)
$CH_3I + h\nu \longrightarrow CH_3I^+ + e$
n= 5 6 7 8 9 10 11 12 13 14 ··· ∞
I.P.($^2E_{3/2}$)=1300.67 ±0.5Å
I.P.($^2E_{1/2}$)=1220.67 ±0.5Å
1300 1280 1260 1240 1220 1200 1180 1160 Å

Fig. 2

VIII. IMPROVED POTENTIALS FOR Ne + Ar, Ne + Kr AND Ne + Xe

ABSTRACT

Improved interatomic potentials for Ne-rare gas pairs have been obtained by fitting a multiparameter potential to low energy differential cross sections, second virial coefficients and diffusion coefficients. All asymmetric Ne-rare gas potentials have narrower attractive wells than those of the symmetric rare gas pairs. The values of r_m and ε for Ne + Ar, Ne + Kr and Ne + Xe are 3.43Å, 719°K; 3.58Å, 74.5°K and 3.75Å, 75.0°K, respectively.

INTRODUCTION

Potential parameters for Ne + Ar, Ne + Kr, and Ne + Xe have been previously determined by fitting LJ (n,6) potentials to the differential elastic scattering cross sections.[1] Parson et. al.[1] have been able to resolve oscillations in their differential cross section measurements and to discriminate against the LJ (8,6) and the LJ (12,6) in favor of the LJ (20,6) potential for these systems. Although the LJ (20,6) potential is not expected to provide an adequate description for the long range attraction and short range repulsion, the LJ (20,6) potentials with suitable values of r_m and ε do provide differential cross sections in good agreement with experimental results for all Ne + Ar, Ne + Kr, and Ne + Xe systems at thermal energies. Thus, it is concluded that the narrower LJ (20,6) potentials should provide a good description of the shape of the attractive well, and the parameters (ε and r_m) obtained must be quite realistic. The striking results that well depths of Ne + Ar, Ne + Kr, and Ne + Xe are almost identical, as observed in that work, were somewhat unexpected. Since the commonly used geometric combining rule for well depths of asymmetric systems from corresponding symmetric pairs predicts a significantly deeper well for Ne + Xe compared to Ne + Ar, some questions have been raised regarding the reliability of these potential parameters and the sensitivity of experimental angular distributions of these systems to the potential parameters.[2] We have made further investigations of these systems by carrying out differential cross section measurments at lower collision energies than in the previous work and have derived more precise

multiparameter piecewise potentials in the form of MSV or ESMSV,[3] which provide good agreement with both experimental differential cross sections, second virial coefficients and diffusion coefficients.

EXPERIMENTAL

The experiments were carried out by crossing two supersonic beams of noble gas atoms, as described previously.[3] The Ne beam was produced from a cryogenic beam source[4] cooled with liquid nitrogen. The source pressure of the primary beam was about 450 torr at 77°K while that of the secondary beam was about 500 torr for Ar and Kr, and 300 torr for Xe at room temperature. The angular distributions were obtained by counting elastically scattered Ne atoms for 40 sec at each angle between 3° and 40°. Each mixed pair was scanned three times, and the angular distributions obtained were averaged and are shown in Fig. 1. In order to correct for drifting and fluctuation of the beams and detector sensitivity, we returned to the reference angle (10° from the Ne beam) frequently during the scan, and data were time normalized. The standard deviations of 40 sec counts at the reference angle were less than 2%. In the Ne + Kr and Ne + Xe experiments, Ne was detected at M/e = 20 (Ne^+), but in Ne + Ar experiments Ne was detected at M/e = 10 (Ne^{++}). It was found that the differential cross section for Ne + Ar, obtained by detecting Ne^+, is significantly different from that obtained by detecting Ne^{++} at wide angles when both Ne and Ar beams are at room temperature. With the liquid nitrogen cooled Ne beam,

however, the differences are only detectable at laboratory angles larger than 25° from the Ne beam. A simple kinematic analysis shows that this is due to be simultaneous detection of elastically scattered Ne as Ne^{+} and Ar as Ar^{++} at M/e = 20. Detection of Ne as Ne^{++} is free from contamination of Ar, since Ar^{+4} is not produced in our detector using a 200 eV electron beam.

RESULTS AND ANALYSIS

The experimental results of Ne + Kr and Ne + Xe were fitted by varying eight parameters (ε, r_m, β, c_6, c_8, x_3, x_4) of the piecewise Morse-Spline-van der Waals potentials (MSV), as mentioned before.[3] For Ne + Ar, since information on the repulsive part of the potential is available, the exponential form is used in the high energy region (1.1 to 10 eV), and connected smoothly by an exponential Spline function to a Morse function. The reduced form of the exponential-Spline-Morse-Spline-van der Waals (ESMSV) potential is written as follows:

$$f(x) = V(r)/\varepsilon \qquad x = r/r_m \qquad C_n = C_n/\varepsilon r_m^n$$

$$f = A\exp[-\alpha(x-1)] \qquad 0 < x \leq x_1$$

$$f = \exp(a_1 + (x-x_1)\{a_2+(x-x_2)[a_3 + (x-x_1)a_4]\})$$

(Exponential Spline function) $\qquad x_1 < x < x_2$

$$f = \exp[-2\beta(x-1)]-2\exp[-\beta(x-1)] \qquad x_2 \leq x \leq x_3$$

$$f = b_1 + (x-x_3)\{b_2 + (x-x_4)[b_3 + (x-x_3)b_4]\}$$

(Cubic Spline function) $\qquad x_3 < x < x_4$

$$f = -c_6 x^{-6} - c_8 x^{-8} - c_{10} x^{-10} \qquad x_4 \leq x < \infty$$

Differential cross sections were calculated using the JWKB method of approximating phase shifts. A nonlinear least squares fitting technique by Marquardt[5] was used to obtain initial estimates of ε, r_m, β for fixed x_3 and x_4. Values of x_3 and x_4 are varied to change the shape of the outer wall of the well. C_6 constants are taken from the semiempirical calculation by Gordon et. al.[6-8] C_8 constants are the geometric means of the symmetric pairs, and C_{10} constants are neglected because of lack of information. Thus, only five parameters are varied to fit the low temperature elastic differential cross sections. The value of r_m can be well determined for a given potential function by matching the fast oscillations resolved in experimental angular distributions and those of theoretical calculations. Since low energy differential cross sections are quite sensitive to the shape of the attractive parts of the potentials, the locations of joining points, x_3 and x_4, must be chosen very carefully in order to give a good fit to the small angle differential cross sections. Finally β and ε are varied to obtain optimum values. This sequence of variation of parameters is repeated until the calculated differential cross sections give excellent agreement with experimental results. In the process of finding the best parameters, second virial coefficients were also calculated and compared with experimental data.[9,10] Although for Ne +

Kr and Ne + Xe only a few second virial coefficient data points are available, these second virial coefficient data measured at relatively high temperatures are sensitive to the repulsive parts of the potentials and supplement low energy differential cross section data which are mainly sensitive to the attractive well. The ESMSV potential for Ne + Ar and MSV potentials for Ne + Kr and Ne + Xe, which give a good agreement with both the differential cross sections and the second virial coefficients are then used to calculate diffusion coefficients at various temperatures. The calculated diffusion coefficients for Ne + Kr and Ne + Xe give excellent agreement with the experimental measurements of Hogervorst,[28] but for Ne + Ar, although the agreement is excellent up to 700°K, the calculated diffusion coefficients are 4.1% higher than the experimental value at 1000°K and the deviation increases to 5.9% at 1400°K. The small but significant discrepancies at very high temperatures indicate that the high energy repulsive part of the potential of Ne + Ar could further be improved, Consequently, three parameters, A, α and x_1, related to the exponential repulsion are adjusted until the calculated diffusion coefficients also agree with the experimental values. The best fit ESMSV potential for Ne + Ar and MSV potentials for Ne + Kr and Ne + Xe are shown in Fig. 2. The parameters of these potentials are listed in Table I. The differential cross sections calculated from the best potentials obtained are also compared with experimental results in Fig. 1. The second virial coefficients were calculated by Hirschfelder, Curtiss, and Bird,[12] including two quantum corrections. For Ne-rare gas

systems, quantum corrections are relatively small compared to classical calculations in the temperature range in which comparisons were made. The standard deviations of the best parametric potentials for Ne + Ar, Ne + Kr, and Ne + Xe fitted to the second virial coefficients are 0.81, 0.439, and 0.648 cc/mole, respectively, and these values are considered to be satisfactory in view of the uncertainty of the second virial coefficient data. The calculated second virial coefficients are compared with the experimental results in Fig. 3 as a function of temperature.

DISCUSSION

The reduced masses of Ne + Ar, Ne + Kr, and Ne + Xe are relatively small, and at a reduced collision energy (E/ε) around five, pronounced rainbow structures are only observed in the Ne + Xe system. In finding a potential from a differential cross section, it is very important to recognize that the relative intensities at all angles, as well as positions of extrema in differential cross sections, must be matched precisely. If the potential functions assumed are not realistic, one often finds that by varying the parameters it is possible to match the locations of extrema but not the relative intensity at all angles. Amplitudes of extrema, such as fast oscillations, rainbow oscillations, and symmetry oscillations, are usually damped by finite velocity spreads in the beam and finite angular resolution of the experimental arrangement. Consequently, in order to make a proper comparison, differential cross

sections calculated from a given potential should be averaged over experimental conditions. Values of ε and r_m determined for Ne + Ar, Ne + Kr, and Ne + Xe in this work, are estimated to be better than 3%. In Fig. 4, sensitivity of differential cross sections for Ne + Ar to the values of ε and r_m are illustrated. Fig. 4a shows a series of calculations changing only r_m by 5% in both directions from the best MSV potential determined. The difference in the frequency and position of fast oscillations is quite noticeable. In Fig. 4b, ε is changed 7% from the best value, and appreciable changes in the slope of differential cross sections are observable. By keeping the product of ε and r_m nearly constant and changing individual parameters 5 to 7% the general fall-off in angular distributions is found to be quite similar, as shown in Fig. 4c. Nevertheless, the difference in oscillation frequency and amplitude can be detected. Calculations shown in Fig. 4 are all averaged over experimental conditions.

It is interesting to note that ε and r_m values determined in this work are within the uncertainty of previous work using a LJ (20,6) potential form. Recently, in order to make a comparison with the experimental results of Parson et. al.,[1] Brown and Munn[2] calculated differential cross sections for the mixed inert gas systems Ne + Ar, Ne + Kr, Ne + Xe, Ar + Kr, and Ar + Xe, using a potential $V(r) = \varepsilon\phi(r/\sigma)$ proposed by Munn[13-15] and a set of combining rules proposed by Kohler[16] for the specific energy and length scaling parameters:

$$\sigma_{ij} = (\sigma_{ii} + \sigma_{jj})/2$$

$$\varepsilon_{ij} = 2\alpha_i \alpha_j / \sigma_{ij}^6 (\gamma_{ii} + \gamma_{jj})$$

where

$$\gamma_{ii} = (\alpha_i^2/\varepsilon_{ii}\,\sigma_{ii}^6),$$

ε and σ are the depth of the potential minimum and position of the potential zero, and α is the polarizability.

They stated that the gross rainbow structure of the scattering cross sections was reproduced by their calculations and that there was substantial agreement with the high frequency oscillations observed in the neon series. They concluded that the lack of good agreement between their mixed interaction potential parameters (derived from virial and transport data and the use of the combination rule) and those derived by Parson et. al. indicates that more theoretical and experimental work is needed to unequivocally determine the mixed and pure rare gas interactions.

Actually, the disagreement between the differential cross sections calculated with their potentials and those measured by Parson et. al. is quite appreciable, and the differences in differential cross sections do reflect the differences in the proposed well depths. In the work of Brown and Munn, the experimental results are compared with a calculation for a single relative velocity. Thus, the differences between the calculation and the data are somewhat obscured by the large amplitude and high frequency oscillations, which are severely damped in the experiment.

The values of ε and σ (defined as $V(\sigma) = 0$) are compared with commonly used combination rules and listed in Table II. The simple combination rules do not give good estimates for these systems. As

in He-rare gas systems,[17] the Ne-rare gas systems have nearly the same well depths, and the reciprocal relation for ε; $\varepsilon_{ij} = 2\varepsilon_{ii}\varepsilon_{jj}/(\varepsilon_{ii}+\varepsilon_{jj})$ gives somewhat better predictions that other combination rules but cannot be regarded as adequate. The reduced forms of all Ne-rare gas systems are plotted in Fig. 5 and are also tabulated in Table III. The differences between the Ne_2 potential and asymmetric Ne-rare gas systems are as significant as the differences among asymmetric Ne-rare gas systems. The Ne-Xe potential is more attractive at large distances and more repulsive at short distances than the Ne-Ar potential.

Some previously proposed potentials[18-26,28] for Ne-Ar, Ne-Kr, and Ne-Xe are tabulated in Tables IV, V, and VI for comparison. These potentials are mainly constructed from transport properties and semi-empirical calculations. Some Morse-6 and exp-6 potentials are in fair agreement with MSV potentials dervied in this work. Differential cross sections calculated for some of these potentials are shown in Figs. 6 and 7; the potentials themselves are shown in Figs. 8 and 9.

For Ne + Ar the Morse-6 potential of Gaydaenko et. al.[25] (No. 3 in Table IV) was shown by Konowalow et. al.[19] to give a rather good fit to the second virial coefficients; the differential cross section calculated from this potential is also quite close to experimental results except that the general fall-off of the differential cross section as a function of the scattering angle seems somewhat faster. Diffusion coefficients in the temperature range in which the average relative kinetic energy of atoms is much higher than the potential well depth are more sensitive to the repulsive part of the potential than the

attractive part, since differential cross sections are weighted by a (1-cos θ) factor in the total diffusion cross section, thus reducing the importance of the contribution from small angle scattering, which is more sensitive to the attractive part of the potential. Various exp-6 potentials, obtained from idffusion coefficients by R. J. J. van Heijningen et. al.[18] over the temperature range from 100°K to 400°K, do agree more closely in the repulsive part of the potential than the potential well. As shown in Fig. 8(b), the ESMSV potential has substantial overlap with these potentials in the repulsive region, especially when α = 15. For the Ne-Kr potential, an exp-6 potential with α = 15 [18] agrees almost exactly in the repulsive region with the MSV potential derived in this work as shown in Fig. 9. Potential parameters for LJ (12,6) and exp-6 potentials have been determined by Hogervorst[28] from accurate measurements of diffusion coefficients between 100 and 1600°K. The well depth, ε, for Ne-Ar obtained in his work is about 10% smaller than our present work, but both ε and r_m for Ne-Kr and Ne-Xe agree with our present work within the uncertainties of the determinations of these parameters. The facts that nearly identical values of ε and r_m are obtained for both LJ (12,6) and exp-6 potential forms in Hogervorst's work led him to conclude that the diffusion coefficients could provide an estimate of ε and r_m together with the steepness of the repulsive part of the potentials but not the detailed information on the form of the potentials. The form of the potential, especially around the attractive well, can be better determined from the measurements of elastic differential cross sections.

ACKNOWLEDGEMENTS

This research was supported by the U. S. Atomic Energy Commision and in part by the Advanced Research Projects Agency, Louis Block Fund of The University of Chicago. YTL acknowledges the Teacher-Scholar Grant from the Camille and Henry Dreyfus Foundation.

REFERENCES

1. J. M. Parson, T. P. Schafer, F. P. Tully, P. E. Siska, Y. C. Wong and Y. T. Lee, J. Chem. Phys., 53, 2123 (1970). R. W. Bickes, Jr. and R. B. Bernstein, Chem. Phys. Letters, 4, 111 (1970).
2. N. J. Brown and R. J. Munn, J. Chem. Phys., 57, 2216 (1972).
3. J. M. Parson, P. E. Siska and Y. T. Lee, J. Chem. Phys., 56, 1511 (1972).
4. J. M. Farrar and Y. T. Lee, J. Chem. Phys., 56, 5801 (1972).
5. D. W. Marquardt, J. Soc. Ind. App. Math., 11, 431 (1963).
6. R. G. Gordon, J. Chem. Phys., 48, 3929 (1968).
7. G. Starkschall and R. G. Gordon, J. Chem. Phys., 54, 663 (1971).
8. P. W. Langhoff, R. G. Gordon and M. Karplus, J. Chem. Phys., 55, 2126 (1971).
9. J. Brewer and R. G. Vaughn, J. Chem. Phys., 50, 2960 (1969).
10. J. Brewer, Air Force Office of Scientific Research Report No. 67-2795 (1967).
11. F. T. Smith, Phys. Rev., A5, 1708 (1972).
12. J. O. Hirschfelder, C. F. Curtiss and R. B. Bird, Molecular Theory of Gases and Liquid (Wiley, New York 1964), Chapter 6.
13. R. J. Munn, J. Chem. Phys., 40, 1439 (1964).
14. R. J. Munn and F. J. Smith, J. Chem. Phys., 43, 3998 (1965).
15. M. L. Klein and R. J. Munn, J. Chem. Phys., 47, 1035 (1967).
16. F. Kohler, Monatsh. Chem., 88, 857 (1957).
17. C. H. Chen, P. E. Siska and Y. T. Lee, J. Chem. Phys., 59, 601 (1973).

18. R. J. J. van Heijningen, J. P. Harpe and J. J. M. Beenakker, Physica, 38, 1 (1968).

19. D. D. Konowalow and D. S. Zakheim, J. Chem. Phys., 57, 4375 (1972).

20. D. D. Konowalow, J. Chem. Phys., 50, 12 (1969).

21. B. N. Srivastava and K. P. Srivastava, J. Chem. Phys., 30, 984 (1969).

22. R. K. Nesbet, J. Chem. Phys., 48, 1419 (1968).

23. E. A. Mason, J. Chem. Phys., 23, 49 (1955).

24. K. P. Srivastava, J. Chem. Phys., 28, 543 (1958).

25. V. I. Gaydaenko and V. K. Nikulin, Chem. Phys. Letter, 7, 360 (1970).

26. R. L. Matcha and R. K. Nesbet, Phys. Rev., 160, 72 (1967).

27. J. M. Farrar, Y. T. Lee, V. V. Goldman and M. L. Klein, Chem. Phys. Letters, 19, 359 (1973).

28. W. Hogervorst, Physica, 51, 59 (1971).

FIGURE CAPTIONS

Fig. 1. Laboratory angular distributions of elastically scattered Ne for the Ne + Ar, Ne + Kr and Ne + Xe systems. Solid curves are calculated from best fit potentials.

Fig. 2. Potentials of Ne + Ar, Ne + Kr and Ne + Xe obtained in this work.

Fig. 3. Comparison of second virial coefficients calculated from best fit potentials with experimental data.

Fig. 4. Sensitivity of differential cross sections of Ne + Ar to the variation of ε and r_m for ESMSV potentials listed in Table I.

(a) Variation of r_m, keeping ε constant.

(b) Variation of ε, keeping r_m constant.

(c) Simultaneous variation of r_m and ε, keeping εr_m nearly constant.

Fig. 5. Reduced potentials of Ne + Ne, Ne-Ar, Ne + Kr and Ne + Xe.

Fig. 6. Laboratory angular distributions of elastically scattered Ne for the Ne + Ar system compared with previously proposed potentials. Numbered curves are calculated from corresponding potentials of Table IV. The experimental data are shown twice to allow a clear comparison with the calculated results.

Fig. 7. Laboratory angular distributions of elastically scattered Ne for the Ne + Kr system is compared with a previously proposed Ne + Kr potential listed in Table V. (No. 11).

Fig. 8. Comparison of fitted ESMSV potential (solid curves) with previously proposed potentials for Ne + Ar. The fitted curve is replotted twice for ease of comparison. Numbering scheme corresponds to that of Table IV.

Fig. 9. Comparison of fitted MSV potential with a previously proposed Ne + kr potential listed in Table V (No. 11).

TABLE I.

ESMSV POTENTIAL PARAMETERS

	Ne-Ne	Ne-Ar	Ne-Kr	Ne-Xe
ϵ (Kcal/mole)	.085	0.143	0.148	0.149
r_m (Å)	3.11	3.43	3.58	3.745
β	2.032	6.6	7.0	7.9
A	.132	0.245	----	----
α	4.0	17.55	----	----
C_6 (Kcal/mole Å^6)	90.4	282	392.5	570
C_8 (Kcal/mole Å^8)	220.6	590	810	1210
C_{10} (Kcal/mole Å^{10})	----	----	----	----
a_1	6.66	2.106	----	----
a_2	-17.05	-36.07	----	----
a_3	-36.32	-251.69	----	----
a_4	-14.119	-747.52	----	----
b_1	-7.5	-0.61	-.865	-.92
b_2	1.976	1.89	1.259	1.083
b_3	-3.999	-5.59	-2.997	-2.462
b_4	-.1522	5.64	2.074	1.555
X_1	0.5	0.8	----	----
X_2	0.826	0.88	----	----
X_3	1.1097	1.148	1.065	1.042
X_4	1.4	1.36	1.71	1.86

TABLE II

Potential Parameters from Combination Rules Compared with Experiment.

System[a]	Internuclear Distance (Å) σ_{ii}	σ_{jj}	σ_{ij}[b]	σ_{ij}(Expt)	ε_{ii}	ε_{jj}	ε_{ij}[c]	ε_{ij}[d]	ε_{ij}[e]	ε_{ij}[f]	ε_{ij}(Expt)
Ne-Ar	2.75[h]	3.34[g]	3.05	3.09	42.7	143	73.6	78.14	75.18	65.75	71.94
Ne-Kr	2.75	3.64[h]	3.20	3.22	42.7	198	83.92	91.94	85.92	70.26	74.47
Ne-Xe	2.75	3.81[h]	3.28	3.42	42.7	276	93.06	108.5	100.2	73.94	74.98

(a) The subscripts i ≡ Ne, j ≡ rare gas partner

(b) $\sigma_{ij} = \frac{1}{2}(\sigma_{ii} + \sigma_{jj})$

(c) $\varepsilon_{ij} = 2a_i a_j/\sigma_{ij}^6(\gamma_{ii} + \gamma_{jj})$; a_i, a_j, a_k are atomic polarizability i $\gamma_{ii} \equiv (a_i^2/\varepsilon_{ii}\sigma_{ii}^6)$; σ_{ij} obtained (from (b).

(d) $\varepsilon_{ij} = (\varepsilon_{ii}\varepsilon_{jj})^{1/2}$.

(e) $\varepsilon_{ij} = (\frac{1}{\sigma_{ij}})^6 [\varepsilon_{ii}\sigma_{ii}^6 \varepsilon_{jj}\sigma_{jj}^6]^{1/2}$; σ_{ij} obtained from (a).

(f) $\varepsilon_{ij} = 2\varepsilon_{ii}\varepsilon_{jj}/(\varepsilon_{ii} + \varepsilon_{jj})$.

(g) Ref. 27

(h) Ref. 28

TABLE III.

ESMSV REDUCED POTENTIAL

X	Ne-Ne	Ne-Ar	Ne-Kr	Ne-Xe
0.50	7.807×10^{2}	1.590×10^{3}	1.030×10^{3}	2.593×10^{3}
0.55	4.147×10^{2}	6.611×10^{2}	4.979×10^{2}	1.154×10^{3}
0.60	2.12×10^{2}	2.749×10^{2}	2.375×10^{2}	5.084×10^{2}
0.65	1.014×10^{2}	1.143×10^{2}	1.111×10^{2}	2.20×10^{2}
0.70	4.423×10^{1}	4.753×10^{1}	5.035×10^{1}	9.304×10^{1}
0.75	1.710×10^{1}	1.976×10^{1}	2.161×10^{1}	3.752×10^{1}
0.80	5.702	8.218	8.334	1.386×10^{1}
0.85	1.498	3.460	2.451	4.156×10
0.90	-2.233×10^{-1}	-1.262×10^{-1}	2.77×10^{-2}	4.482×10^{-1}
0.95	-8.619×10^{-1}	-8.471×10^{-1}	-8.244×10^{-1}	-7.654×10^{-1}
1.00	-1.000	-1.000	-1.000	-1.000
1.05	-9.266×10^{-1}	-9.210×10^{-1}	-9.128×10^{-1}	-8.957×10^{-1}
1.10	-7.806×10^{-1}	-7.666×10^{-1}	-7.598×10^{-1}	-7.529×10^{-1}
1.15	-6.3×10^{-1}	-6.058×10^{-1}	-6.25×10^{-1}	-6.27×10^{-1}
1.20	-4.990×10^{-1}	-4.687×10^{-1}	-5.09×10^{-1}	-5.180×10^{-1}
1.25	-3.73×10^{-1}	-3.623×10^{-1}	-4.1×10^{-1}	-4.24×10^{-1}
1.30	-2.972×10^{-1}	-2.802×10^{-1}	-3.281×10^{-1}	-3.431×10^{-1}
1.35	-2.270×10^{-1}	-2.2005×10^{-1}	-2.6×10^{-1}	-2.755×10^{-1}
1.40	-1.762×10^{-1}	-1.754×10^{-1}	-2.048×10^{-1}	-2.188×10^{-1}
1.45	-1.418×10^{-1}	-1.415×10^{-1}	-1.61×10^{-1}	-1.78×10^{-1}
1.50	1.148×10^{-1}	-1.147×10^{-1}	-1.264×10^{-1}	-1.358×10^{-1}

TABLE III. --Continued

X	Ne-Ne	Ne-Ar	Ne-Kr	Ne-Xe
1.60	-7.697×10^{-2}	-7.720×10^{-2}	-8.069×10^{-2}	-8.470×10^{-2}
1.70	-5.295×10^{-2}	-5.326×10^{-2}	-5.510×10^{-2}	-5.624×10^{-2}
1.80	-3.725×10^{-2}	-3.756×10^{-2}	-3.888×10^{-2}	-4.107×10^{-2}
1.90	-2.673×10^{-2}	-2.701×10^{-2}	-2.798×10^{-2}	3.030×10^{-2}
2.00	-1953×10^{-2}	-1.976×10^{-2}	-2.048×10^{-2}	2.222×10^{-2}
2.10	-1.449×10^{-2}	-1.469×10^{-2}	-1.523×10^{-2}	-1.654×10^{-2}
2.20	-1.091×10^{-2}	-1.107×10^{-2}	-1.148×10^{-2}	-1.249×10^{-2}
2.30	-8.319×10^{-3}	-8.456×10^{-3}	-8.770×10^{-3}	-9.547×10^{-3}
2.40	-6.421×10^{-3}	-6.533×10^{-3}	-6.777×10^{-3}	-7.384×10^{-3}
2.50	-5.009×10^{-3}	-5.102×10^{-3}	-5.294×10^{-3}	-5.772×10^{-3}
ϵ (Kcal/mole)	.085	0.143	0.148	0.149
r_m (Å)	3.11	3.43	3.58	3.745

TABLE IV.

Potentials for Ne + Ar System

System	No.	Potential Form	ϵ (°K)	r_m (Å)	α	β	Reference	σ_{12} (Å)	Standard deviation of 2nd virial coeff. fitting
Ne + Ar	1	ESMSV	71.94	3.43	17.725	6.6	this work	3.06	1.02
	2	LJ(20, 6)	70.3±2.2	3.48±0.05			1		
	3	Morse-6	69.5	3.3981		6.388	19, 25		0.72
	4	Morse-6	70.1	3.40		6.383	19, 26		1.76
	5	Morse-6	73.5	3.55		6.447	19, 26		1.33
	6	Exp-6	63.8±5	3.638	13.22±.0		20		
	7	Exp-6	63.79	3.638	13.22		22		
	8	Exp-6	73.9	3.443	14.17		23		8.76
	9	Exp-6	68.42	3.491	14.35		24		
	10	Exp-6	42.8±2	3.83±.03	12		18		
	11	Exp-6	49.8±2	3.68±.02	13		18		
	12	Exp-6	55.1±2	3.58±.02	14		18		
	13	Exp-6	60.9±2.0	3.50±.02	15		18		
	14	Exp-6	64.5±4	3.46±0.03	15.5		28		
	15	LJ(12-6)	61.7±2.0				18	3.11±.02	
	16	LJ(12-6)	64.5				21	3.098	
	17	LJ(12-6)	69.5				21	3.067	
	18	LJ(12-6)	67.6				21	3.079	
	19	LJ(12-6)	64.5	3.47±.03			28	3.09±.03	

TABLE V.

Potentials for Ne + Kr System

System	No.	Potential Form	ε(°K)	r_m(Å)	α	β	σ_{12}(Å)	Reference	Standard deviation of 2nd virial coeff. fitting
Ne + Kr	1	MSV	74.47	3.58		7.0	3.226	this work	0.43
	2	LJ(20, 6)	78.22±2.2	3.6±.07				1	
	3	LJ(12, 6)	67.5				3.257	21	
	4	LJ(12, 6)	63.5				3.291	21	
	5	LJ(12, 6)	64.9				3.287	21	
	6	LJ(12, 6)	69.8±3.5				3.24±.02	18	
	7	LJ(12, 6)	71.5±3.5	3.62±.03			3.22±.03	28	
	8	Exp-6	52.8±3.5	3.94±.04	12			18	
	9	Exp-6	60.5±3.5	3.80±.03	13			18	
	10	Exp-6	65.8±3.5	3.71±.03	14			18	
	11	Exp-6	72.0±3.5	3.62±.03	15			18	3.00
	12	Exp-6	71.5±4	3.60±.03	15.5			28	

TABLE VI.

Potentials for Ne + Xe System

System	No.	Potential Form	ϵ(°K)	r_m(Å)	α	β	σ_{12}	Reference	Standard deviation of 2nd virial coeff. fitting
Ne + Xe	1	MSV	74.98	3.745		7.9	3.42	this work	0.64
	2	LJ(20, 6)	75.33±3.62	3.80±.01				1	
	3	Exp-6	61.9±5.0	4.01±.04	14			18	
	4	Exp-6	68.7±5.5	3.91±.04	15			18	
	5	Exp-6	73. ±4.	3.87±.04	15.5			20	
	6	LJ(12, 6)	69.1±6.0				3.48±.04	18	
	7	LJ(12, 6)	73. ±4	3.88±.04			3.46±.03	28	

TABLE VII

DIFFUSION COEFFICIENTS ($cm^2 sec^{-1}$)

T(K)	NEON - ARGON			NEON - KRYPTON			NEON - XENON		
	Calculated	Measured[a]	% Difference	Calculated	Measured[a]	% Difference	Calculated	Measured[a]	% Difference
300	.318	.323	-1.5	.262	.262	0.0	.220	.219	0.5
350	.415	.421	-1.4	.342	.342	0.0	.286	.286	0.0
400	.521	.525	-0.8	.429	.431	-0.5	.358	.359	-0.3
450	.637	.635	0.3	.525	.526	-0.2	.436	.440	-0.9
500	.761	.765	-0.5	.627	.627	0.0	.520	.523	-0.6
550	.895	.892	0.3	.737	.737	0.0	.610	.615	-0.8
600	1.037	1.045	-0.8	.853	.850	0.4	.705	.710	-0.7
700	1.345	1.355	-0.7	1.106	1.098	0.7	.911	.920	-1.0
800	1.685	1.675	0.6	1.384	1.38	0.4	1.14	1.16	-0.2
1000	2.453	2.43	0.9	2.01	2.01	0.0	1.65	1.68	-1.8
1200	3.332	3.31	0.7	2.73	2.71	0.7	2.23	2.26	-1.3
1400	4.317	4.24	1.8	3.54	3.51	0.9	2.87	2.92	-1.7

[a] Measurements of Hogervorst, Ref. 28.

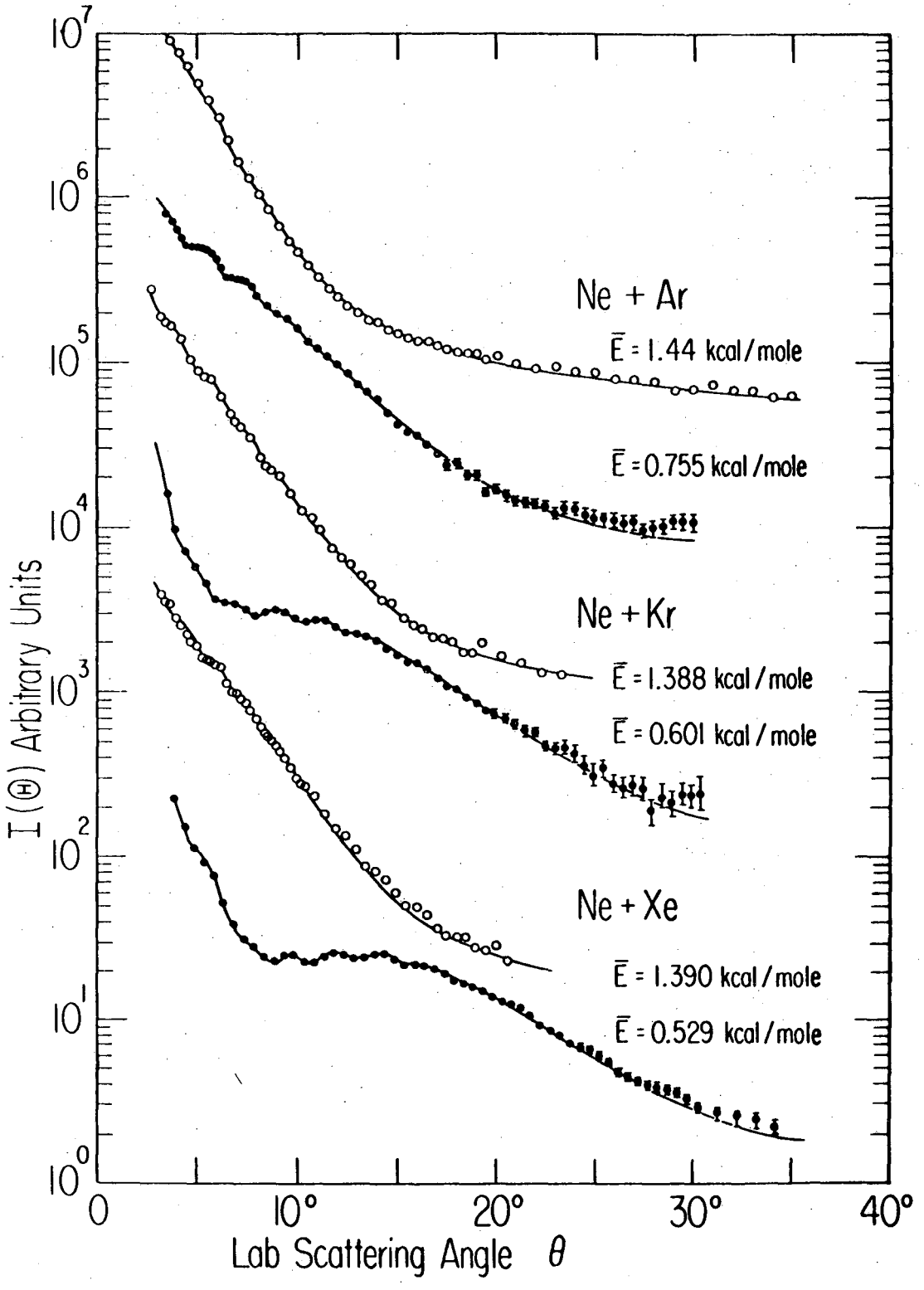
Ne + Ar
$\bar{E}$ = 1.44 kcal/mole
$\bar{E}$ = 0.755 kcal/mole
Ne + Kr
$\bar{E}$ = 1.388 kcal/mole
$\bar{E}$ = 0.601 kcal/mole
Ne + Xe
$\bar{E}$ = 1.390 kcal/mole
$\bar{E}$ = 0.529 kcal/mole
I(Θ) Arbitrary Units
Lab Scattering Angle θ
10^0
10^1
10^2
10^3
10^4
10^5
10^6
10^7
0
10°
20°
30°
40°

Fig. 1

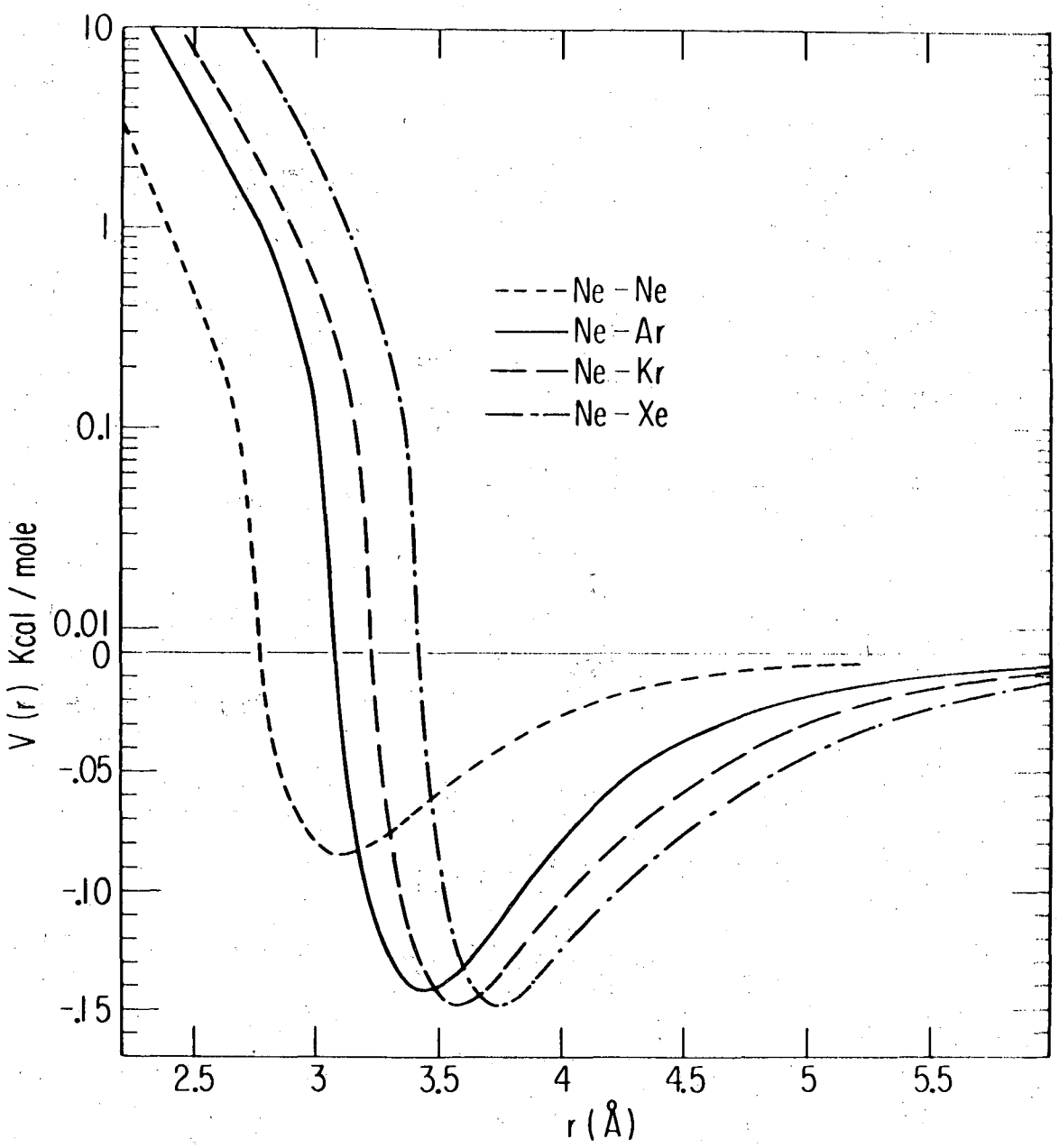

Fig. 2

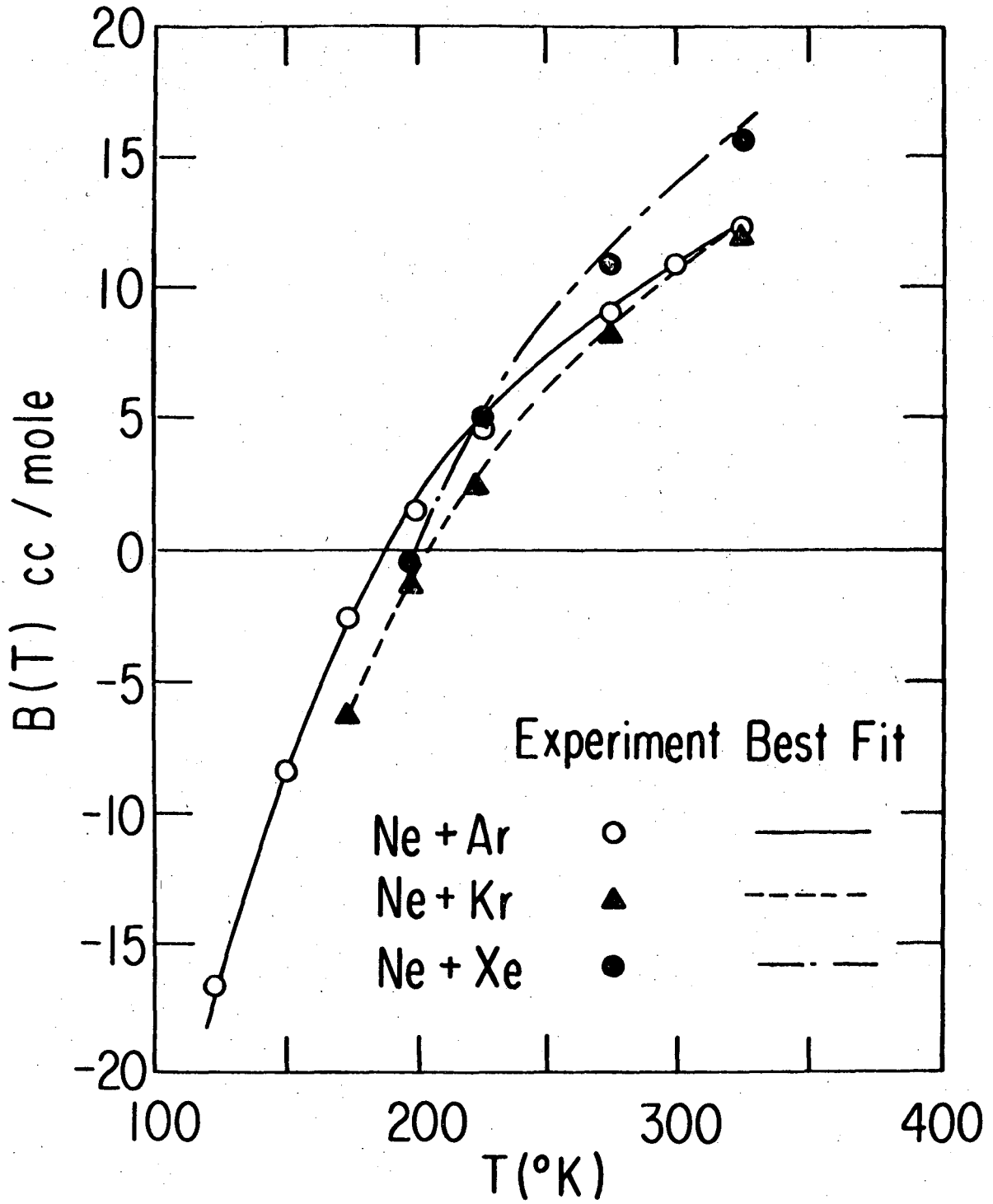
20
15
10
5
0
-5
-10
-15
-20
100
200
300
400
B(T) cc / mole
T(°K)
Experiment Best Fit
Ne + Ar
Ne + Kr
Ne + Xe

Fig. 3

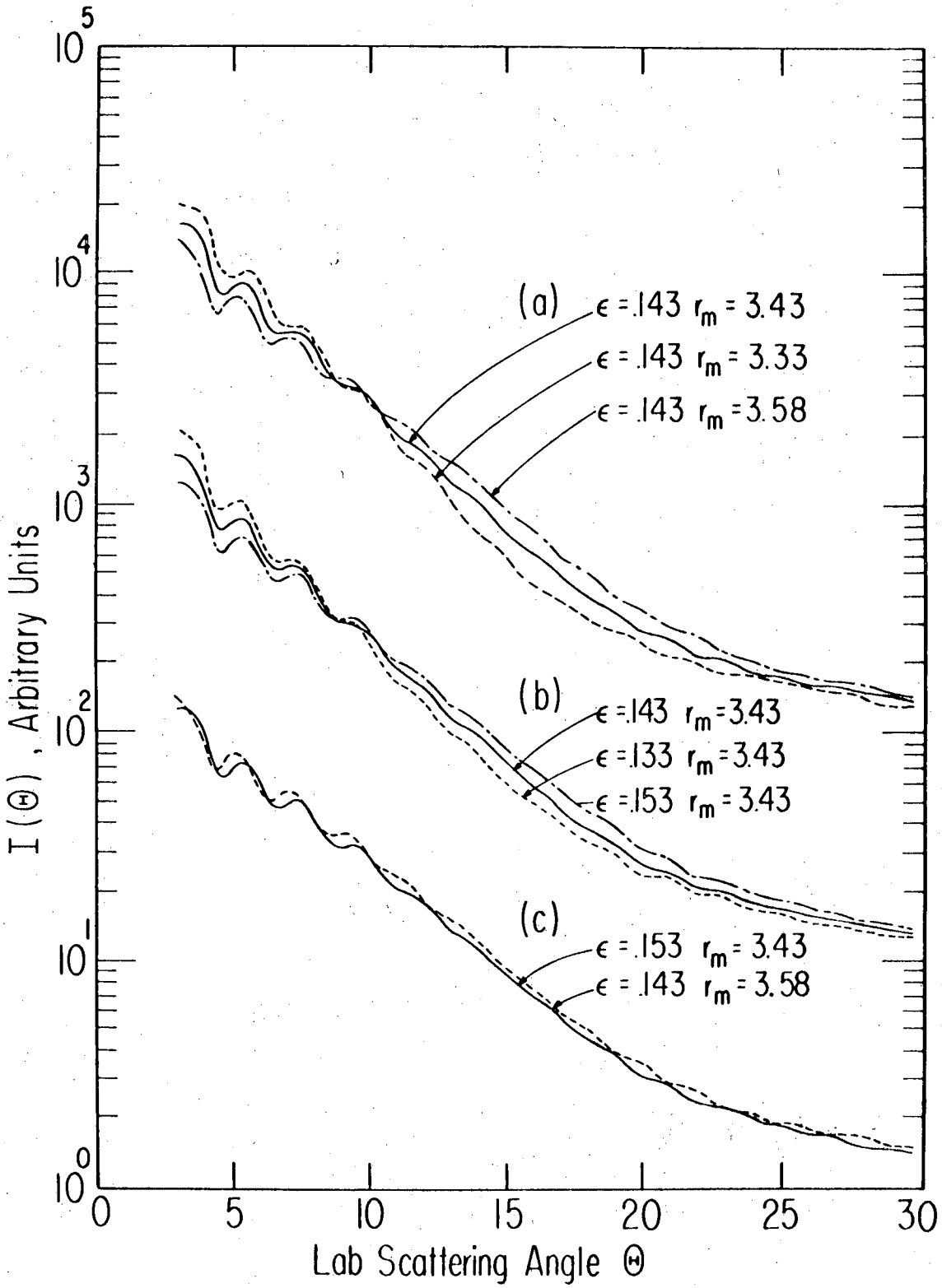

Fig. 4

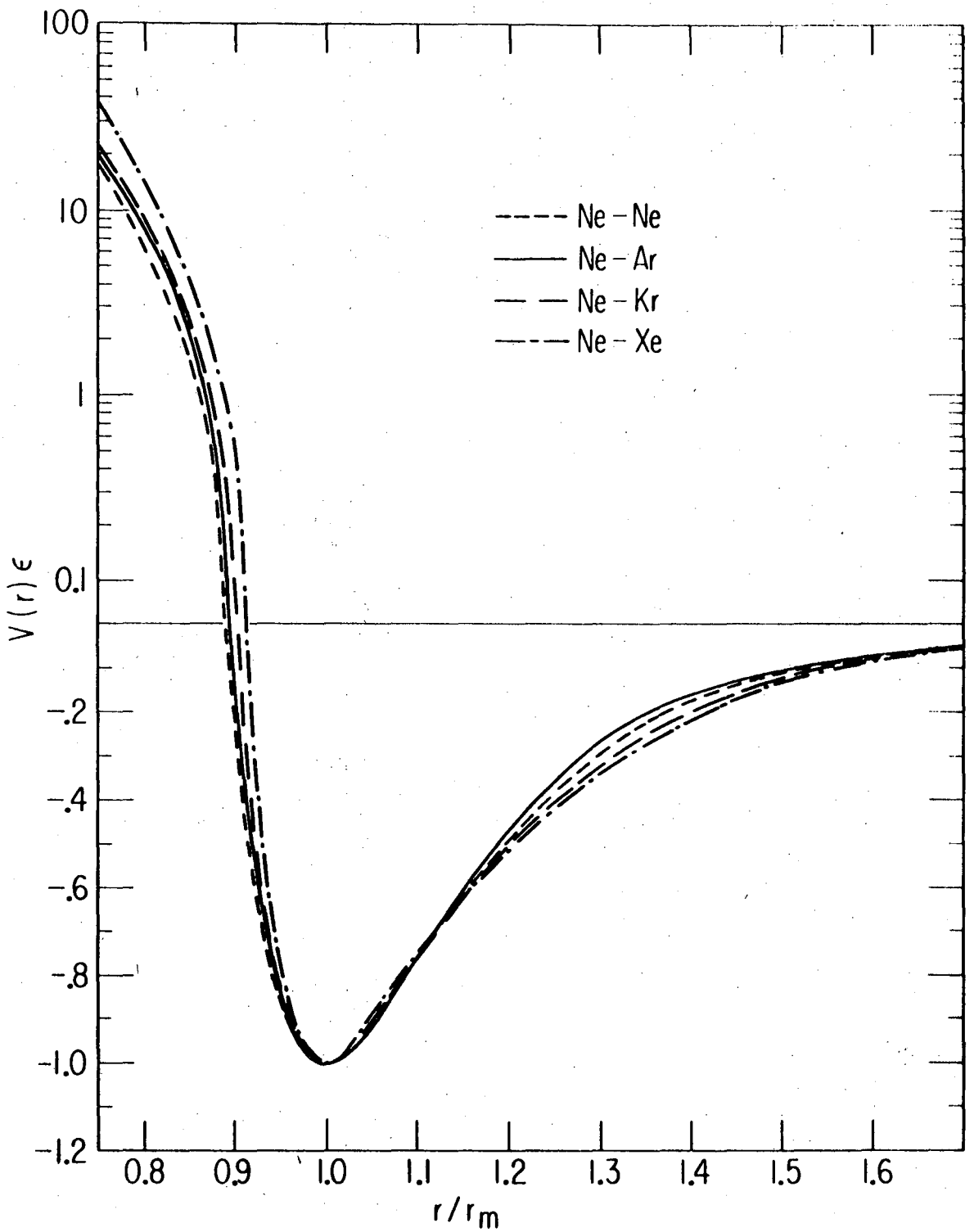
100
10
1
0.1
-.2
-.4
-.6
-.8
-1.0
-1.2
V(r) ϵ
0.8
0.9
1.0
1.1
1.2
1.3
1.4
1.5
1.6
r/rm
Ne – Ne
Ne – Ar
Ne – Kr
Ne – Xe

Fig. 5

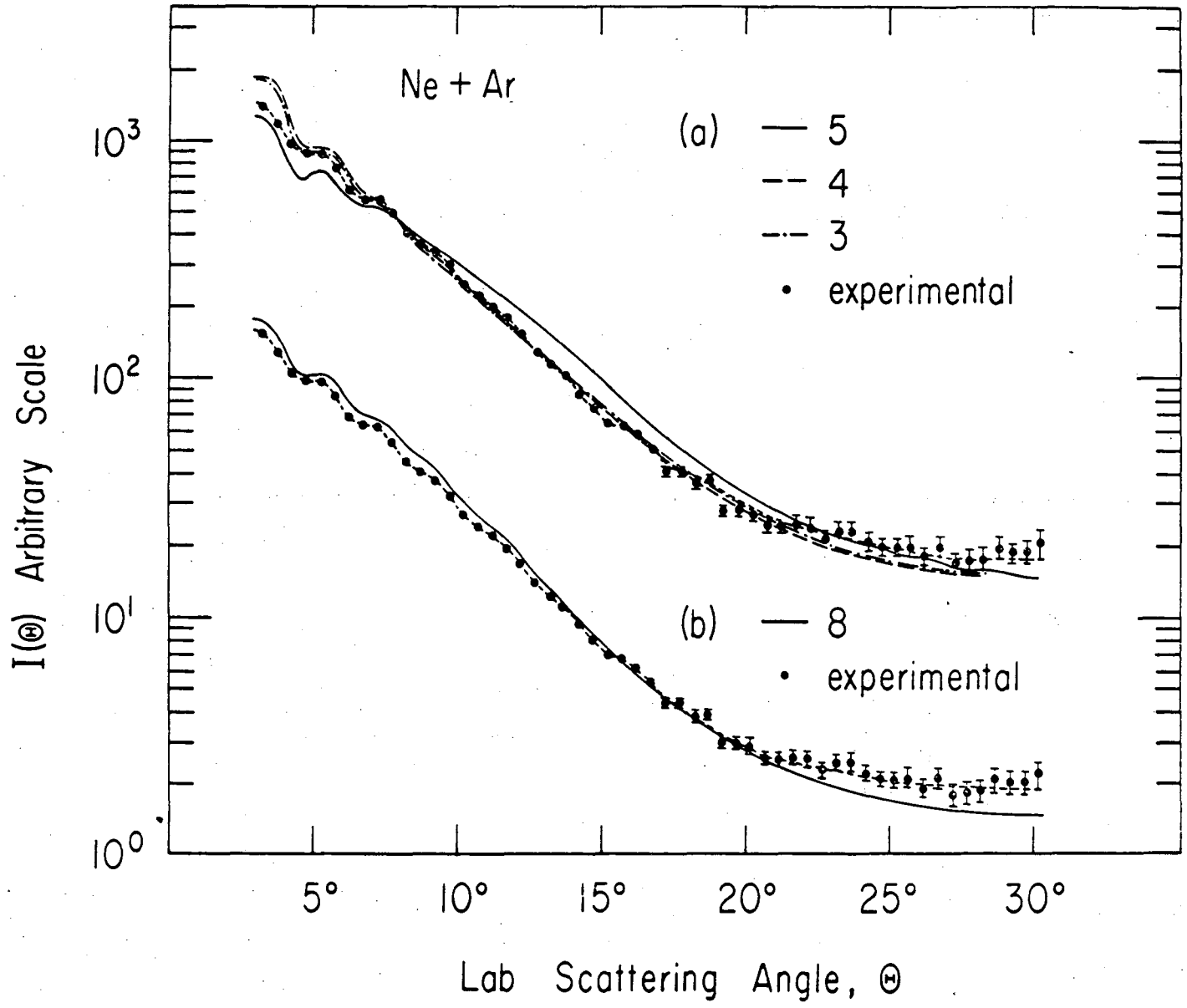

Fig. 6

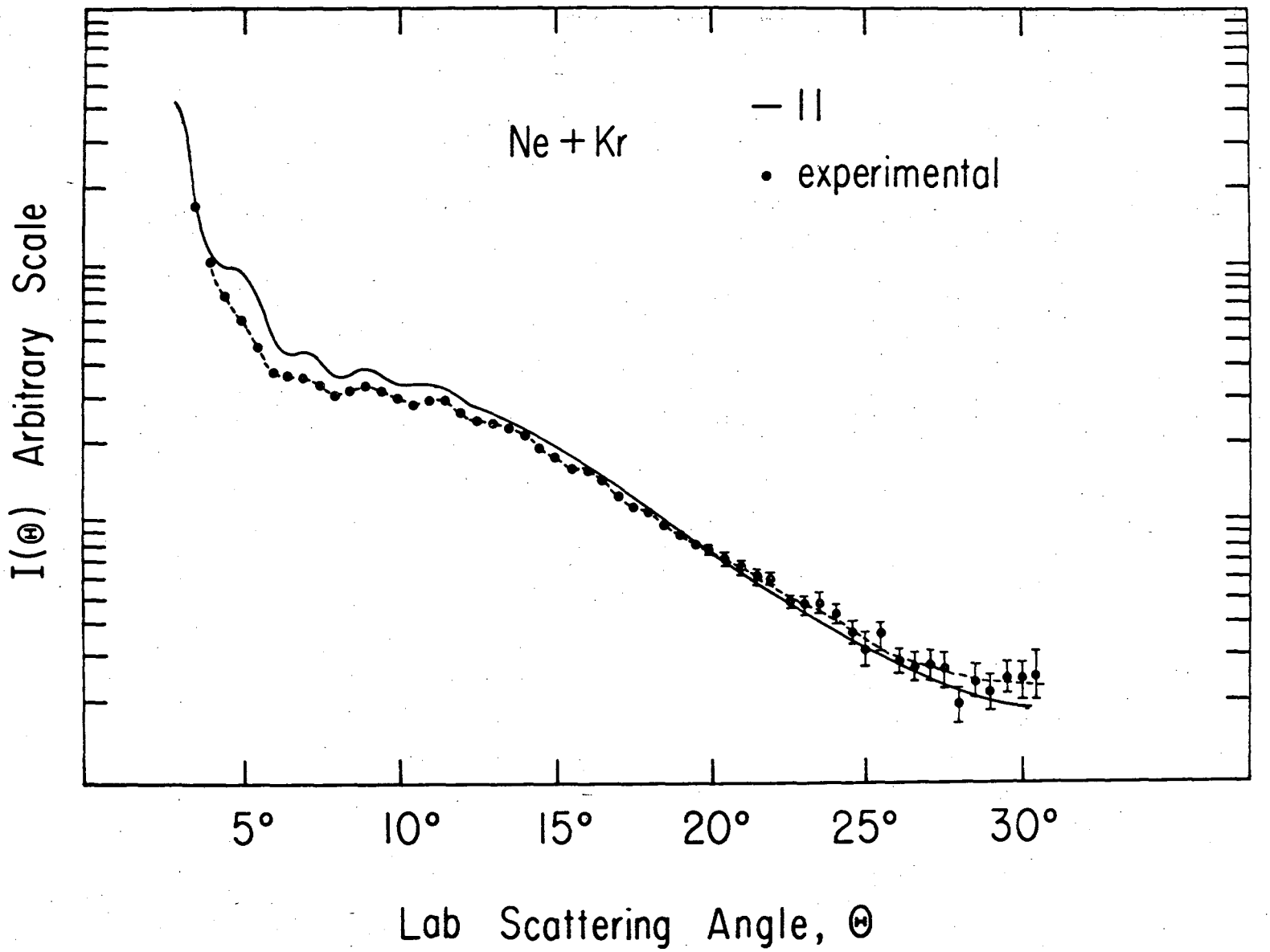
— II
Ne + Kr
• experimental
I(Θ) Arbitrary Scale
5°
10°
15°
20°
25°
30°
Lab Scattering Angle, Θ

Fig. 7

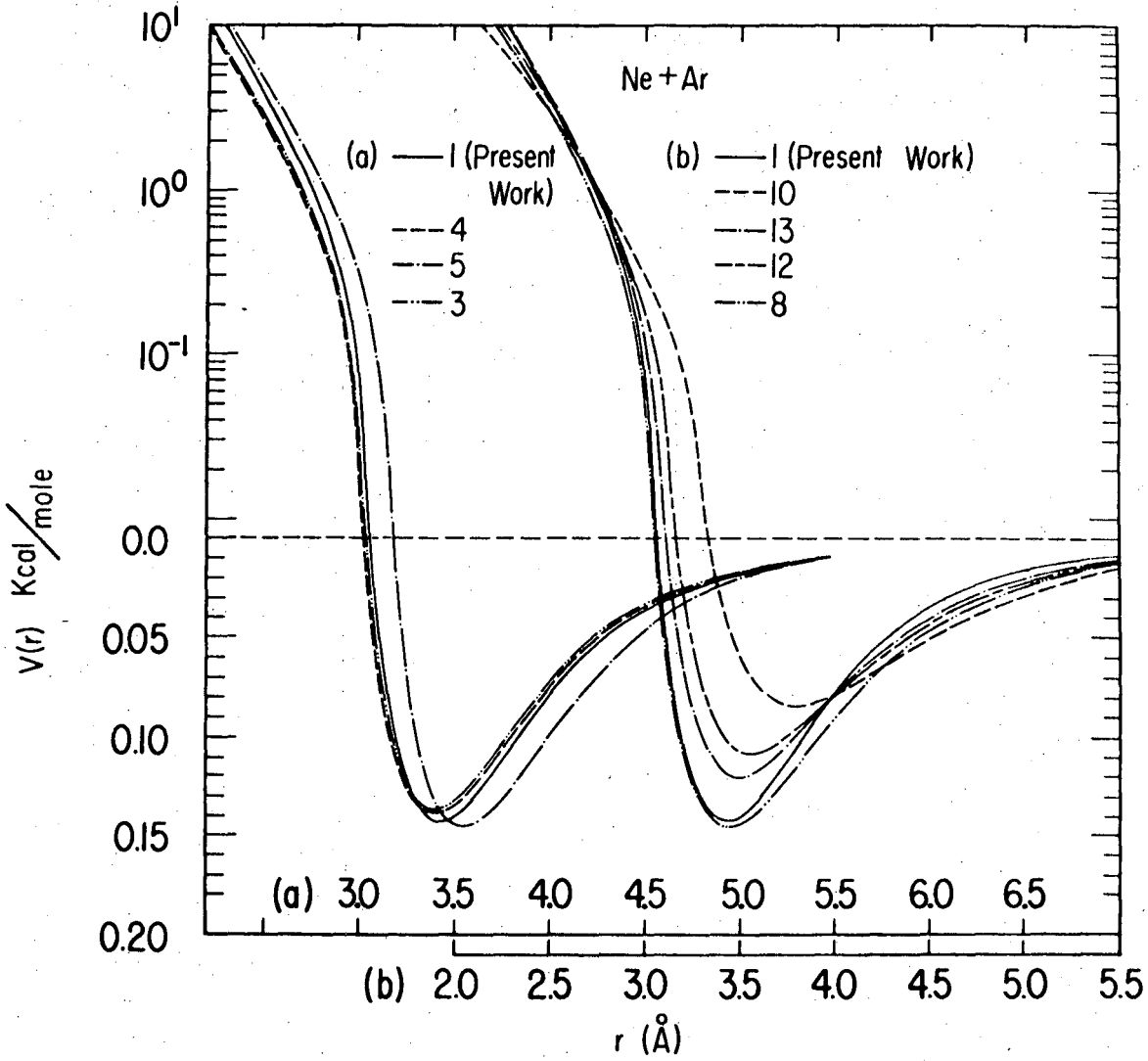

Fig. 8

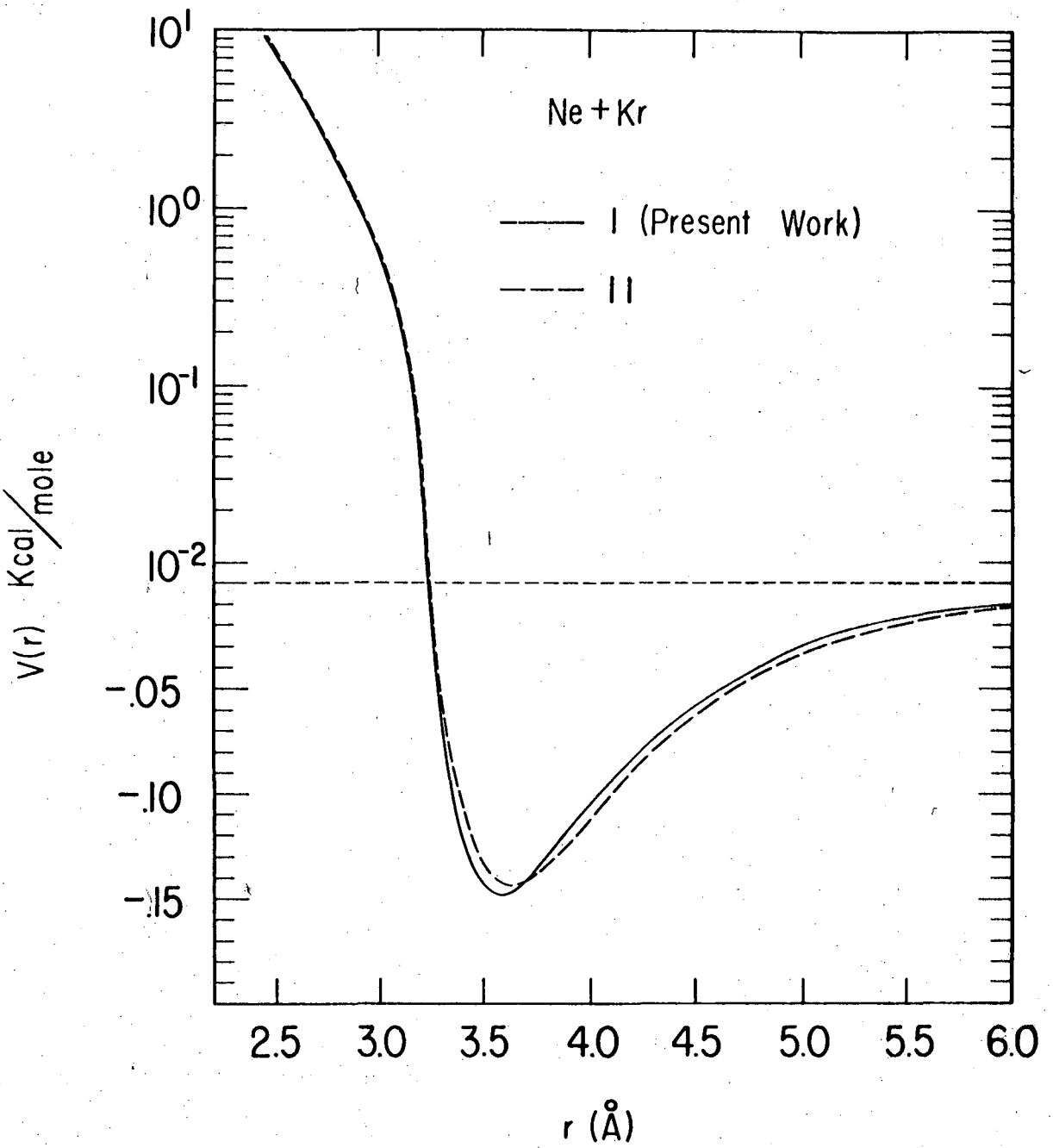
Ne + Kr
I (Present Work)
II
V(r) Kcal/mole
r (Å)
10¹
10⁰
10⁻¹
10⁻²
-.05
-.10
-.15
2.5
3.0
3.5
4.0
4.5
5.0
5.5
6.0

Fig. 9

APPENDICES

A. Mechanical & Vacuum Layout of the Photoionization Apparatus

Figure 1 and Fig. 2 show the detailed assembly diagrams of the photoionization apparatus in plane view and vertical view respectively. The arrangement and operation of the apparatus has been described briefly in the experimental part of chapter three. It is the purpose of this appendix to give a more detailed description on the differential pumping system for the monochromator.

The pumping arrangement for the monochromator is shown in Fig. 3. In order to excite the He Hopfield continuum, the lamp is at a steady pressure P_1 = 100 torr (He). If the area of the optical entrance slit between the lamp and the first differential pumping chamber is 100μ (width) × 0.5 cm (height) = 0.005 cm^2, this corresponds to a conductance for He of C_1 = 0.225ℓ/sec. The throughput of He from the lamp to the first differential pumping chamber is

$$Q_1 = (P_1-P_2)(0.225\ell/s) \doteq P_1(0.225\ell/s)$$
$$= 45\ (\text{torr}\cdot\ell)/\text{sec}.$$

The Roots pump has a pumping speed S_2 = 300 c.f.m. = 141 ℓ/sec and this gives a steady pressure

$$P_2 = \frac{45}{141}\ \text{torr} = 0.32\ \text{torr}.$$

The area of slit 2 is 0.183 cm (width) × 0.498 (height) = 0.090 cm^2, which corresponds to a conductance for He of C_2 = 4.05 ℓ/sec. The second differential pumping region is pumped by an ejector pump which has a pumping speed of S_3 = 300 ℓ/sec. The steady pressure is

$$P_3 = \frac{(4.05)(0.32)}{300} = 4.3 \times 10^{-2} \text{ torr.}$$

The area of the third slit is 0.35 cm (width) × 0.584 cm (height) = 0.204 cm^2, and this gives a conductance for He of C_3 = 9.2 ℓ/sec. The pumping speed of the 6" diffusion pump for He is ≈ 2500 ℓ/sec. Thus, the pressure in the main chamber of the monochromator is

$$P_3 = \frac{9.2 \times 4.3 \times 10^{-2}}{2500} = 1.5 \times 10^{-4} \text{ torr.}$$

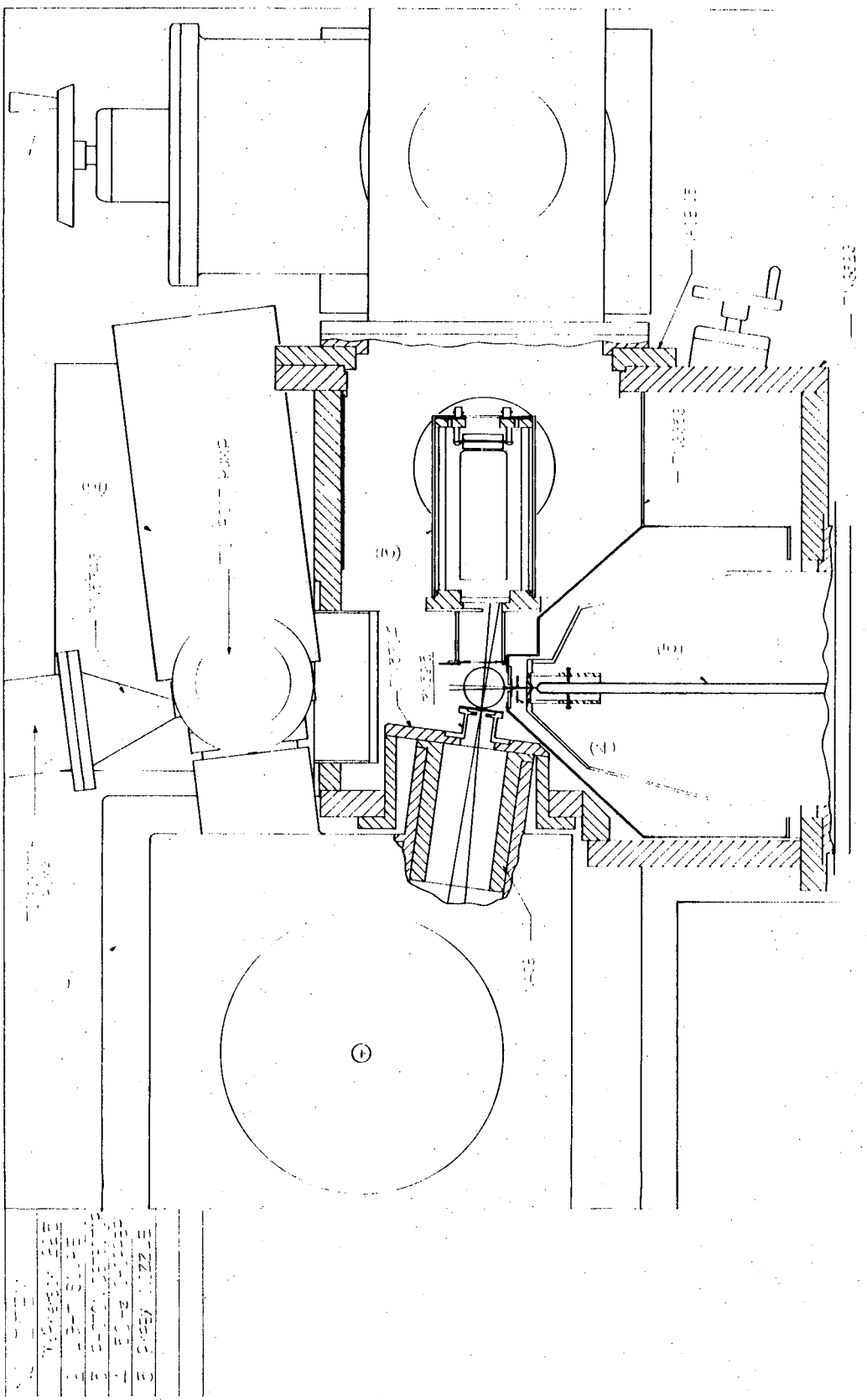

Fig. 1. Assembly diagram of the photoionization apparatus (Plane view)

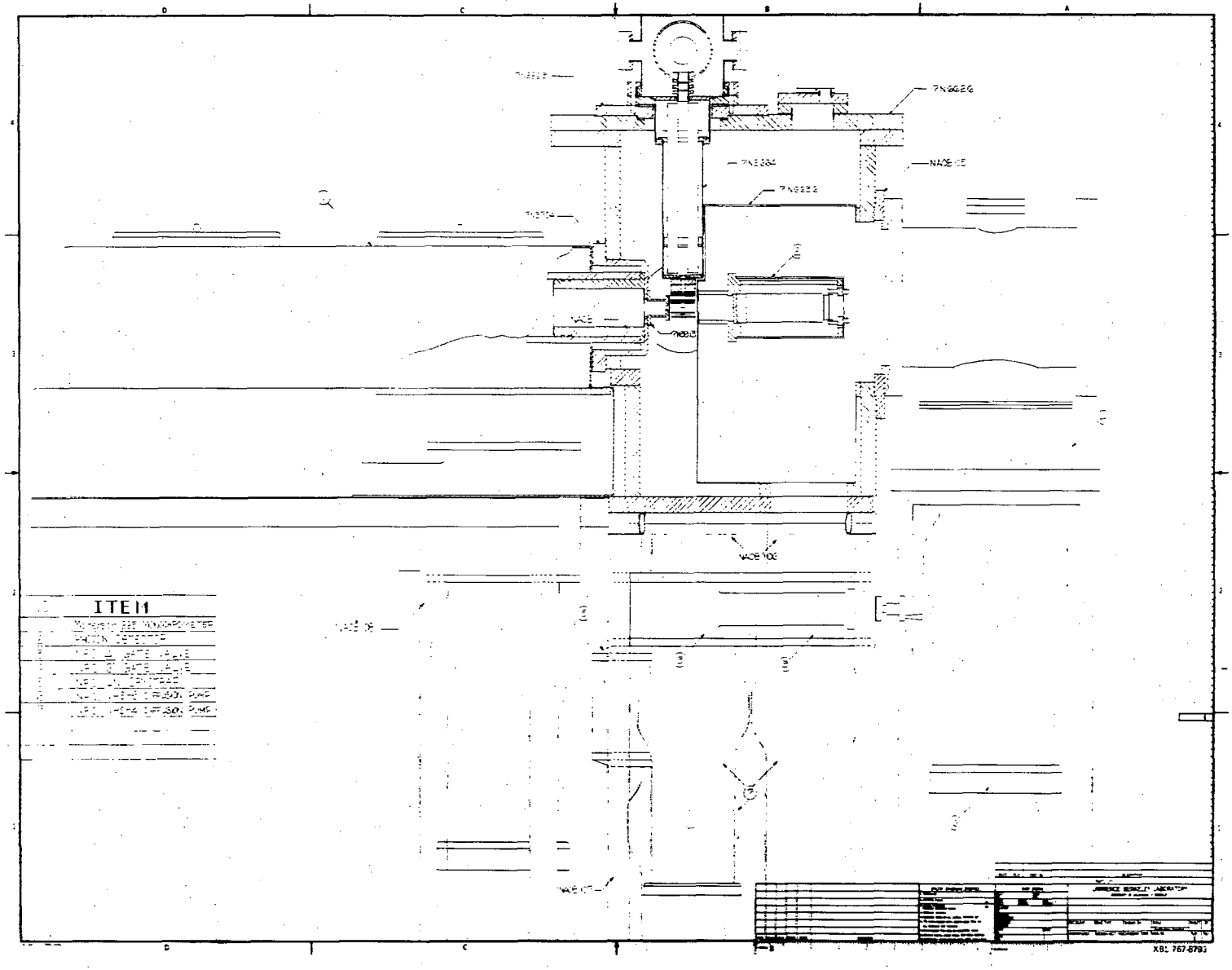

Fig. 2. Assembly diagram of the photoionization apparatus (vertical view).

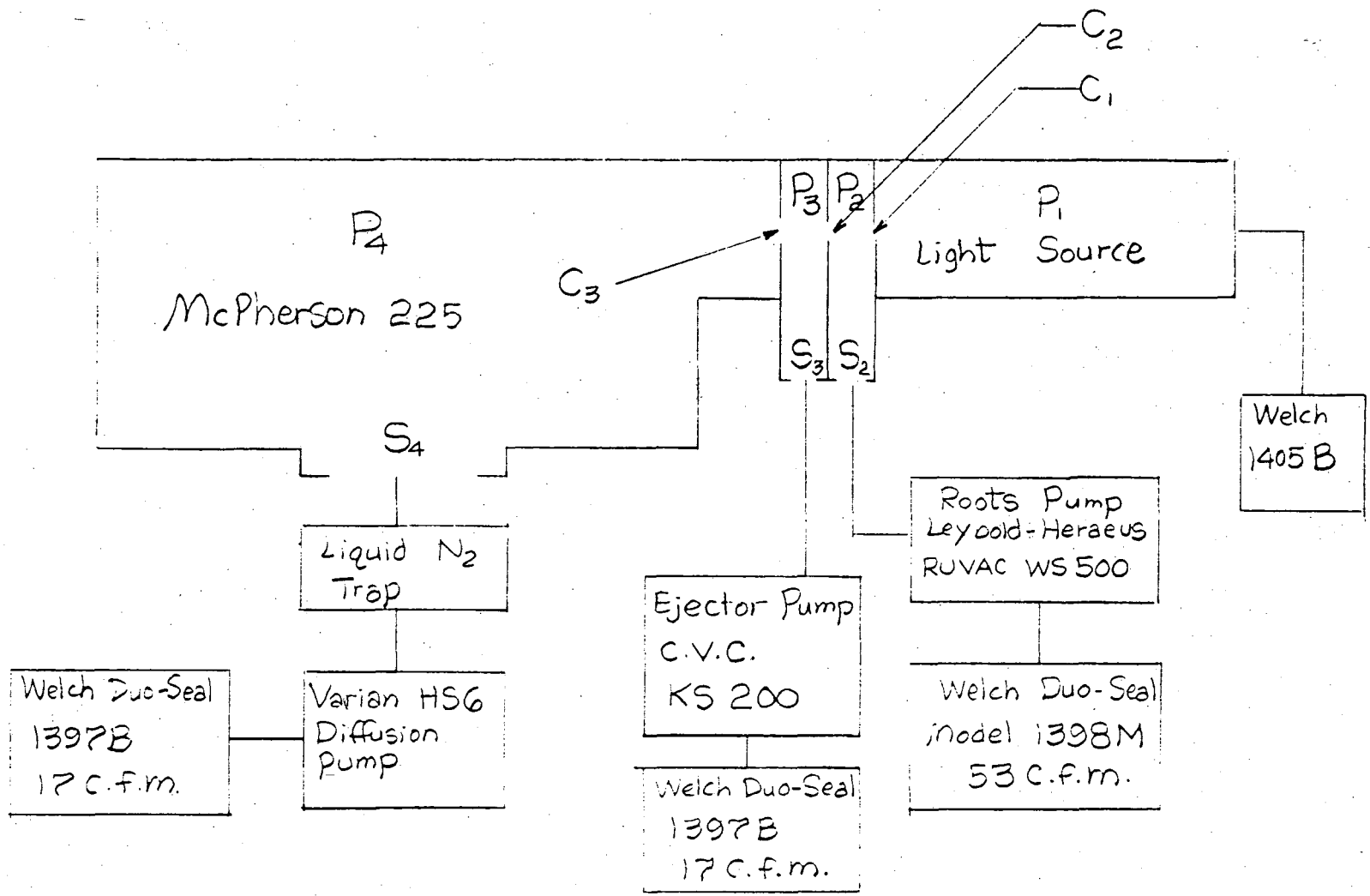

Fig. 3. Pumping Assembly for monochromator

B. Molecular Beam Production System

The pumping and mechanical arrangement for the molecular beam production system is shown in Fig. 1. The exhausted chamber is pumped by a 10" diffusion pump (Varian HS 10) which has a nominal pumping speed of $S_1 \approx 4000$ ℓ/sec, and the buffer chamber is pumped by a 4" diffusion pump (Varian VHS4) with an effective pumping speed of about $S_2 = 550$ ℓ/s (used with a gate valve). The main chamber is pumped by two 4" and one 6" diffusion pumps which is estimated to have an effective pumping speed of $S_3 = 2500$ ℓ/sec.

Using argon gas as an example, a source pressure of 760 torr at room temperature (298°K) corresponds to the mass flow through the nozzle and is described by

$$\dot{m} = 14.3\, D_o^2 \cdot P_o \quad \frac{\text{torr}\cdot\text{lit}}{\text{sec}} \tag{B.1}$$

$$= (14.3)(0.0127)^2 \cdot (760)$$

$$= 1.75\ \frac{\text{torr}\cdot\text{lit}}{\text{sec}}$$

where $D_o = 0.0127$ cm is the diameter of the nozzle

$P_o = 760$ torr is the nozzle stagnation pressure.

Hence the normal pressure of the exhausted chamber is

$$P_1 = (1.75\ \frac{\text{torr}\cdot\text{lit}}{\text{sec}})/4000\ \text{lit/sec}$$

$$= 4.4 \times 10^{-4}\ \text{torr}$$

The solid angle subtended by a 0.0635 cm diameter skimmer is

$$\Delta\Omega = \frac{(\frac{\pi}{4})(0.0635)^2}{(0.5)^2} = 0.01268\ \text{sterad.}$$

For an isentropic expansion, the number density on the beam axis n(x) is approximated by

$$n = 0.161 \times n_o \times P_o \left(\frac{X}{D_o}\right)^{-2} \qquad (B.2)$$

At STP, the number density of one torr is

$$n_o = 3.24 \times 10^{16} \text{ atom/c.c.}$$

The number density at the skimmer entrance is

$$n = 0.161 \times 3.24 \times 10^{16} \times 760 \left(\frac{0.127}{5}\right)^2$$
$$= 18 \times 10^{14} \text{ atom/c.c.}$$

The mean velocity of argon at room temperature (298°K) is

$$v = 5 \times 10^4 \text{ cm/sec}$$

which gives a beam flux at the skimmer entrance to be

$$n \times v = 5 \times 10^4 \times 18 \times 10^{14} = 9 \times 10^{19} \text{ atom/cm}^2\cdot\text{sec}$$

The number of atoms entering the differential pumping chamber is

$$9 \times 10^{19} \times \frac{\pi}{4} (0.0635)^2 \text{ atoms/sec}$$

This corresponds to a pressure volume product of

$$= (3 \times 10^{17} \text{ atom/c.c. sec})/(3.24 \times 10^{19} \text{ atom/torr}\cdot\ell)$$
$$= 9.3 \times 10^{-3} \text{ torr}\cdot\text{lit/sec}$$

This gives a normal pressure, P_2, for the buffer chamber of

$$P_2 = \frac{9.3 \times 10^{-3}}{550\ \ell/\text{sec}} = 1.7 \times 10^{-5} \text{ torr}$$

The area of defining slit in the differential pumping wall is

$$= \text{width x height} = 0.1 \times 0.323$$
$$= 0.0323 \text{ cm}^2$$

Thus, the pressure in the main chamber is

$$P_3 = 5 \times 10^{-7} \text{ torr.}$$

The number density of the beam at the collision center is equal to 1.1×10^{13} atom/c.c. $\approx 3 \times 10^{-4}$ torr/c.c. at S.T.P.

Figure 2 shows the plot of the beam intensity of acetylene (C_2H_2) at the collision center versus the nozzle stagnation pressure as probed with an electron gun. The solid curve is the experimental curve and the dashed line is the predicted curve if we expect a linear increase in beam intensity as a function of stagnation pressure.

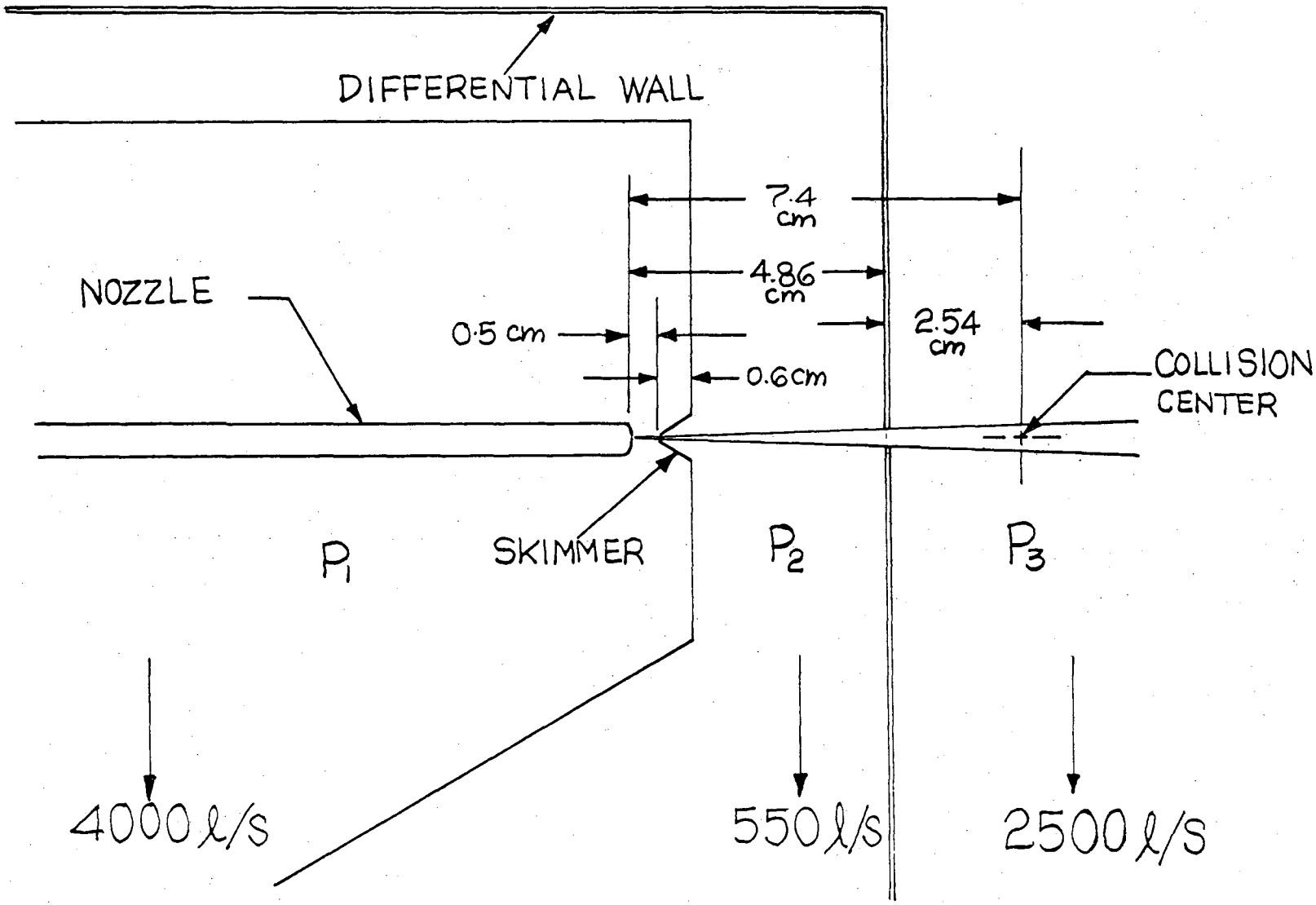

Fig. 1. Pumping arrangement for beam production system

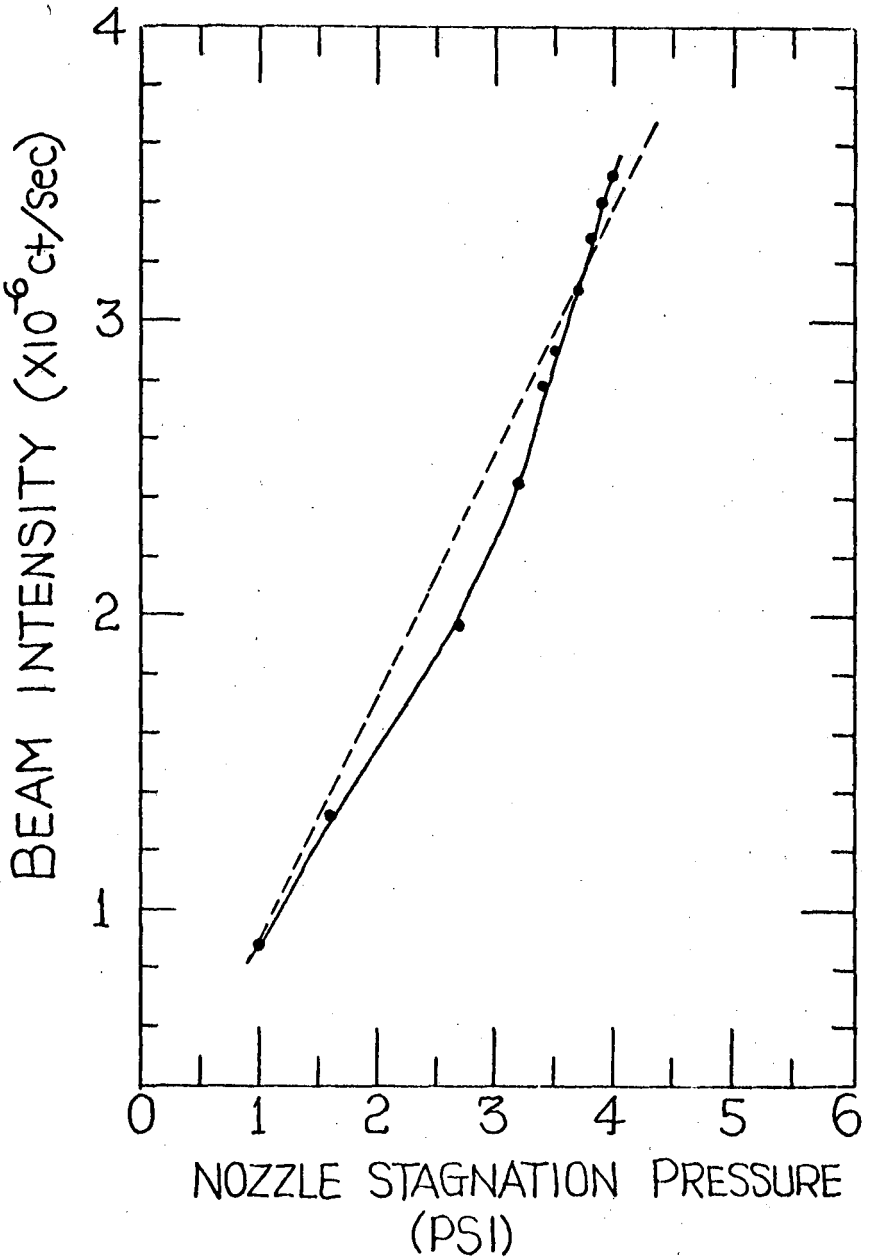

Fig. 2. Beam intensity of acetylene (C_2H_2) at the collision center as a function of nozzle stagnation pressure

C. Vacuum Ultraviolet Light Source

There are many light sources which have been designed and used for vacuum radiation studies. The choice of source depends on the application. A line spectrum is often more intense than a continuum source. For photoionization cross section measurements studied as a function of wavelength, it is preferable to use a continuum light source. Furthermore, for the photoionization studies in this research, the photon energies used lie between 6 eV and 21 eV. The various types of continuum light sources which produce photon energies within this range have been discussed by Samson[1] and described briefly in the following sections.

I. (a) The Hydrogen Continuum and Hydrogen Many-Line Pseudocontinuum.

The DC capillary discharge of H_2 at low pressure (1-5 torr) produces an emission continuum which extends from 1600Å to 5000Å. The sharp band structure of hydrogen starts at 1670Å and extends down to 850Å. This has the appearance of a line spectrum and gives rise to the commonly used term "the many line molecular hydrogen pseudocontinuum spectrum." The spectral range with which we are concerned for our application is shown in Fig. 1. The range is mainly covered by the hydrogen many-line pseudocontinuum. At low discharge pressures, the atomic resonance lines are more prominent than the band structure. On the other hand, an increase in discharge pressure and a corresponding increase in power dissipation in the light source, enhance the light intensity of the band structure and the atomic resonance lines are suppressed. In addition, the light intensity increases nearly linearly with power dissipation in the discharge lamp and the length of discharge capillary.

This is one of the most commonly used laboratory light sources in the wavelength region from 950Å to 2000Å. However, due to the sharp-line band structure, it is not suitable for high resolution studies.

(b) The He, Ne, Ar, Kr and Xe Hopfield Continua

Hopfield[2-4] first discovered the continuous emission spectrum of helium extending from 600Å to 1000Å. The continuum has been studied extensively by Tanaka and Huffman.[5-10] Huffman has observed that the continuum is emitted as an afterglow. In addition, it was found that helium continuum is best produced by a condensed spark discharge which produces more ionization. The following chain of reactions is suggested as a mechanism operative in a spark discharge in helium.

$$2He + He^+ \longrightarrow He_2^+ + He$$

$$He_2^+ + e \longrightarrow He_2^*$$

$$He_2^* \longrightarrow He_2 + h\nu$$

$$He_2 \longrightarrow He + He$$

Thus the intensity of the continuum would be expected to increase with pressure until the competing processes become important. Another fact which suggests that the He^+ ion is the primary reactant is the necessity for extremely pure helium in producing the continuum. In a gas discharge, the energy is absorbed primarily by the species with the lowest ionization potential, and since He has the greatest ionization potential of all the elements (24.58 eV), any impurity will tend to decrease the number of He^+ ions. Tanaka et. al.,[11] have attributed the origin of two main peaks near 810Å and 680Å to the transitions $A^1\Sigma_u^+ \rightarrow X^1\Sigma_g^+$ and $D^1\Sigma_u^+ \rightarrow X^1\Sigma_g^+$ respectively, as shown in Fig. 3. The helium continuum is shown in Fig. 4.

Similar emission continua for Ne, Kr and Xe have been found by Takamine[12] and Tanaka et. al.[13-15] The intensity distributions in the continuous emission spectra of Ar, Kr and Xe as excited by a 125W microwave generator are shown in Fig. 2. These three continua, nearly cover the same spectral region as the hydrogen many-line continuum. However, due to the high cost of Kr and Xe, the Kr and Xe continua are seldomly used in Laboratory.

By combining the use of helium Hopfield continuum and the hydrogen many-line pseudocontinuum, we essentially have a continuous light source covering the wavelength range from 600Å to 2000Å (~6 eV - 21 eV). This is sufficient for the photoionization experiments of this research.

II. Mechanical Construction and Operation of the Light Source

The discharge lamp consists of a quartz capillary discharge tube and two aluminum electrodes. The discharge capillary is a 6 mm O.D. and 11 inches long quartz capillary which is surrounded by a water jacket. The two ends of the tube are vacuum sealed to two water cooled aluminum electrodes by two cajoins. The assembly of the discharge lamp is shown in Fig. 7. The anode (which closes to the differential pumping arm of the monochromator) is normally grounded. During the operation of the lamp, gas (He or H_2) is being fed into the lamp from the front anode and continuously pumped out from the cathode by a small mechanical pump. This prevents the optical entrance slit which is usually very narrow from being clogged up by sputtering material produced during the discharge. The schematic diagram showing the discharge gas regulated system is shown in Fig. 5.

To excite the hydrogen many-line pseudocontinuum, about 3-5 torr of H_2 at a steady flow is maintained in the discharge lamp. The hydrogen gas used is the ultra-pure grade (99.999% purity) obtained from Matheson. A 1:1 ratio mixture of hydrogen and deuterium has also been used. Due to the difference in zero point energy of H_2, D_2 and HD, a better continuum is to be anticipated. The lamp is powered by a McPherson Model 740 d.c. power supply as shown in Fig. 6(a). The typical output spectrum obtained is shown in Fig. 1.

In order to excite the He Hopfield continuum, a high power pulser is used to pulse the discharge lamp. The helium used is also the ultra-high purity grade (99.999% minimum purity) obtained from Matheson. The electronic schematic block diagram is shown in Fig. 6(b). The Velonex 360 is used as a pulse oscillator. The frequency of this unit is continuously tunable from ~1 Hz to 0.3 MHz and the pulse width can be changed continuously from 0.05 μsec to 3 m sec with a maximum duty factor of 1.5%. The pulse generated by the Velonex 360 is further amplified by a pulse amplifier (LBL 17 × 4504 W-2) which is powered by a 15 kV, 500 mA d.c. power supply. The output is then fed to the cathode of the discharge lamp. As expected, it is found that the light intensity increases with the discharge He pressure. With a 100 μ optical entrance slit and the present differential pumping system, the maximum discharge He pressure allowed is ~100 torr. The maximum photon intensity was obtained when the repetitional rate of the pulse is 100 KHz, the pulse width is about 0.5 μsec and the d.c. power supply is set at 6 kV, 300 mA. The typical He Hopfield emission

spectrum observed is similar to that shown in Fig. 4. With the discharge conditions mentioned above, and the present monochromator system, about 10^{10} photon/sec Å at 800Å are obtained at the exit slit of the monochromator as estimated by a nickel photoelectric cell.

REFERENCES

1. J.A.R. Samson, "Techniques of Vacuum Ultraviolet Spectroscopy" John Wiley and Son, Inc., New York, 1967.
2. J. J. Hopfield, Phys. Rev., 35, 1133 (1930).
3. J. J. Hopfield, Phys. Rev., 36, 784 (1930).
4. J. J. Hopfield, Astrophys, J., 72, 133 (1930).
5. R. E. Huffman, Y. Tanaka, and J.C.L.C. Larrabee, Appl. Optics 2, 617 (1963).
6. R. E. Huffman, J. C. Larrabee, Y. Tanaka and D. Chambers, J. Opt. Soc. Am., 55, 101 (1965).
7. R. E. Huffman, L. C. Larrabee and D. Chambers, Appl. Optics, 4, 1145 (1965).
8. R. E. Huffman, W. W. Hunt, Y. Tanaka and R. L. Novack, J. Opt. Soc. Am., 51, 693 (1961).
9. R. E. Huffman, Y. Tanaka, and J. C. Larrabee, J. Opt. Soc. Am., 52, 851 (1962).
10. R. E. Huffman, J. C. Larrabee, and Y. Tanaka, Appl. Optics, 4, 1581 (1965).
11. Y. Tanaka, A. S. Jursa, and F. J. LeBlanc, J. Opt. Soc. Am., 48, 304 (1958).
12. T. Takamine, T. Suger, Y. Tanaka, and G. Imotani, Sci. Papers Inst. Phys. Chem. Research (Tokyo), 35, 447 (1939).
13. Y. Tanaka, and M. Zelikoff, Phys. Rev., 93, 933 (1954).
14. Y. Tanaka, and M. Zelikoff, J. Opt. Soc. Am., 44, 254 (1954).
15. Y. Tanaka, J. Opt. Soc. Am., 45, 710 (1955).
16. P. G. Wilkinson and E. T. Bryam, Appl. Optics, 4, 581 (1965).

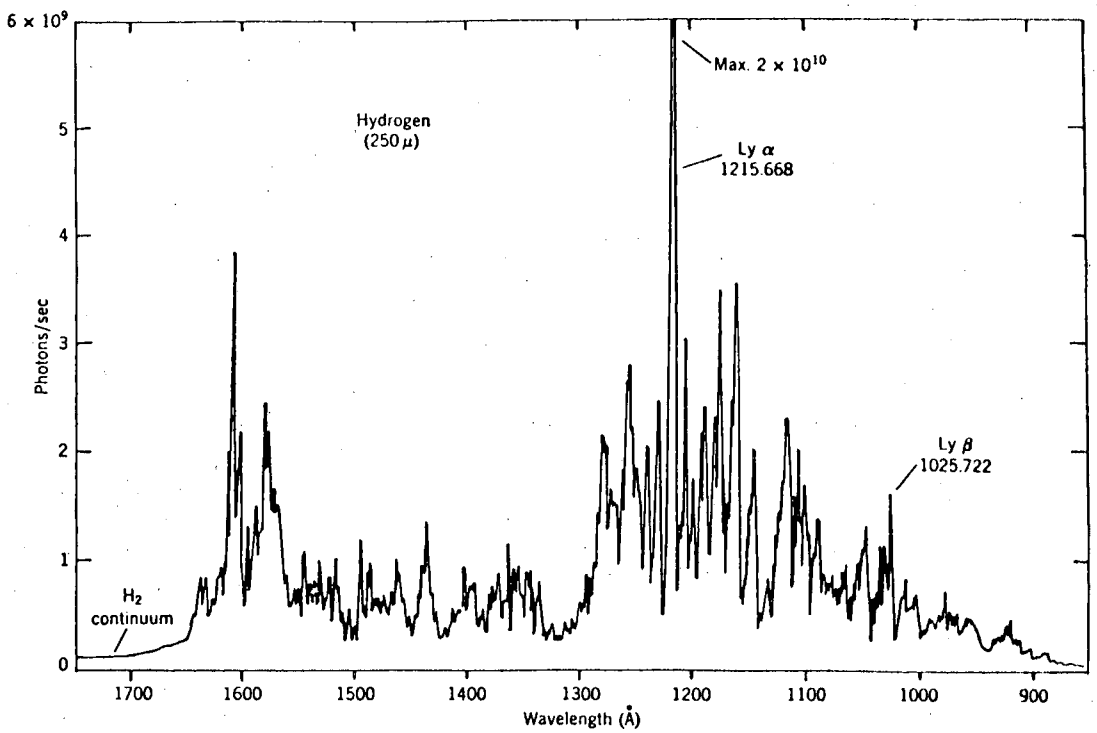

Fig. 1. H_2 spectrum between 850 and 1750 Å. Pressure, 250 μ; discharge current, 400 mA. No radiation is produced at wavelengths shorter than 800 Å.

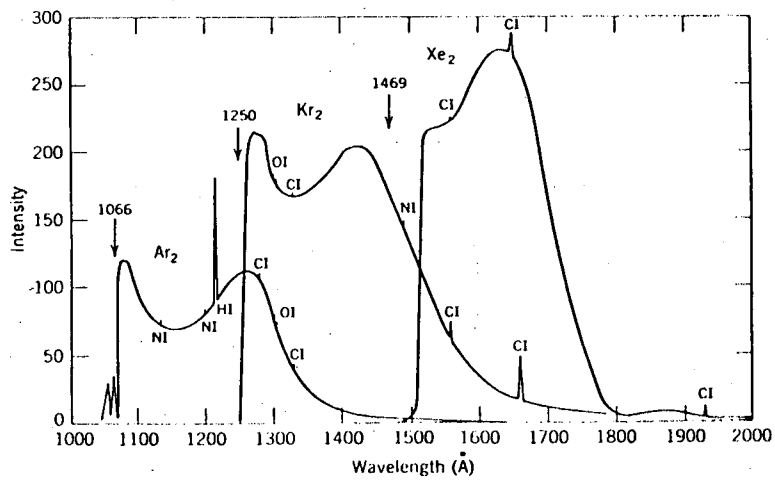

Fig. 2. Intensity distribution in the continuous emission spectrum of argon, krypton, and xenon as excited by a 125-W microwave generator. Gas pressure was 200 torr. Atomic emission lines of hydrogen, oxygen, nitrogen, and carbon are indicated. (16)

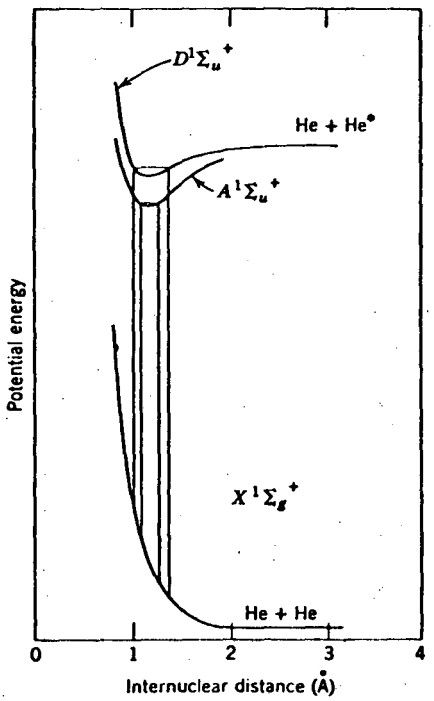

Fig. 3. Schematic diagram of the potential energy curves of He_2.

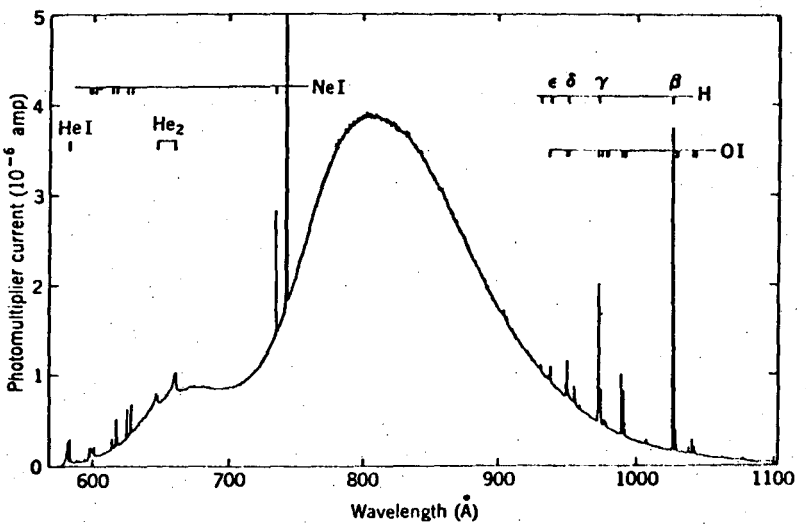

Fig. 4. Helium continuum using thyratron modulator. Conditions: sodium salicylate photomultiplier detector (EMI 9514S) at 1630 V; 0.5 Å bandwidth using 100-μ slits; power supply at 116 mA and 10 kV; 5-kc sec pulse repetition frequency; 44-mm Hg helium pressure; 1.0-sec time constant (7)

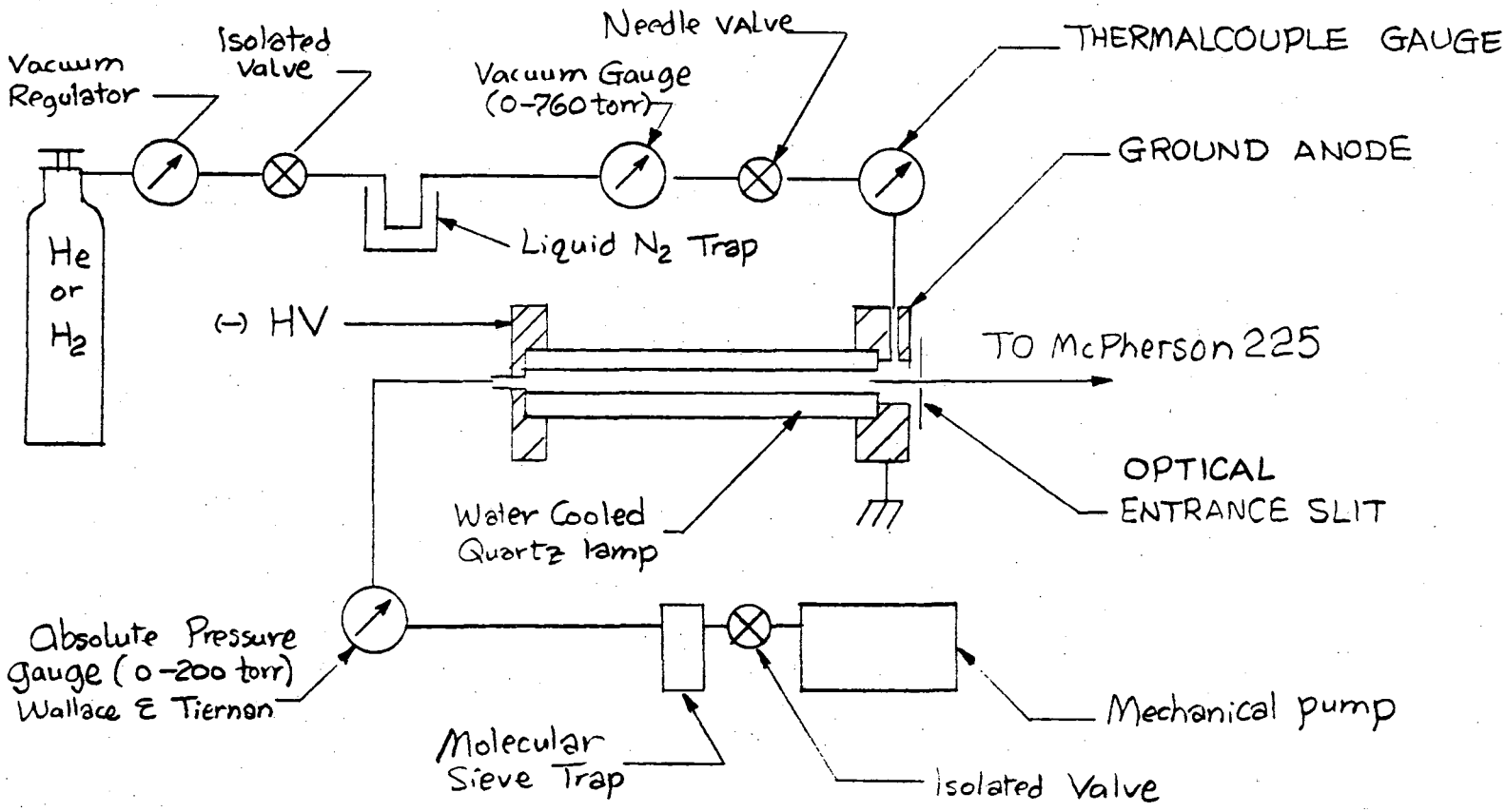

Fig. 5. Discharge Gases regulated System

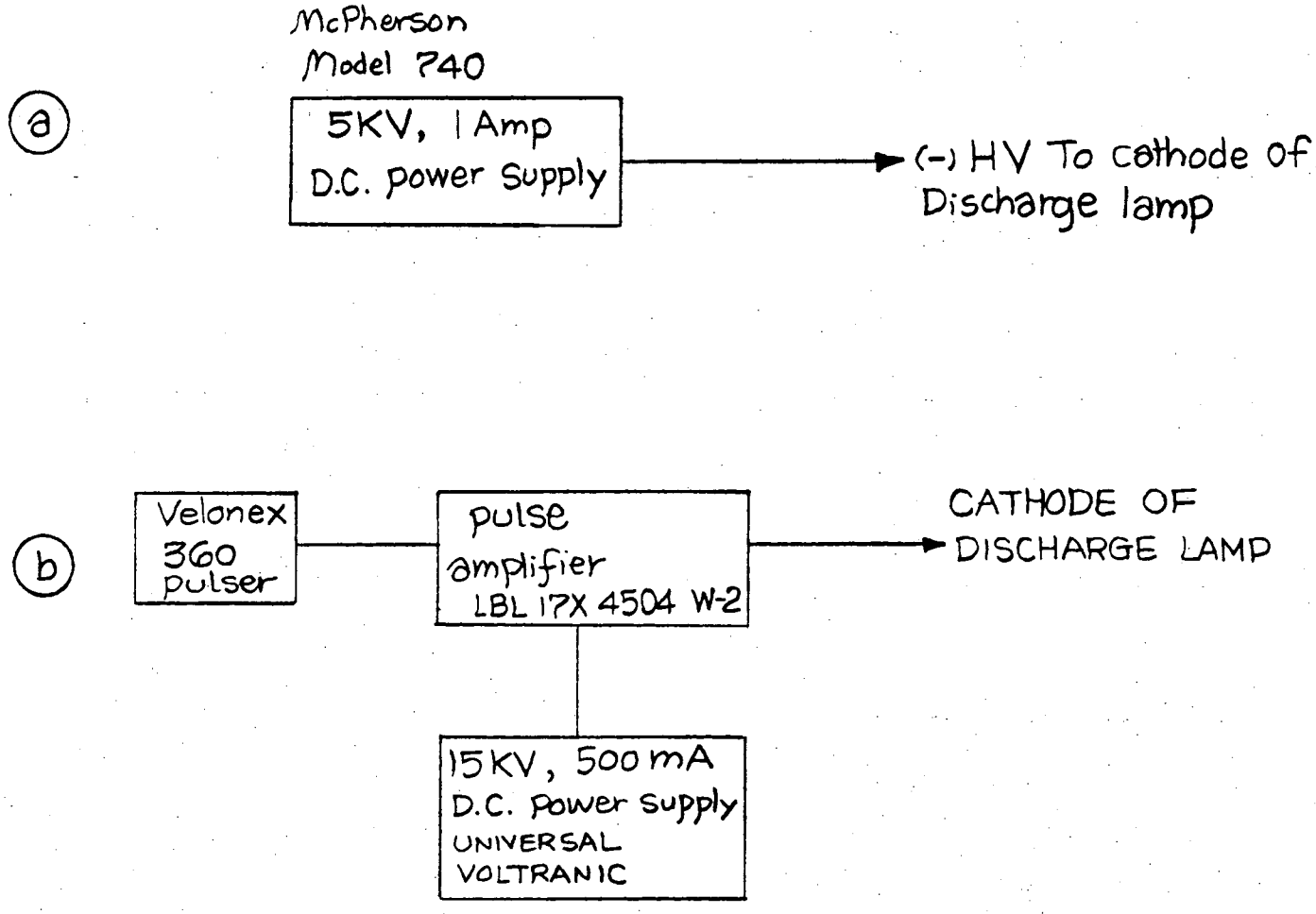

Fig. 6. Block assembly of discharge power supply.
(a) Power supply to produce H_2 pseudocontinuum.
(b) Power supply to produce He Hopfied continuum.

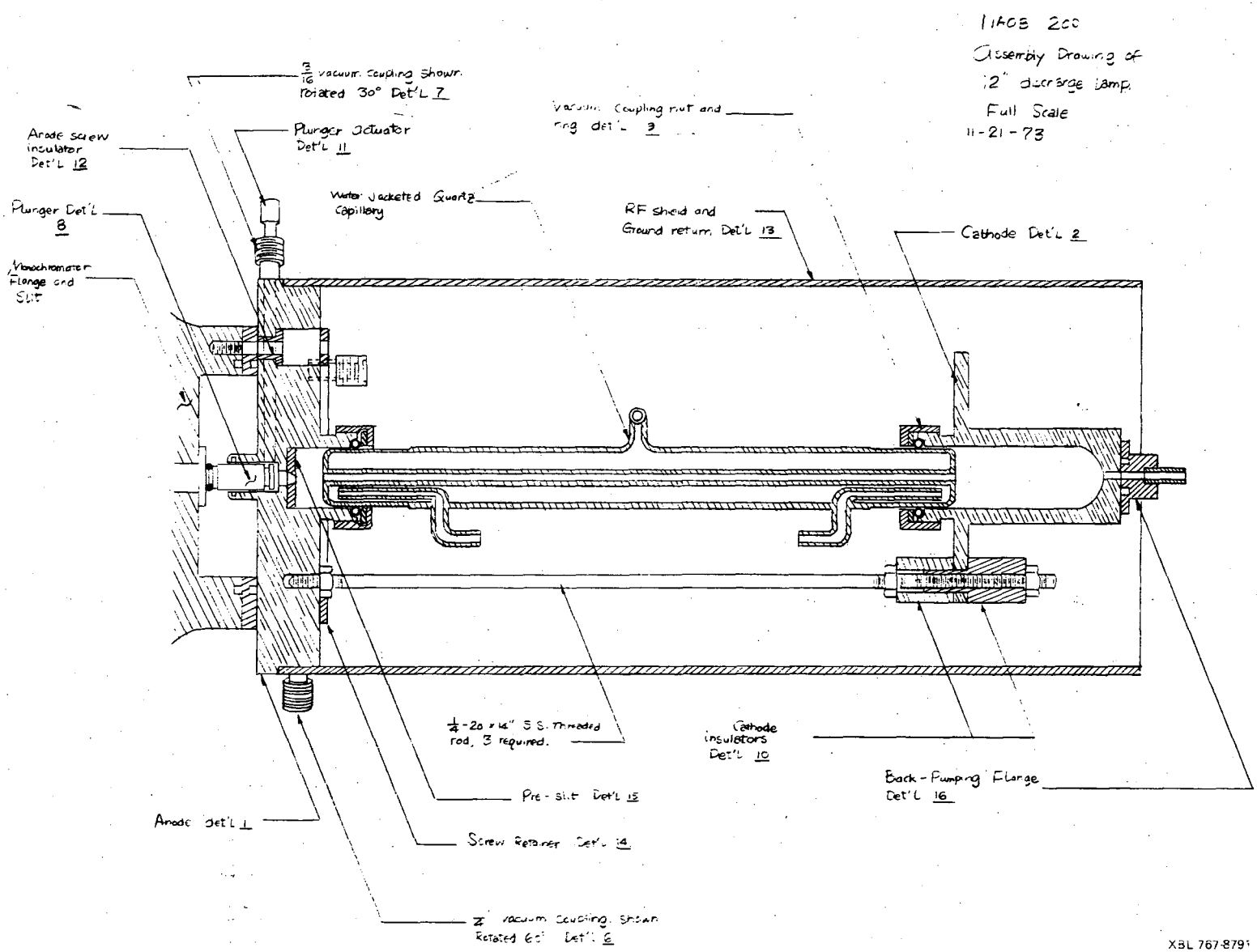

Fig. 7. Assembly of discharge light source.

D. Quadrupole Mass Spectrometer

The assembly of the quadrupole mass spectrometer system is shown in Fig. 1. The whole detector chamber is pumped by a 220 ℓ/sec (ULTEK) ion pump and a liquid nitrogen trap which is not shown in the drawing. A small manual operated gate valve is installed at the entrance of the quadrupole mass spectrometer system to isolate the detector chamber from the main chamber when the machine is not operating. During the operation of the apparatus, the detector is maintained at a pressure of $\sim 5 \times 19^{-9}$ torr. The ions generated at the collision center either by photon or electron impact are focused to the entrance of the quadrupole. After mass filtering, the ions are focused again, accelerated and then bombard an aluminum coated target which ejects two to seven electrons per ion, depending on the mass of the bombarding ions. These electrons are further accelerated on an aluminum coated thin plastic scintillator[1] (0.0005" thick) which is cemented on a quartz window with optical epoxy (which has approximately the same refractive index as the plastic scintillator (NE111). The light generated due to the impact of the electrons then further amplified by a photomultiplier (RCA 8850) which gives out a pulse which is then counted by a scaler. The electronic for the counting system is described in Section F. The assembly and electronic wiring for the ionizer and focusing ion optics is shown in Fig. 2. In order to eliminate the ion pump noise, a ground metal shield is placed around the scintillation detecting system. In addition, an optical baffle is installed at the pump port of the ion pump to prevent the soft x-rays from interfering with

the scintillation detector. (Not shown in Fig. 1)

The general scintillation system can be understood by dividing the process into six consecutive events.

1. The absorption of 30 keV electrons in the plastic scintillation system, resulting in excitation and ionization within it.
2. The conversion of energy dissipated in the scintillator to light energy through the luminescence process.
3. The transit of light photons to the photocathode of the photomultiplier tube.
4. The absorption of the photons at the cathode and the emission of the photoelectron.
5. The electron-multiplication process within the photomultiplier tube.
6. The analysis of the current pulse furnished by the photomultiplier tube through the use of the succeeding electronic equipment.

If n_e is the number of photoelectrons released from the photocathode and M is the multiplication factor of the tube, then the charge q appearing at the output of the photomultiplier is

$$q = Men_e \tag{D.1}$$

$$n_e = (nE_nF_nC_{np})(T_pF_p)(S_m F_c) \tag{D.2}$$

E_n is the energy of the high energy electrons

F_n is the fraction of total energy of bombarding electrons absorbed by the scintillator.

C_{np} is the efficiency of conversion from electron energy dissipated in

the scintillator to light energy.

T_p is the transparency of scintillator for scintillation which it produces.

P_p is the fraction of light photons which reach photocathode if T_p=1.

S_m is the sensitivity of photocathode at wavelength for maximum sensitivity in terms of photoelectrons per electron volt of light energy striking it.

f is the figure of merit expressing the degree to which the spectral sensitivity of photocathode matches spectral distribution of scintillation.

F_c is the fraction of photoelectrons collected by dynodes.

Let n to be the number of high energy electrons, then $nE_nF_nC_{np}$ = the amount of light energy in the scintillation.

T_pF_p = fraction of light which reaches the photocathodes.

$S_{mf}F_c$ = number of photoelectrons reaching the first dynode of the multiplier per electron volt of light energy striking the photocathode.

The output pulses of the phototube are inductively coupled to the counting electronic system (Fig. 5). The photomultiplier used in this apparatus has a quantum yield of ~40% which corresponds a value of S_m = 0.1, let us assume

$T_pF_p = 0.5$

$F_nC_{np} = 0.03$

$S_{mf}F_c = 0.05$

$n = 6$

$M = 5 \times 10^6$

The output pulse width is $\sim 2 \times 10^{-9}$ sec.

With a 50Ω connector, the pulse height is

$$V = IR = \left(\frac{q \text{ coul}}{2 \times 10^{-9} \text{ sec}}\right)(50\Omega)$$

$$n_e = (6 \times 30 \times 10^3 \times 0.03)(0.5)(0.05) = 140$$

$$q = 140 \times 1.9 \times 10^{-19} \times 5 \times 10^6 = 1.33 \times 10^{-10} \text{ coul}$$

$$V = \frac{1.33 \times 10^{-10} \times 50}{2 \times 10^{-9}} \approx 3 \text{ volt}$$

In order to examine the detector, pulse height analysis has been carried out with the set up as shown in Fig. 3. The pulse height distribution with different cathode voltages and electron energies is shown in Fig. 4. To discriminate the single electron noise from the photocathode, the discriminating level only set at approximately 0.2 volt.

REFERENCES

1. N. R. Daly, The Rev. of Scientific Inst., 31, 264 (1960).

2. W. J. Price, "Nuclear Radiation Detection" McGraw Hill Book Company, 2nd Ed. (1964).

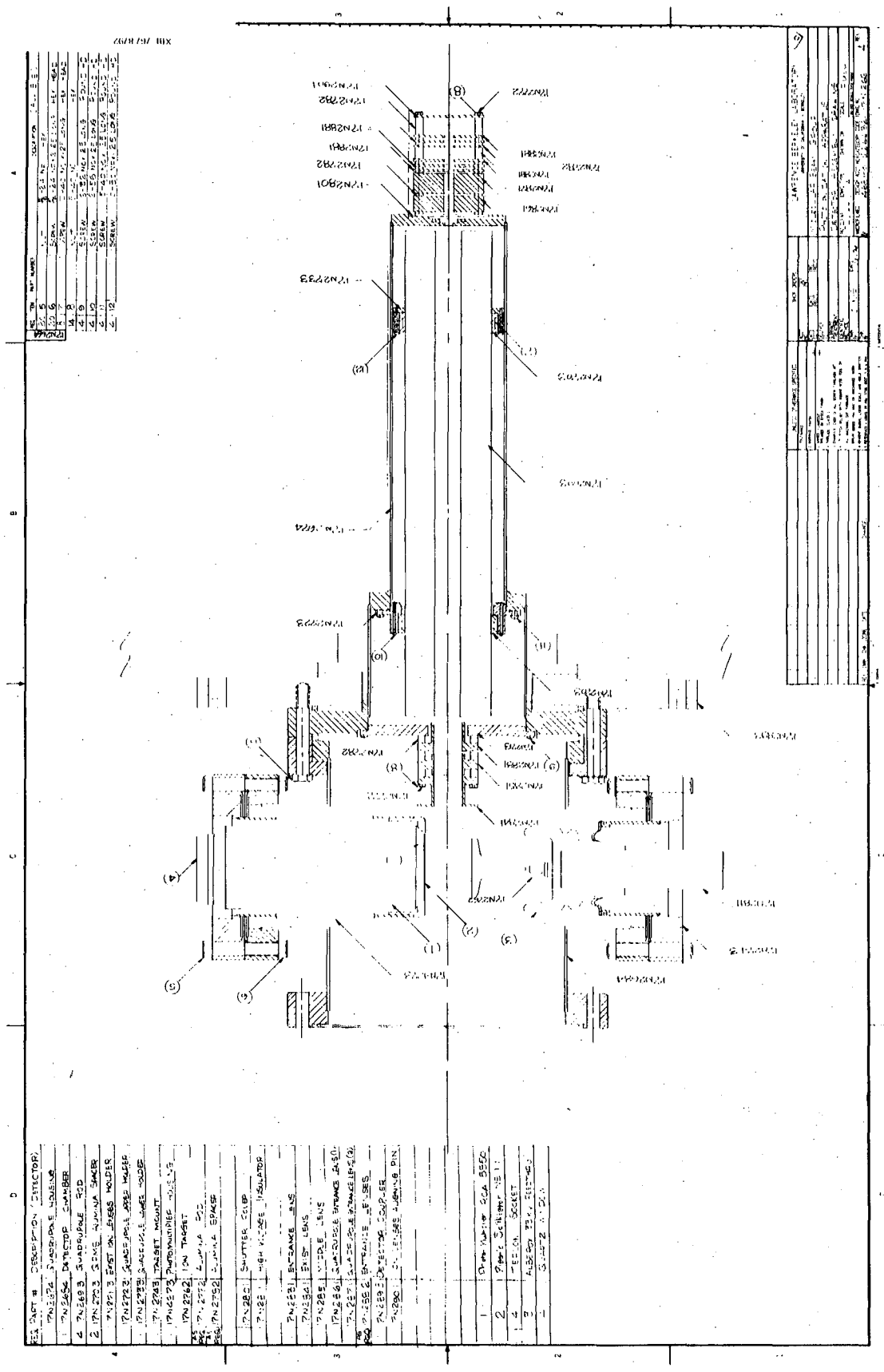

Fig. 1. Assembly of quadrupole mass spectrometer.

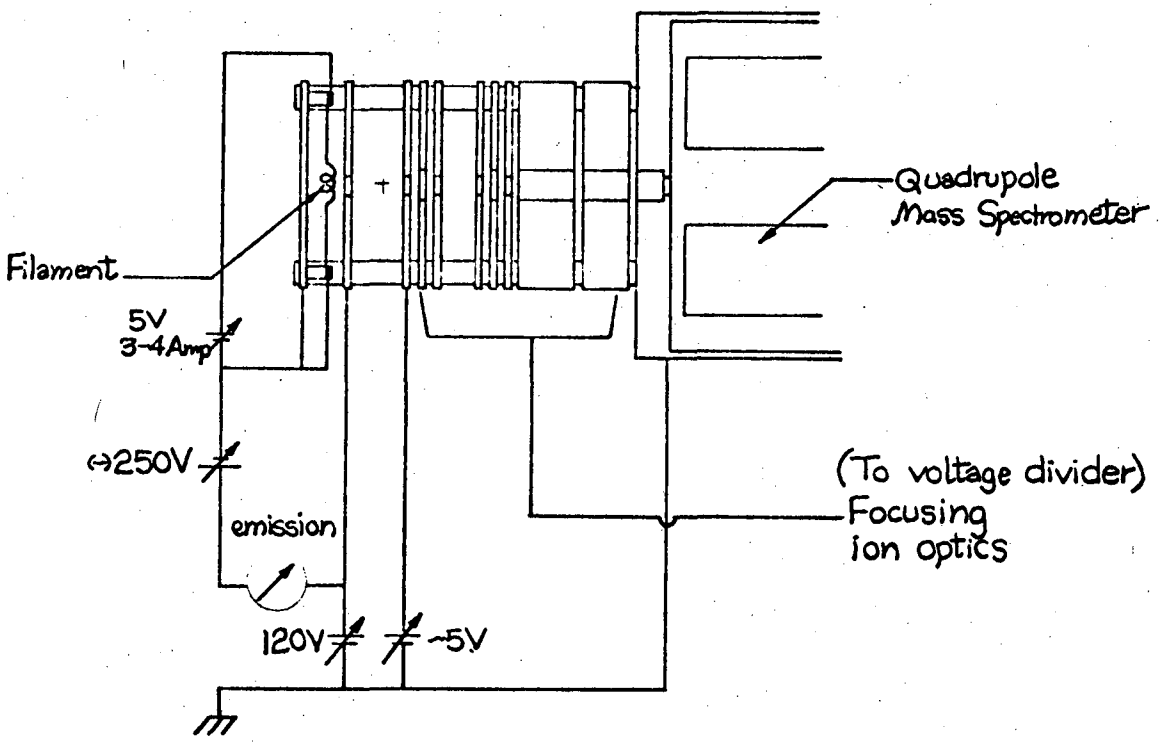

Fig. 2. Assembly of the ionizer and focusing elements

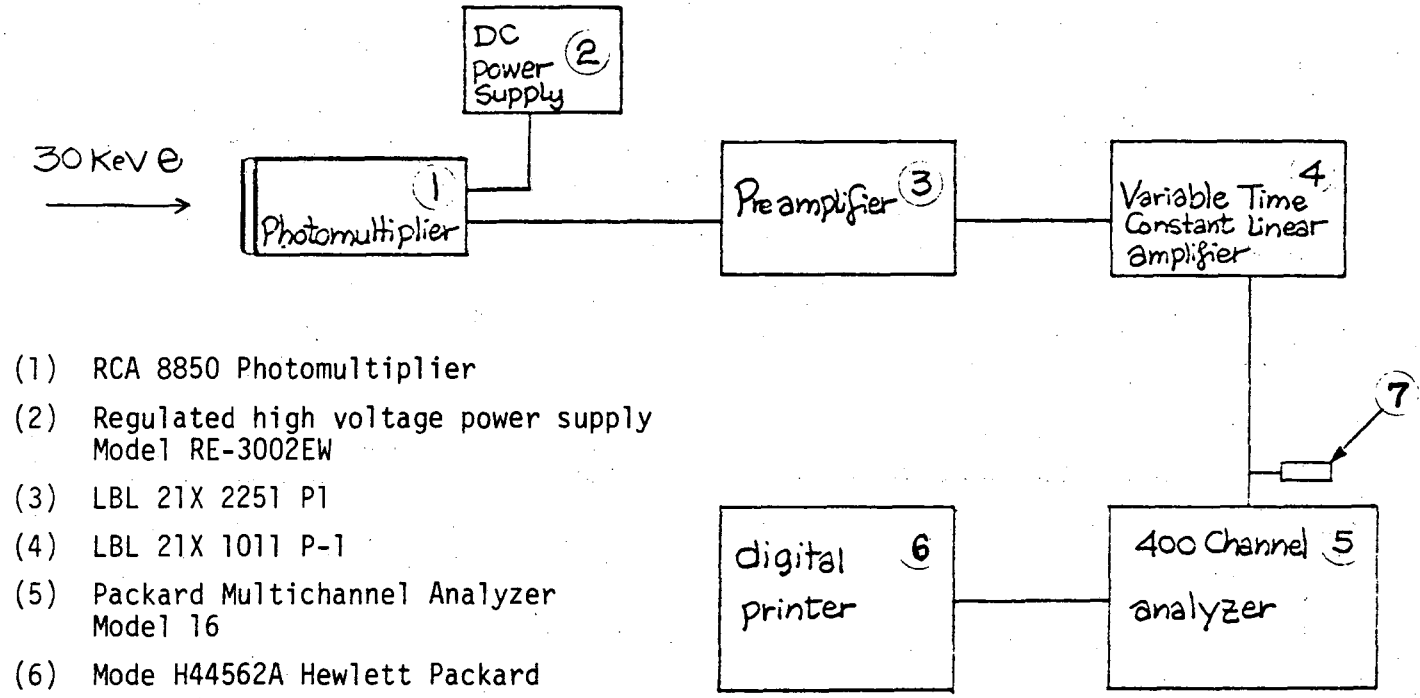

(1) RCA 8850 Photomultiplier

(2) Regulated high voltage power supply
Model RE-3002EW

(3) LBL 21X 2251 P1

(4) LBL 21X 1011 P-1

(5) Packard Multichannel Analyzer
Model 16

(6) Mode H44562A Hewlett Packard

(7) 125Ω Terminator

Fig. 3. Pulse Height Anaysis Mode

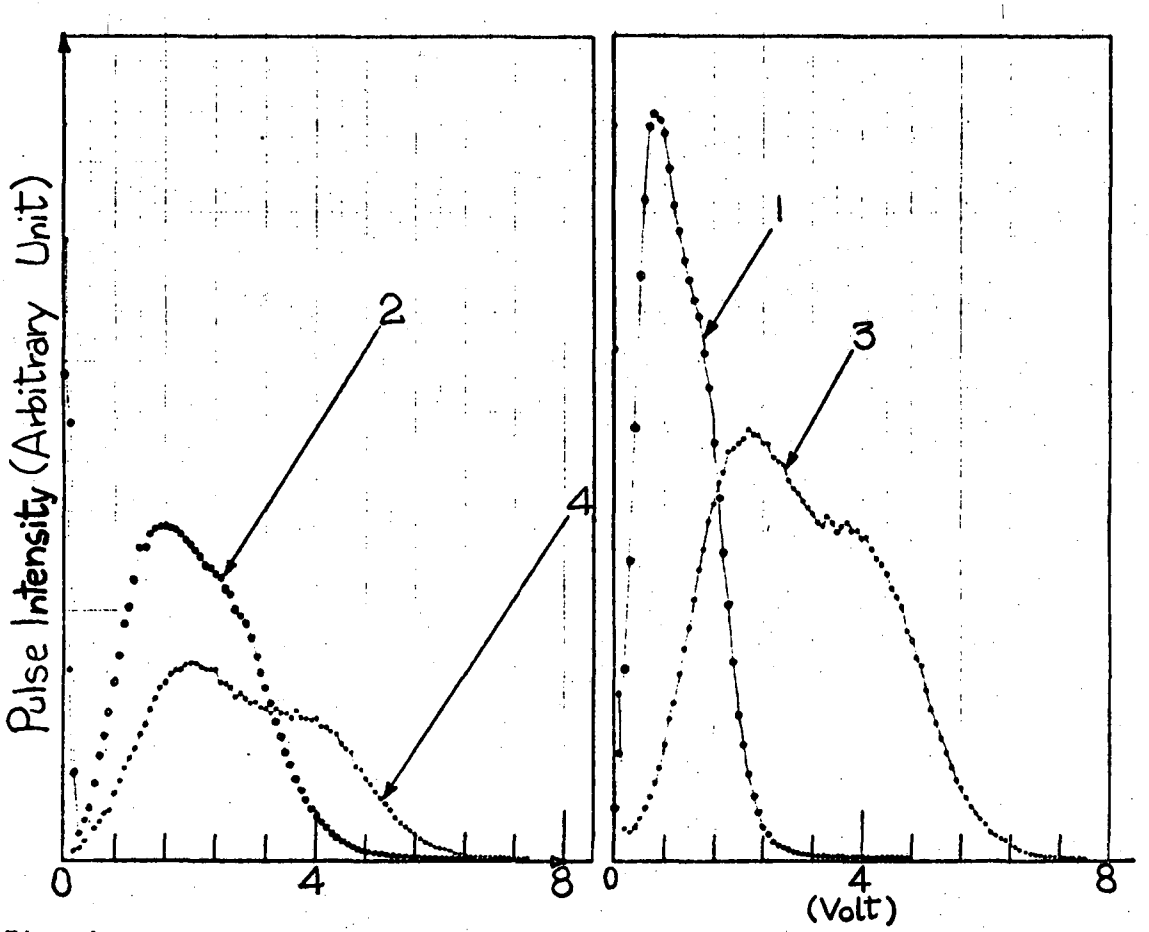

Fig. 4.
Amplifier at a gain = 4

Curve 1: Phototube cathode voltage = (-)2150 V, electron energy = 30 keV
Curve 2: Phototube cathode voltage = (-)2250 V, electron energy = 25 keV
Curve 3: Phototube cathode voltage = (-)2250 V, electron energy = 30 keV

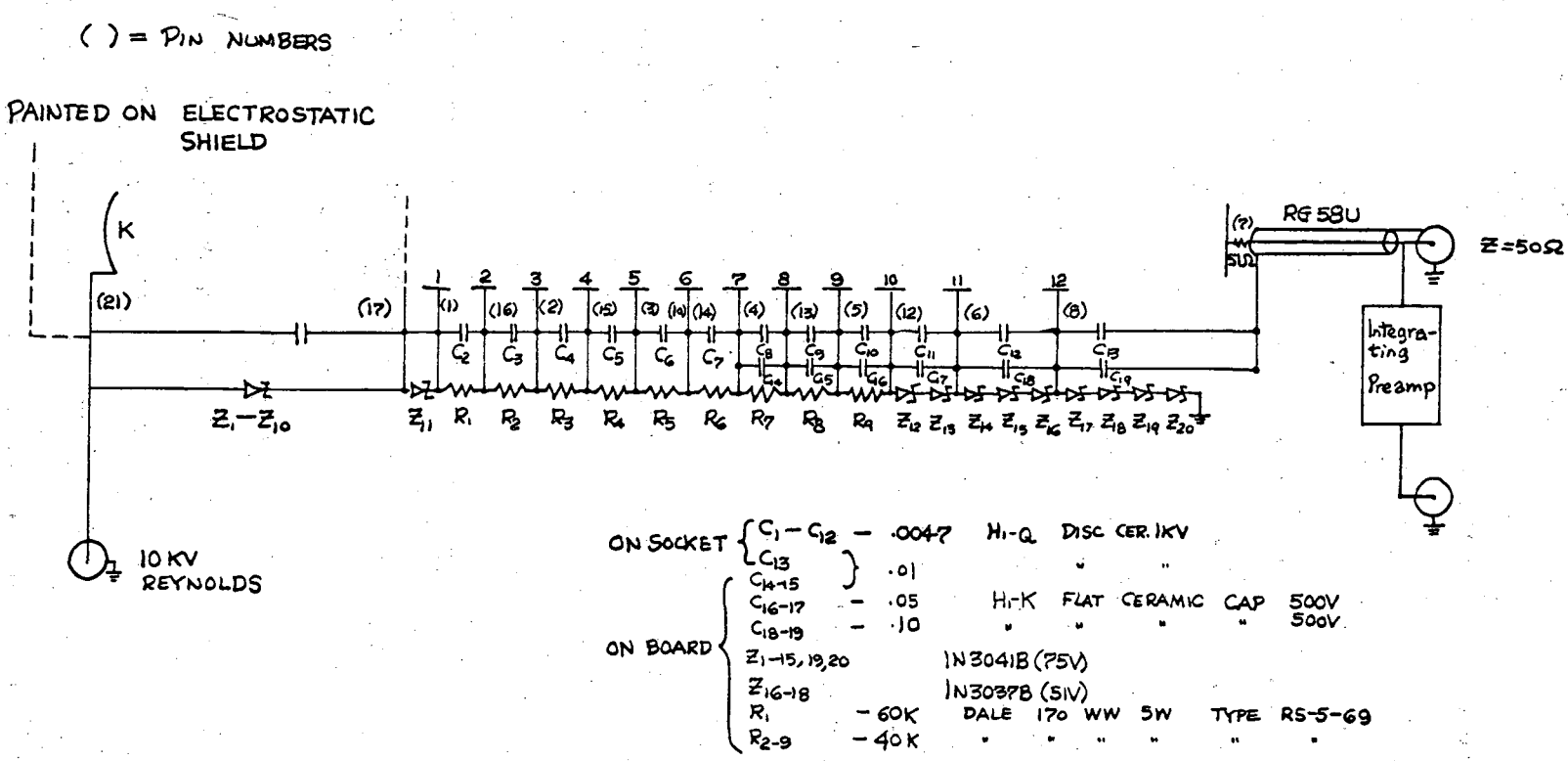

Fig. 5. RCA 8850 BASE WIRING (LBL 21X227 S-1)

E. The Vacuum Ultraviolet Photon Detectors

The various modes of interaction between radiation and matter provide the underlying principles of all detectors. For vacuum UV radiation, these interactions involve the photoionization of gases, the ejection of photoelectrons form metals, chemical changes, photoconductivity, fluorescence, and thermal effects. Two types of VUV photon detectors are used in this research.

I. (a) Fluorescent Detector.

This technique essentially combines the use of a photomultiplier with a scintillator. The scintillating material used is sodium salicylate which has been found to be one of the materials that have the highest fluorescent efficiency in the range 400 - 2000Å.[1] The assembly diagram of the fluorescent detector is shown in Fig. 1. A fine crystalline layer of sodium salicylate is coated on a quartz window. The latter is cemented to an aluminum flange. The impingement of VUV photons produces a fluorescent emission spectrum as shown in Fig. 2. (The maximum intensity of fluorescence is located at 4200Å and coincides with the maximum sensitivity of a photomultiplier.) The fluorescent signal is thus amplified by the phototube and measured by a picoammeter. The properties of sodium salicylate have been well studied. Figure 3 shows the relation between response and thickness of the sodium salicylate layer at 1200Å.[2] It can be seen that the efficiency rises rapidly to a maximum at 1 mg/cm^2 then falls off very slowly as the thickness increases. The relative quantum efficiency of sodium salicylate between 200 and 1000Å is depicted in Fig. 4;[3] and Fig. 5[4] shows the aging efficiency of coating.

It was found that the fluorescent spectrum of sodium salicylate was independent of the exciting wavelength between 275 and 2537Å.[5] The fluorescent decay time of sodium salicylate appears to lie between 7 and 12 nsec.[6,7]

I. (b) Nickel Photoelectric Detector.

The photoelectric yields of most metals have been measured from 2 - 1500Å.[8,9] It was found that for the spectral region from 473Å to 1000Å, the photoelectric yield of a heat treated nickel cathode is nearly constant. Using a nickel sheet as the cathode in a simple diode arrangement, the total photoelectric emission current $I(\lambda)$ measured is related to the incident photon flux by the following relation:

$$Ni(\lambda) = (I(\lambda) \times 6.24 \times 10^{18})/\gamma(\lambda) \text{ photon/sec}$$

where $\gamma(\lambda)$ is photoelectric yield of nickel.

The mechanical drawing for the construction of the nickel photoelectric detector is shown in Fig. 6.

REFERENCES

1. F. S. Johnson, K. Watanabe and R. Tousey, J. Opt. Soc. Am., 41, 702 (1951).
2. M. Seya and F. Masuda, Sci. Light, 12, 9 (1963).
3. J.A.R. Samson, unpublished data (1965).
4. J.A.R. Samson, J. Opt. Soc. Am., 54, 6 (1964).
5. K. J. Nygaard, Brit. J. Appl. Phys., 15, 597 (1964).
6. K. J. Nygaard, private communication (March 1965).
7. G. K. Herb and W. J. Van Sciver, Rev. Sci. Inst., 36, 1650 (1965).
8. W. C. Walker, N. Wainfoin and G. L. Weissler, J. Appl. Phys., 26, 1366 (1955).
9. H. Hinteregger and K. Watanabe, J. Opt. Soc. Am., 43, 604 (1952).

① Sodium Salicylate
② Quartz Window
③ Lucite Light Pipe
④ EMI 9634 QR Photomultiplier
⑤ Mounting Fixture
⑦
⑥ Aluminum Light Shield
(Black anodized inside)

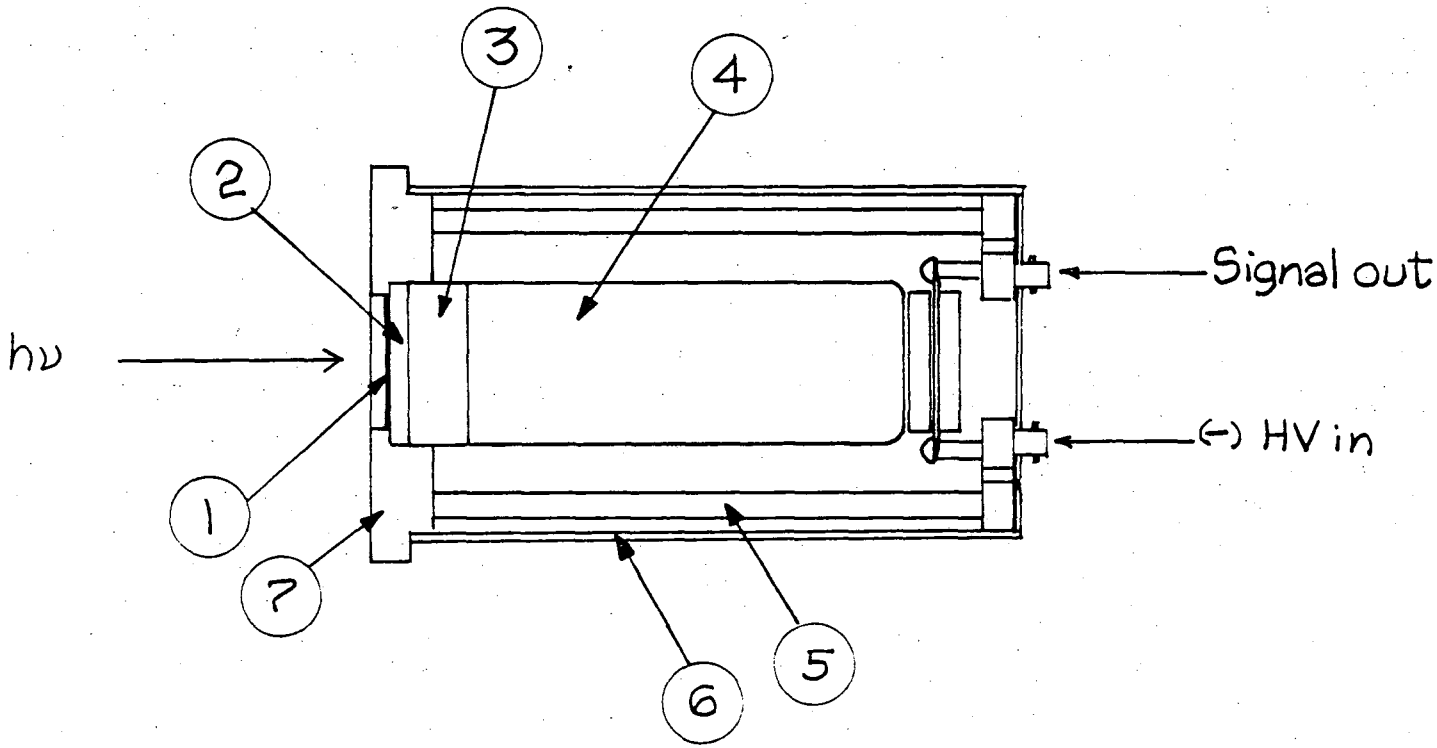

Fig. 1. Assembly of the fluorescent detector

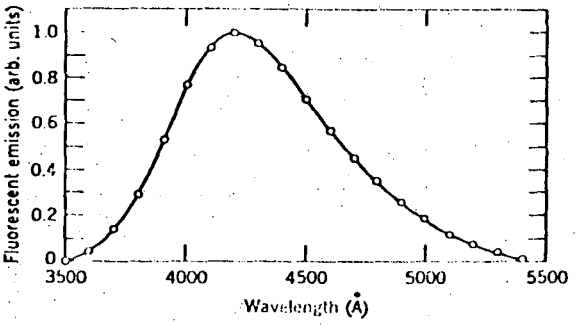

Fig. 2. Fluorescent emission spectrum of sodium salicylate

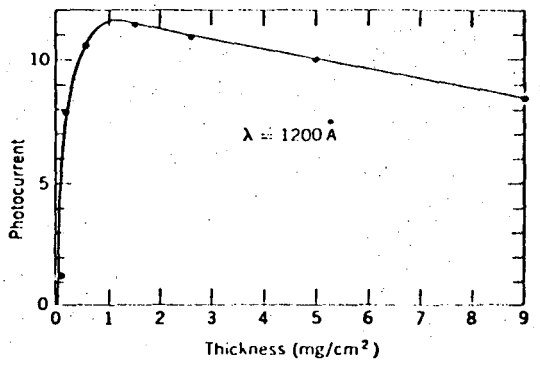

Fig. 3. Relation between response and thickness of sodium salicylate layer at 1200 Å

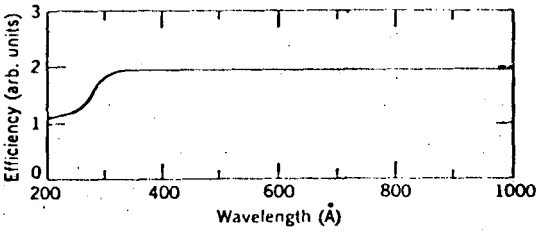

Fig. 4. Relative quantum efficiency of sodium salicylate between 200 and 1000 Å.

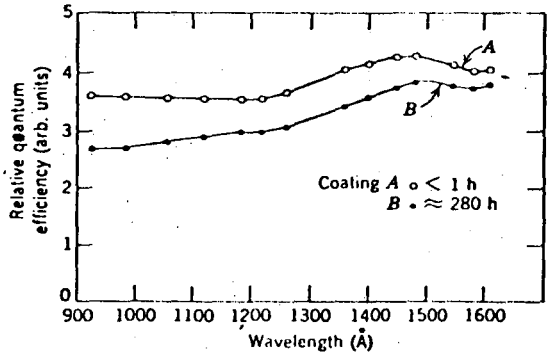

Fig. 5. Relative quantum efficiency of sodium salicylate between 900 and 1600 Å. The yield was measured for two different coatings relative to a thermopile. Coating *A* is less than one hour old while coating *B* is approximately 280 hours old

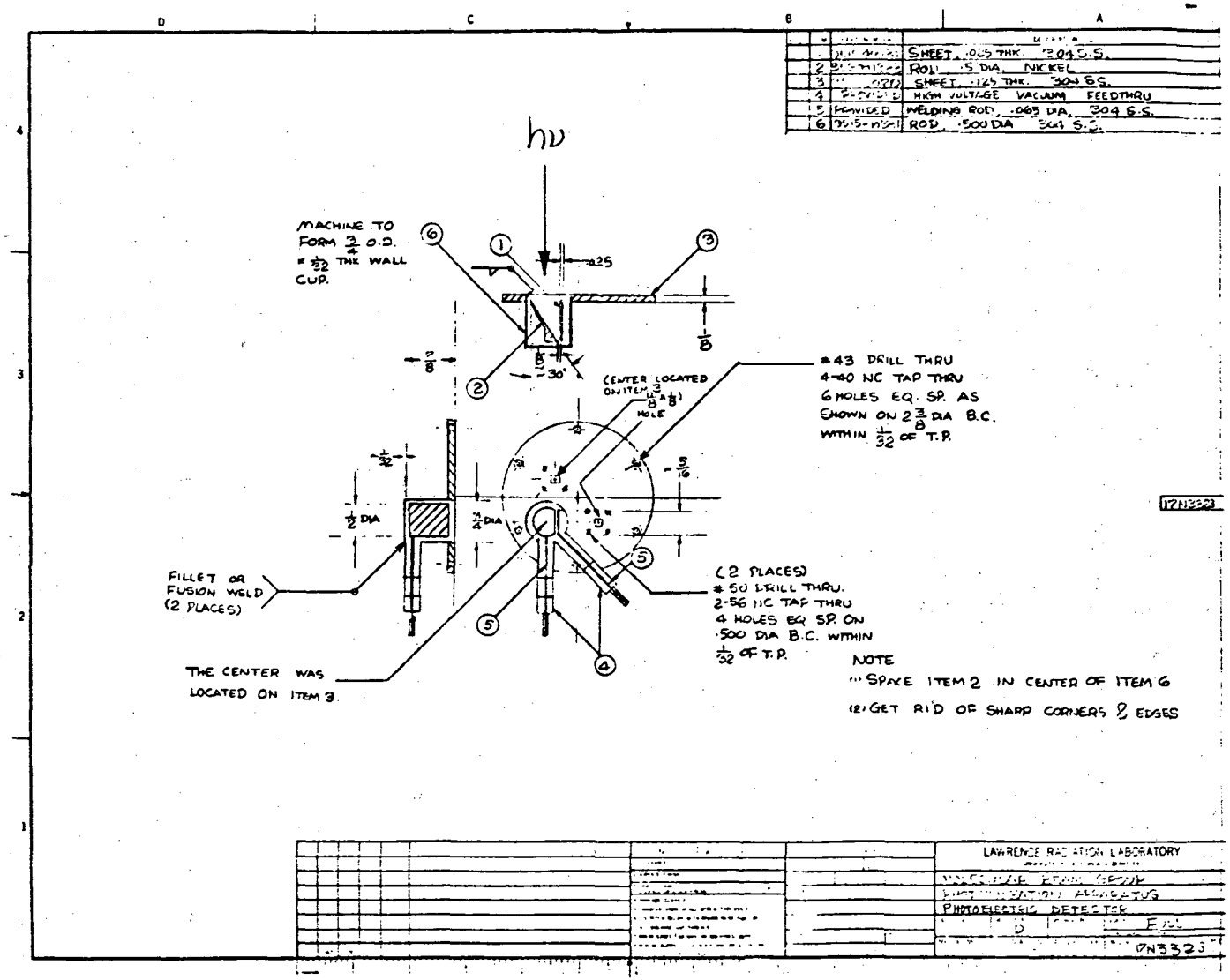

Fig. 6. Photoelectric detector

F. Automatic Scan Control System for Photoionization Apparatus

The electronic block diagram for the photoionization apparatus is shown in Fig. 1. During the photoionization experiment the ion intensity and the photon intensity at a corresponding wavelength have to be monitored simultaneously. The ion and photon detection in the manual mode have been described in the experimental part of Chapter 3. This section describes the operation of the photoionization apparatus in an automatic mode. The scan control timing diagram for the photoionization apparatus is shown in Fig. 2. The system is initiated by pressing the start control on the timer. A pulse (time out or gate 3) with the width corresponding to the present time on the timer will enable the third scaler to count the pulses generated by the voltage to frequency converter (this measures the photon intensity in number of counts). The rising edge of this pulse also initiates gates 1 and 2 which gate scaler 1 and 2 respectively. These two gates are generated by the 150 Hz chopper as mentioned in the experimental part of Chapter 3. The signal of scaler 1 corresponds to the photoion intensity when the chopper is opened and scaler 2 gives the background ion signal when the chopper is closed. The falling edge of the time out pulse (which synchronizes with the falling edge of the last pulse of gate 2) then energizes the oscillator of the printer to print out the signals of the three scalers. Simultaneously, after the printing, the falling edge of the last printing pulse triggers two pulses to reset the timer and scalers as well as the automatic clock pulses (3μs width) to step the stepping motor upward or downward to a preset number of steps

(80 step for 1Å increment). The rising edge of the run count pulse advances the counter in the control unit from display 1 to 2 (i.e. the first run is complete) and generates a restart pulse to start the timer for the second run. The system will continue until it has completed the number of runs as preset in the control unit.

The photon signal as measured by the picoammeter is also recorded by a strip chart recorder. This gives a secondary record of the photon intensity. The analog output (0 - 1.5 V) is converted to digital output by a voltage to frequency converter as mentioned above. In order to preserve the relative intensity of the photon, the voltage to frequency converter has to have a linear response to the voltage output from the picoammeter. Thus the linearity of the V/f is examined and plotted in Fig. 3 which shows a relation

$$f(\text{KHz}) = 59004\ V + 57$$

where V is the input voltage in volt and f is the output frequency in KHz.

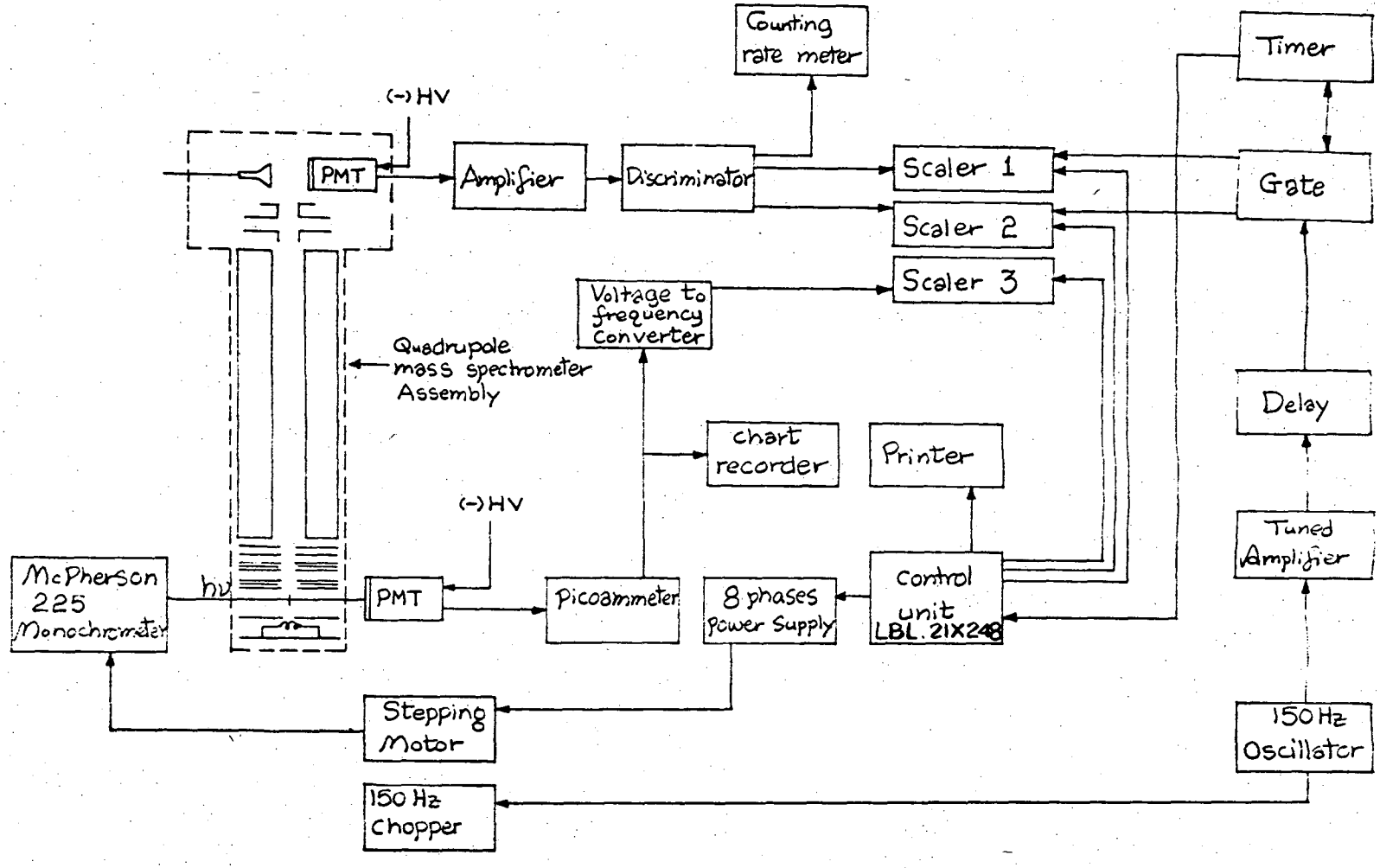

Fig. 1. Electronic block diagram of the photoionization apparatus

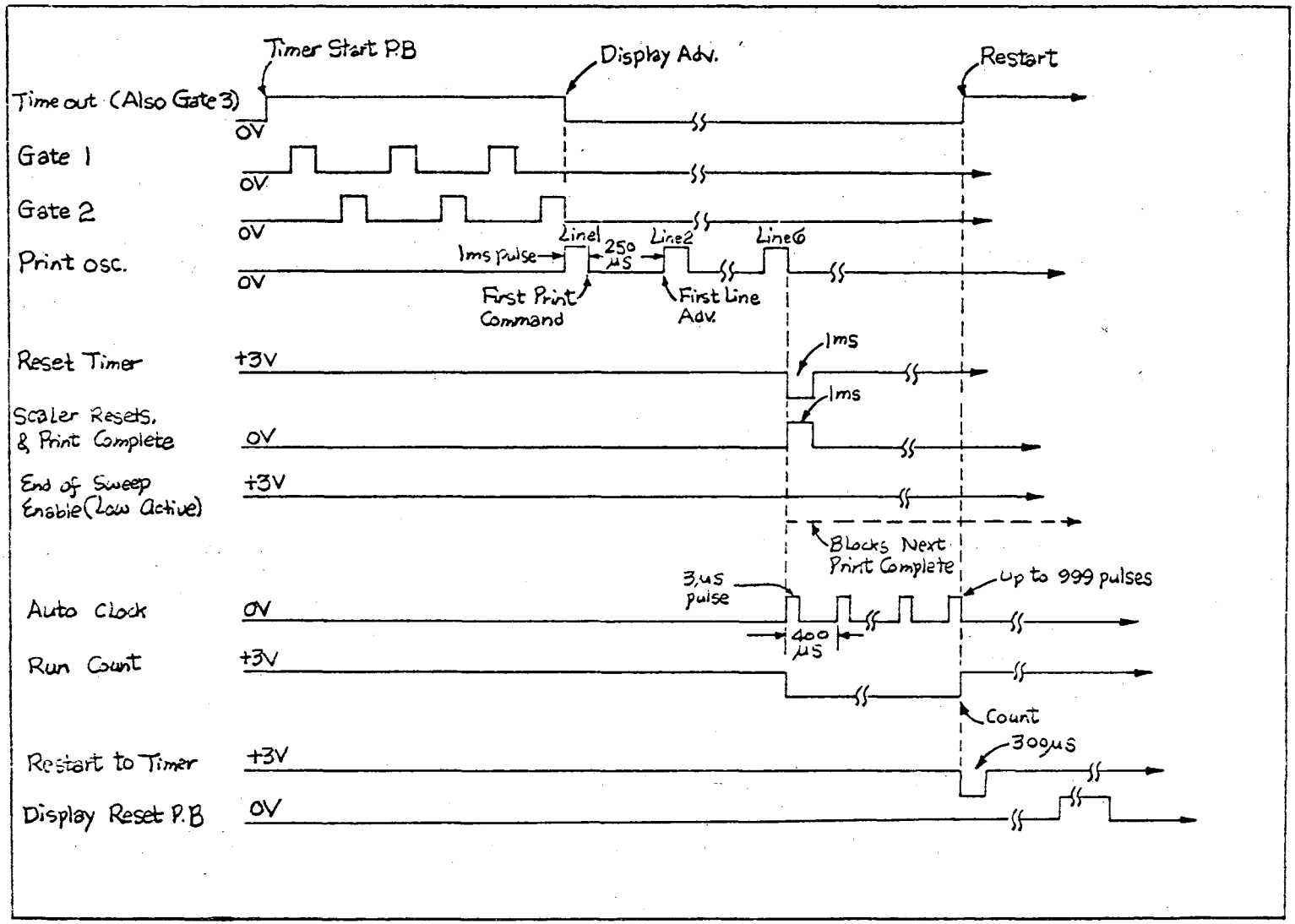

Fig. 2. SCAN CONTROL TIMING DIAGRAM

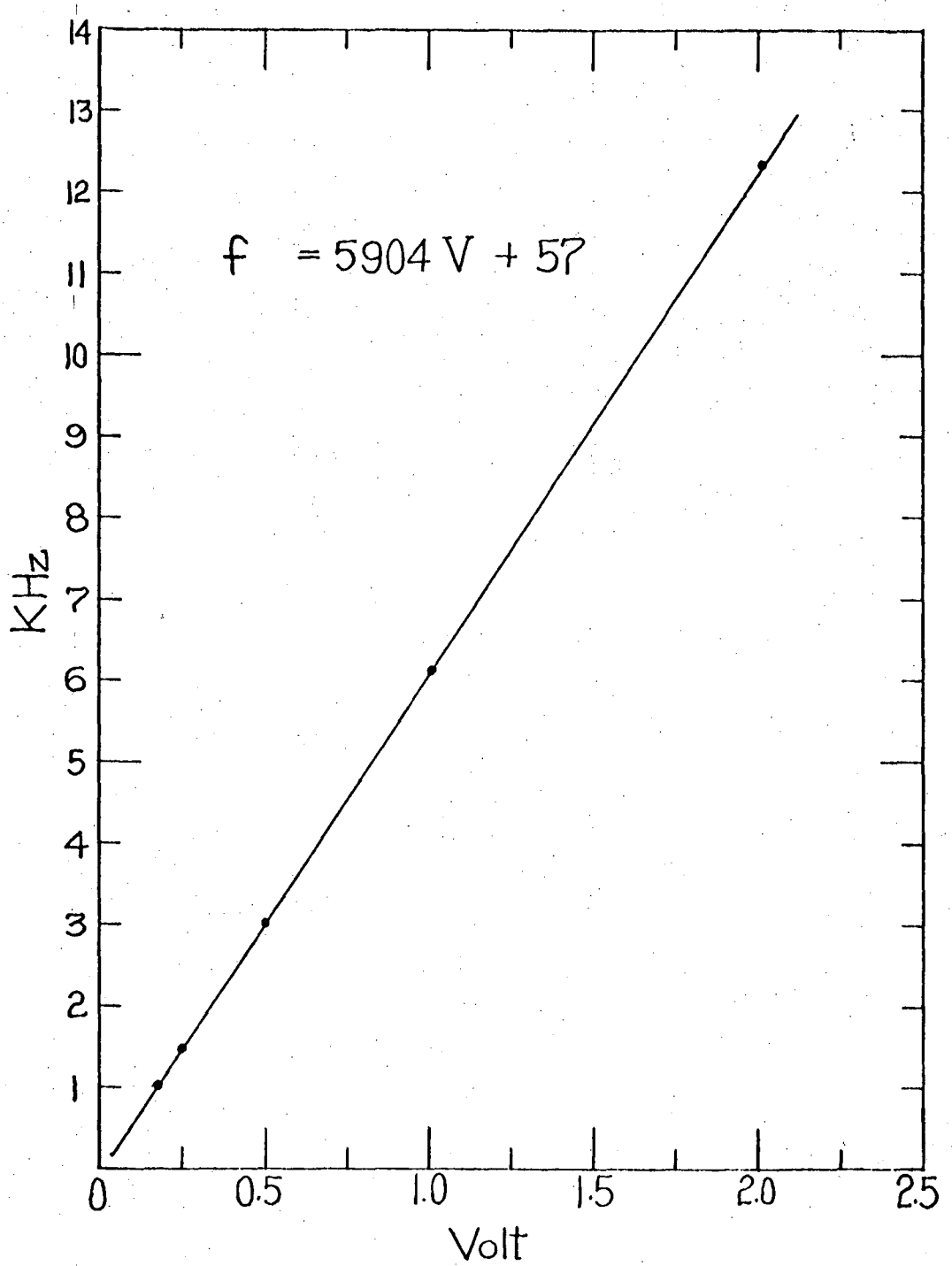

Fig. 6. Linearity plot of the voltage to frequency converter

This report was done with support from the United States Energy Research and Development Administration. Any conclusions or opinions expressed in this report represent solely those of the author(s) and not necessarily those of The Regents of the University of California, the Lawrence Berkeley Laboratory or the United States Energy Research and Development Administration.

TECHNICAL INFORMATION DIVISION
LAWRENCE BERKELEY LABORATORY
UNIVERSITY OF CALIFORNIA
BERKELEY, CALIFORNIA 94720